

Shape and Size Specific:  
Fabrication, Characterization, and Application of Highly Tailored Biocompatible Hydrogel  
Particles for Use in Materials and Biomedical Settings

Kevin Patrick Herlihy

A dissertation submitted to the faculty of the University of North Carolina at Chapel Hill in  
partial fulfillment of the requirements for the degree of Doctor of Philosophy in the  
Department of Chemistry (Polymer and Materials).

Chapel Hill  
2009

Approved by

Joseph DeSimone

Valerie Ashby

Marcey Waters

Michael Rubenstein

Etta Pisano

Abstract  
Kevin Patrick Herlihy  
Shape and Size Specific:  
Fabrication, Characterization, and Application of Highly Tailored Biocompatible Hydrogel  
Particles for Use in Materials and Biomedical Settings  
(Under the direction of Joseph M. DeSimone)

This work details the method development of a bench top process designed to fabricate highly defined particles of uniform shape and size. In this method, perfluorinated elastomeric molds were patterned off of etched silicon wafers and other substrates. These molds were then filled with a pre-particle solution that was subsequently solidified by UV photoradical initiated polymerization. Particle harvesting by physical agitation and a variety of sacrificial adhesive layers was examined. Purification of particles was also explored using multiple techniques including: centrifugation, dialysis, and a variety of filtration techniques. Regioselective chemical and metallic surface functionalization was demonstrated. Direct particle analysis was performed using microscopic techniques and indirect analysis of particle loading and surface chemistry was performed using spectrophotometric, fluorescence, and mass spectrometry techniques.

Micron scale particles were fabricated with a variety of shapes, sizes, chemistries, and cargos for materials applications. It was determined that particle shape dictated how particles with an induced dipole moment aligned and crystallized in alternating electric fields. Control over chaining and alignment with respect to particle orientation was gained when particles were loaded with superparamagnetic cargo.

Nanometer scale particles with different form factors were also fabricated for *in vivo* imaging and biodistribution studies in small animals. The particles ranged in size from 80 nm to 2000 nm in length. Particles were surface modified with poly(ethylene glycol) for protection from the reticuloendothelial system. The particles contained or were surface modified with one or more contrast agent including near infrared fluorescent dye, iron oxide nanoparticles (for Magnetic Resonance Imaging), or  $\text{Cu}^{64}$  for Positron Emission Tomography. This research laid the groundwork for future experiments in targeted delivery of therapeutics to tumors using the template based particle fabrication technology.

To my cheerleader, nurse, wife, and bff.

To my parents.

To Buster and Savannah.



The author would first like to thank Janine Nunes with whom I coauthored two manuscripts. Second, it is important to acknowledge the countless troubleshooting / brainstorming sessions that Elizabeth Enlow and I had. Third, Timothy Merkel deserves recognition and acknowledgement for his help in particle fabrication, his level headedness under pressure, and for helping me on the long nights spent during the animal studies as I dove headfirst into the unknown realm of radiochemistry. In addition the author would like to thank the army of scientists that helped him along the way: Curtis Bergquist for help with early particle design; Dr. Dorian Canelas for useful discussions on science and coauthoring a review on nanotherapeutics and imaging agents; Benjamin Evans and Lamar Mair of Prof. Richard Superfine's Lab for helpful discussions on magneto-polymer composites; Briana Carstens of Prof. Richard Superfine's lab for the vibrating magnetometry work; Dr. Wallace Ambrose and Amar Kumbhar of Chapel Hill Nanofabrication Labs for technical TEM assistance; Dr. C. Robert Bagnell for confocal microscopy assistance; Jeremy Niskala of Prof. Wei You's lab for metal evaporation assistance; Carlos Villas and Prof. David Scheinberg of Memorial Sloan Kettering Cancer Center; Prof. Hong Yuan, Prof. Hongyu An, and Dr. Bryan Yoder of the Biomedical Research and Imaging Center of UNC Chapel Hill for help with small animal imaging; Dr. Gary Bordanero, Dr. Robert Ilic, and Dr. Meredith Metzler of the Cornell Nanofabrication Facility who were very helpful in the fabrication of silicon wafers with  $2 \times 2 \times 1 \mu\text{m}^3$ ,  $2 \times 2 \times 4 \mu\text{m}^3$ ,  $2 \times 2 \times 6 \mu\text{m}^3$  rectangular features, and  $10 \times 4 \times 1 \mu\text{m}^3$  boomerang

features; Liquidia Technologies, Inc. for Fluorocur<sup>®</sup> and 80 x 360 nm and 80 x 2000 nm patterned PFPE molds; This work was supported by the STC program of the National Science Foundation (CHE-9876674), National Institutes of Health Carolina Cancer Center for Nanotechnology (5-U54-CA119373-02), and DARPA (07-4627). Finally, the author acknowledges his advisor Joseph DeSimone for taking him in and turning him into a scientist.

## Table of Contents

Section 1: Particle Fabrication Methods Using the Particle Replication In Non-wetting Template (PRINT) Technique.....	1
1.1 Overview of Particle Fabrication.....	1
1.1.1 Bottom-Up Approaches to Particle Fabrication.....	2
1.1.2 Top-Down Approaches to Particle Fabrication.....	4
1.1.2.1 Hard-Template Approaches to Top-Down Particle Fabrication.....	5
1.1.2.2 Microfluidics Approaches to Top-Down Particle Fabrication.....	6
1.1.2.3 Mechanical Stretching as a Top-Down Approach to Particle Fabrication.....	8
1.1.2.4 Photolithographic Approaches to Top-Down Particle Fabrication.....	10
1.1.2.5 Imprint Lithography Approaches to Top-Down Particle Fabrication.....	11
1.2 Particle Replication In Non-wetting Templates (PRINT).....	14
1.2.1 PRINT Overview.....	14
1.2.2 Master Fabrication.....	16
1.2.3 Mold Fabrication.....	18
1.2.5 Particle Curing and / or Solidification.....	21
1.2.6 Particle Harvesting.....	21
1.2.7 Particle Purification.....	23

1.2.8 Particle Surface Modification.....	26
1.2.9 Particle Characterization.....	26
1.2.9.1 SEM.....	27
1.2.9.2 TEM.....	27
1.2.9.3 AFM.....	28
1.2.9.4 Particle Stability.....	29
1.2.9.5 Particle Concentration.....	30
1.3 Summary.....	31
References.....	32
Section 2: Shape and Size Specific Contrast Agent Fabrication, Characterization and Early Biodistribution Studies.....	37
2.1 Introduction to Nanomedicine and Nanodiagnostics.....	37
2.2 Background on Nanotherapeutics.....	38
2.3 Background on Nanoparticle Imaging Agents.....	44
2.3.1 MR Imaging.....	44
2.3.2 Positron Emission Tomography.....	48
2.3.3 Near Infrared Fluorescence Imaging.....	49
2.4 Multimodal Shape and Size Specific Contrast Agents Fabricated Using the PRINT Process.....	49
2.4.1 Particle Composition.....	50
2.4.2 Particle Fabrication, Harvesting, and Purification.....	51
2.4.3 Particle Surface Functionalization.....	56
2.4.3.1 Surface Functionalization with DOTA-bz-SCN.....	56
2.4.3.2 Surface Functionalization with PEG-NHS.....	58

2.4.3.3 “Cold” Copper Chelation.....	59
2.4.3.4 <sup>64</sup> Cu Chelation.....	60
2.5 Particle Characterization.....	61
2.5.1 Particle Concentration and Iron Oxide Content Determination by Thermogravimetric Analysis.....	61
2.5.2 Dynamic Light Scattering and Zeta Potential Analysis.....	61
2.5.3 Determining Available Primary Amine Concentration by Kaiser Assay Analysis.....	61
2.5.4 Determining DOTA Surface Concentration by Arsenazo III Transchelation Assay Analysis.....	63
2.5.5 Characterization of Near Infrared Particle Fluorescence.....	64
2.5.6 Characterization of MRI Particle Contrast.....	65
2.5.7 Characterization of PRINT Particles as PET Contrast Agents.....	66
2.6 In Vivo Imaging Study.....	68
2.6.1 In Vivo PET/CT Results.....	69
2.6.2 In Vivo Near Infrared Fluorescence Results.....	74
2.6.3 In Vivo MRI Results.....	77
2.7 Summary.....	78
2.8 Future Directions.....	79
References.....	82
Section 3: Microscale Particle Fabrication and Analysis.....	86
3.1 Alignment and Crystallization of Electrically Polarizable Anisotropic Particles Fabricated Using the PRINT Process.....	86

3.1.1 Introduction to the Alignment and Crystallization of Electrically Polarizable Anisotropic Particles.....	86
3.1.1.1 Particle Fabrication Background.....	87
3.1.1.2 Dielectrophoresis.....	88
3.1.2 Experimental.....	89
3.1.2.1 Particle Composition.....	89
3.1.2.2 Master Fabrication.....	90
3.1.2.3 Mold fabrication.....	90
3.1.2.4 Monomer Solution.....	90
3.1.2.5 Particle Fabrication.....	91
3.1.2.6 Particle Harvesting.....	92
3.1.2.7 Particle Purification.....	93
3.1.2.8 Sample Preparation.....	93
3.1.3 Experimental Setup.....	93
3.1.3.1 Electrical Cell Setup.....	93
3.1.3.2 Imaging.....	94
3.1.3.3 Turbidity Experiments.....	95
3.1.4 Results and Discussion.....	95
3.1.4.1 Particle Stability.....	95
3.1.4.2 Particle Fabrication Results.....	97
3.1.4.3 Particle Alignment and Crystallization Experimental Results.....	99
3.1.4.4 Dielectrophoresis Summary.....	108
3.2 Fabrication and Magnetic Manipulation of Shape and Size Specific Magneto-Polymer Composite Particles.....	110

3.2.1 Introduction and motivation for the Fabrication of Magneto-Polymer Composite Particles.....	110
3.2.2 Fabrication of Magnetic Hydrogel Composites with Random and Linear Magnetic Domains.....	113
3.2.2.1 General Particle Composition.....	113
3.2.2.2 Nano-scale Particle Fabrication.....	114
3.2.2.3 Micro-scale Particle Fabrication.....	115
3.2.2.4 Directionality of Linear Chains of Magnetite.....	117
3.2.3 Magnetic Manipulation of Microscale Composite Particles.....	120
3.2.4 End-labeled Composite Particles and Their Use as Micromotors.....	122
3.2.4.1 End-labeling Composite Particles.....	122
3.2.4.1 Background of Micromotor Particles in H <sub>2</sub> O <sub>2</sub> .....	124
3.2.4.2 Micromotor Particles in H <sub>2</sub> O <sub>2</sub> in a Stationary Magnetic Field.....	127
3.2.4.2 Micromotor Particles in H <sub>2</sub> O <sub>2</sub> in a Rotating Magnetic Field.....	129
3.2.5 Magneto-Polymer Composites Summary.....	129
References.....	131

## List of Tables

1.1	Comparison of swelling behavior of PDMS versus PFPE coupons in a variety of organic solvents.....	15
2.1	Multimodal shape and size specific particle composition.....	51
2.2	Zeta potential of 200 x 200 nm cylindrical particles as a function of pH and number of PEGylations.....	59
2.3	Particle half-life in blood circulation.....	72
2.4	Ratio of the AUC of the lungs to the liver and lungs to the spleen at 45 minute and 24 hour exposure times p.i. as a function of particle size.....	73
3.1	Particle dimensions and critical aggregation values.....	99
3.2	Particle composition and attributes of the PFPE mold and films used for particle fabrication.....	113
3.3	Translational particle velocities in stationary magnetic fields.....	129



## List of Figures

1.1	Template-based particle fabrication techniques.....	6
1.2	Microfluidic approaches to particle fabrication.....	8
1.3	Particle fabrication by mechanical stretching.....	10
1.4	Photolithographic approaches to particle fabrication.....	11
1.5	Schematic of the PRINT method.....	13
1.6	Illustrative examples of particles made using the PRINT method.....	16
1.7	Scanning electron micrograph of 200 x 200 nm PRINT particles.....	27
1.8	Transmission electron micrograph of magnetite filled PRINT particle.....	28
1.9	Atomic force micrograph of a PFPE mold.....	29
2.1	Schematic representation of the PRINT process.....	40
2.2	Examples of magneto-polymer composites from the literature.....	46
2.3	AFM images of empty molds for each of the four particle sizes.....	52
2.4	SEM images of particles of each particle size fixed to a PET harvesting layer.....	53
2.5	Titration of particle by addition of 25 mM NaOH.....	54
2.6	SEM images of free particles of each particle size drop cast from aqueous solution.....	55
2.7	TEM images of all particle sizes containing iron oxide nanoparticles.....	56
2.8	Zeta potential of DOTA-functionalized 200 x 200 nm cylindrical particles as a function of the pH.....	58

2.9	Standard curve showing the linear relationship of absorbance at 405 nm vs primary amine concentration.....	62
2.10	Standard curve demonstrating the linear relationship of absorbance at 630 nm vs the concentration of DOTA.....	64
2.11	NIRf phantom study of particles in 2 wt % agarose gel was performed to determine an estimate of the limit of detection for particles <i>in vivo</i> .....	65
2.12	T1 Map of standard dilution phantom (left) and plot of T1 relaxation time vs particle concentration (right).....	66
2.13	Cartoon of tail vein catheter setup.....	69
2.14	Dynamic PET scan (t = 0 – 60 min) and two static scans (6 and 24 hrs) of a mouse injected with 200 x 200 nm cylindrical particles.....	71
2.15	Averaged SUV data (n = 3 mice) for particle accumulation in the liver, spleen, lung and heart.....	72
2.16	NIRf images of a control mouse with no injected particles (A), a mouse injected with 200 x 200 nm cylindrical particles at 1.5 hrs (B), and the same mouse at 24 hrs (C).....	75
2.17	NIRf images of lungs (A), liver (B), spleen (C), and kidney (D) of mice injected with 200 x 200 nm PRINT particles.....	76
2.18	Particle accumulation determined by NIRf as a function of particle size at 24 hrs p.i.....	77
2.19	<i>In vivo</i> MRI scans of a mouse injected with 200 x 200 nm cylindrical particles containing iron oxide nanocrystals.....	78
3.1	Literature examples of self-assembly of shape and size specific particles.....	87
3.2	Schematic of the PRINT method.....	92
3.3	Dielectrophoretic cell schematic.....	94
3.4	Turbidity measurements of hexnut particles in three concentrations of CTAB.....	96

3.5	Turbidity measurements of all four micron sized particles in CTAB.....	96
3.6	Scanning electron micrograph of each of the four particle shapes.....	98
3.7	Schematic describing particle orientation.....	100
3.8	Fluorescence micrographs of particles dispersed and aligned by dielectrophoresis.....	102
3.9	Fluorescence micrographs and cartoon schematics of crystalline particle configurations.....	104
3.10	Low magnification fluorescence micrographs of aligned particles in solution.....	106
3.11	Fluorescence micrographs of hexnut and rod-shaped particles on the gold electrode.....	108
3.12	Atomic Force micrographs of particles on a harvesting layer.....	114
3.13	Scanning and Transmission electron micrographs of rice and worm-shape particles containing magnetite.....	115
3.14	Fluorescence micrograph of boomerang-shaped particles in the mold with increasing amounts of magnetite.....	116
3.15	Schematic detailing the alignment of chains of magnetite in PRINT particles.....	117
3.16	Fluorescence micrograph of particles with differing orientations of magnetite.....	119
3.17	Flourescence micrograph of magneto-polymer composite particles aligned in a magnetic field.....	121
3.18	SQUID magnetization curves of particles with magnetite in different orientations within the particle.....	122
3.19	Schematic detailing the end-labeling and movement of H <sub>2</sub> O <sub>2</sub> rocket particles.....	124
3.20	Schematic of magnetic stage set up for particle chaining experiments in water.....	126

3.21	Multiframe fluorescence overlay of one $\text{H}_2\text{O}_2$ rocket in $\text{H}_2\text{O}_2$ as magnetic direction is changed.....	127
3.22	Schematic detailing the microscope setup for $\text{H}_2\text{O}_2$ rocket experiments.....	128

## List of Abbreviations and Symbols

AC – Alternating Current

AEM – Aminoethyl methacrylate

AFM – Atomic Force Microscopy

AIBN – 2,2-bis-azobutronitrile

APMA – Aminopropyl methacrylamide

Ar – Argon

Au – Gold

AUC – Area Under the Curve

BRIC – Biomedical Research and Imaging Center

C<sub>4</sub>F<sub>8</sub> – Octafluoroethylene

Ci – Curie

CNF - Cornell Nanoscale Science and Technology Facility

CT - Computed Tomography

CTAB – Hexadecyltrimethylammonium bromide

DEAP – Diethoxyacetophenone

DEP – Dielectrophoresis

d.i. – Deionized

DLS – Dynamic Light Scattering

DMF – Dimethylformamide

DMSO – Dimethylsiloxane

DOTA - 1,4,7,10-tetraazacyclododecane-1,4,7,10-tetraacetic acid

DTPA - Diethylenetriaminepentaacetic acid

EDS – Energy Dispersive Spectroscopy

EDTA – Ethylenediamine tetraacetic acid

ESEM – Environmental Scanning Electron Microscope

Fe<sub>3</sub>O<sub>4</sub> – Magnetite

FFF – Flow Field Fractionation

Gd – Gadolinium

H – Applied Magnetic Field

H<sub>2</sub>O<sub>2</sub> – Hydrogen peroxide

HCl – Hydrochloric acid

HCPK – 1-hydroxycyclohexylphenyl ketone

HMDS – Hexamethyl disylazane

Hz – Hertz

i.d. - injected dose

IACUC – Institutional Animal Care and Use Committee

iTLC – Instant Thin Layer Chromatography

mN/m – MilliNewton per meter

MRI – Magnetic Resonance Imaging

N<sub>2</sub> – Nitrogen

NH<sub>4</sub>OH – Ammonium hydroxide

NHS – N-hydroxy succinimide

NIRf – Near Infrared Fluorescence

nm – Nanometer

O<sub>2</sub> - Oxygen

Pd – Palladium

PDMS – Poly(dimethyl siloxane)

PEG – Poly(ethylene glycol)

PET – Poly(ethylene terphthalate)

PET - Positron Emission Tomography

PFPE – Perfluoropolyether

PPE - Personal protective equipment

PRINT – Particle Replication In Non-wetting Templates

PS – Poly(styrene)

PTFE – Poly(tetrafluoroethylene)

PVA – Poly(vinyl alcohol)

PVDF – Poly(vinylidene fluoride)

PVP –Poly(vinyl pyrrolidone)

RES – Reticulo Endothelial System

ROI - Region of interest

SCK – Shell Crosslinked Knedel-like particles

SEM – Scanning Electron Microscopy

SPECT - single photon emission computed tomography

siRNA – small interfering RNA

SF<sub>6</sub> – Sulfur hexafluoride

SFI-L – Step and Flash Imprint Lithography

SFL – Stop Flow Lithography

SQUID – Superconducting Quantum Interference Device

T – Tesla

TEM – Transmission Electron Microscopy

TFF – Tangential Flow Filtration

TGA – Thermogravimetric Analysis

UNC-CH – University of North Carolina at Chapel Hill

UV – Ultraviolet

V – Volt

VP - 1-vinyl-2-pyrrolidinone

$\lambda$  – Denotes wavelength

$\mu$  – “micro”

$\mu$  – Micrometer

$^{\circ}\text{C}$  – Degrees Celsius

$\phi$  – Volume fraction



## **Section 1: Particle Fabrication Methods Using the Particle Replication In Non-wetting Template (PRINT) Technique**

### **1.1 Overview of Particle Fabrication**

Colloidal particles, those particles with an average diameter of 10 micrometers or less, have been studied in detail for varied applications in catalysis, electronics, photovoltaics, coatings, cosmetics, smart fluids, therapeutics, and diagnostics among others. While the vast majority of colloidal particles are spherical in nature, nonspherical, or anisotropic particles, have potential to lead to advancements in all of these applications and more. Anisotropic colloidal particles, for example are capable of assembling into structures which are distinct from the hexagonal close packed arrangements favored by spherical particles and are of interest in the fields of memory storage, optical electronics, photonics and sensors (see Section 2).<sup>1,2</sup>

Anisotropic colloidal particles are exciting, however, not only because of the changes in optical, electrical, and other material properties, but also because of a wealth of advantageous biomedical properties. Precisely designed biodistribution profiles, for example, are highly sought after and it is believed that shape specific colloids may hold the key. In addition, enhanced tissue targeting and the ability to tote biologically relevant cargo such as therapeutics or imaging agents make the study of these particles very intriguing.

Considerable effort has been devoted to the development of fabrication methods that can produce colloidal particles with fine control over size, shape, composition, cargo

and surface chemistry. A number of different approaches towards particle fabrication are briefly reviewed in this section with an emphasis on the control over shape and size that each different technique is capable of. One technique in particular, the Particle Replication In Non-wetting Templates (PRINT®) method is highlighted as an ideal method for the fabrication of monodisperse colloids with precise control over the size, shape, material composition, and surface chemistry of the resulting particles. The varying aspects of PRINT are detailed below; from master and mold fabrication steps that lay the foundation of the process all the way to finishing touches of particle fabrication including purification and stability measurements. This section is a summary of lessons learned in particle fabrication and is designed to provide a detailed snap shot of the ever-evolving PRINT process.

#### **1.1.1 Bottom-Up Approaches to Particle Fabrication**

Two broad approaches are amenable for the fabrication of anisotropic particles: bottom-up and top-down techniques. Bottom-up approaches begin at the atomic or molecular scale and build up to the desired particle size, while top-down methods process a material on the desired size scale. The most commonly employed methods for the production of mass quantities of particles on the colloidal length scale are bottom-up synthetic approaches such as emulsion polymerization. In a typical process, a monomer is emulsified via rapid stirring in a mobile phase that contains an initiator and a surfactant. Upon heating to activate the initiator, spherical particles are nucleated in the surfactant micelles and grow to the desired size. Particles obtained by emulsion methods are typically spherical and can vary in size from tens of nanometers to several microns in diameter. The particle size and the molecular weight of the polymers formed in emulsions are controlled with parameters such as the surfactant concentration and reaction temperature. Surfactant

adsorbed onto the surface of these particles can be difficult to remove if undesired. While this method is extremely scalable, the particles fabricated in this way are typically spherical in shape, can have large polydispersities and are limited in chemical composition.

Particles with non-spherical shape are of increasing interest for biomedical applications such as drug delivery, where the rod-like or corkscrew morphologies possessed by many viruses and bacteria are suspected to have derived an evolutionary advantage from their specific shapes.<sup>3</sup> Crystals of many metals and metal-oxides can be grown into both spherical and anisotropic shapes such as cubes, rods, discs and faceted polyhedra using nucleation and arrested growth strategies.<sup>1, 4, 5</sup> More complex branched structures can be formed by sequential growth of dots and rods of different materials.<sup>6</sup> Such nucleation and growth methods are limited to inorganics and the shape selectivity is highly dependent on the material and its crystal structure. Further, these inorganic materials often lack the capability to encapsulate a cargo or undergo surface modification.

Bottom-up approaches for the fabrication of organic particles have received a great deal of attention for use in biomedical applications such as imaging, gene or drug delivery. These methods chiefly rely on self-assembly of amphiphilic molecules to create micelles, vesicles, liposomes, and polymersomes. The hydrophobic interior is able to encapsulate a hydrophobic cargo. While spherical particles have been the standard, increasing attention has been directed towards higher aspect ratio particles (particles that are taller than they are wide) that are achievable with control of the relative length of hydrophobic and hydrophilic domains.<sup>3, 7-9</sup>

An example of high aspect ratio particles was recently demonstrated by Discher, *et al.* who explored filamentous polymersomes called filomicelles for their circulation

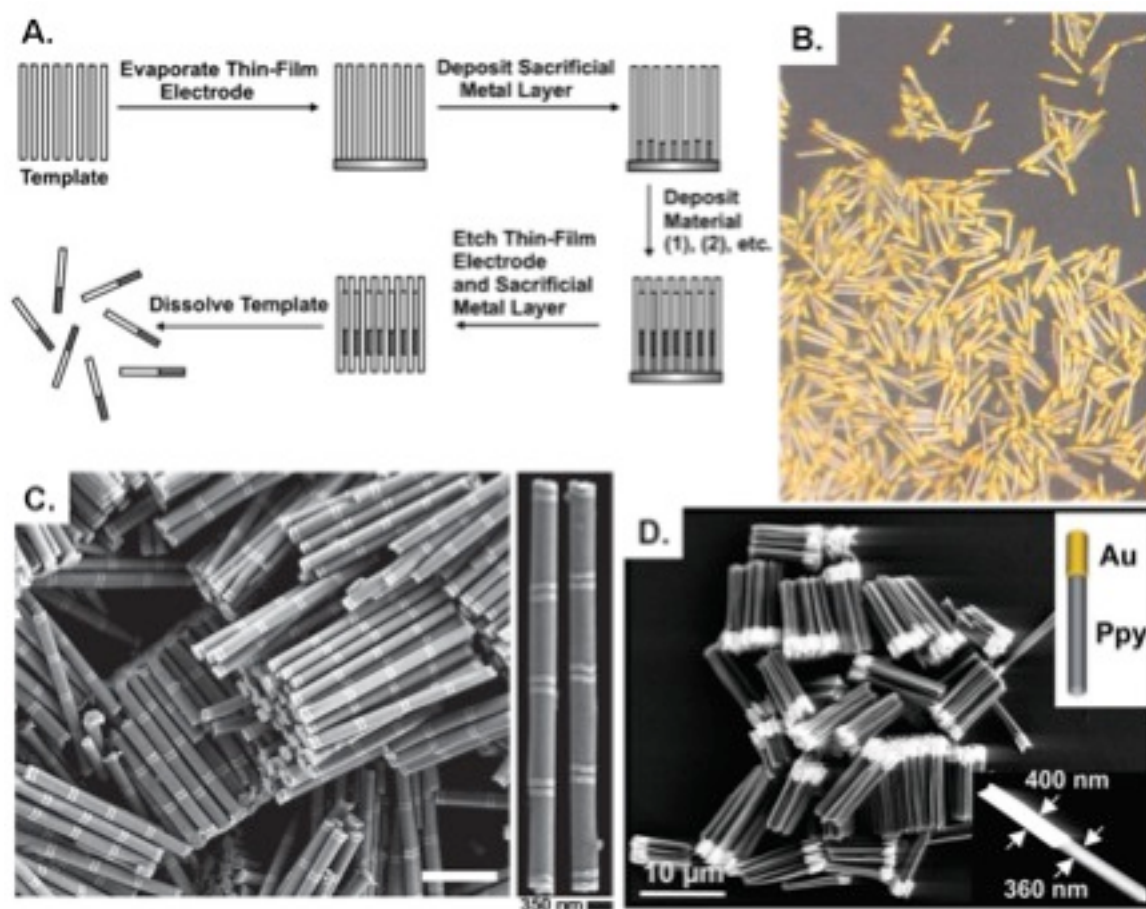
persistence and ability to encapsulate and deliver chemotherapeutics. The filomicelles were prepared from block copolymers with lipid-like amphiphilicity, but a more symmetric ratio of hydrophilic to hydrophobic blocks than is found in lipids. These filamentous particles persisted in the circulation about ten times longer than spheres with similar surface chemistry, and were successful in encapsulating and delivering a hydrophobic chemotherapeutic to tumored mice.<sup>9</sup> One criticism of these self-assembled systems is the dynamic nature of the particles so assembled. With membrane components held together with attractive forces rather than with covalent bonds, the structures generated can add or lose components, making their size and shape more fluid than may be desired. The dynamic nature of these self-assembled systems has been addressed by Wooley *et al.* with shell-cross linked knedel-like particles (SCKs).<sup>10-13</sup> These block copolymer micelles are modified with reactive groups on the surface which can be chemically cross-linked after self-assembly, giving superior stability to their structure.

### **1.1.2 Top-Down Approaches to Particle Fabrication**

Top-down approaches to particle fabrication rely on tools, rather than surface energy and thermodynamics like so many bottom-up approaches, to tailor the size and shape of particles. “Crude” top-down methods are popular in the fabrication of bulk materials. Examples of this include milling and grinding in which particle size distributions are highly disperse and shape is very irregular. Sorting for particle size is possible using a variety of techniques including sieves and fractionation. A number of new top-down techniques have been developed that offer substantial benefits in the control over size and shape. Examples of these techniques include template based, microfluidic, mechanical stretching, and photolithographic approaches.

### **1.1.2.1 Hard-Template Approaches to Top-Down Particle Fabrication**

Hard-template methods have been used to prepare nanowires, nanotubes and nanorods.<sup>14-17</sup> In this technology, porous templates are filled with one or more materials to fabricate monodisperse nanoparticles. Traditionally, the templates are filled via electrochemical means. This is accomplished by first depositing a sacrificial metal layer, such as gold or silver, on one side of the template for electrical contact. Then, the material or materials of interest are electrochemically deposited into the pores of the template. For example, metals can be synthesized using the appropriate electroplating solution, and conducting polymers can be synthesized via oxidative polymerizations. After deposition, the template is dissolved yielding an ensemble of nanoparticles connected at the base to the substrate metal. The connecting sacrificial metal layer is then dissolved to generate a monodisperse suspension of high aspect ratio nanoparticles. Both tubes and solid wires or rods can be prepared depending on the surface treatment of the template.<sup>18</sup> One major advantage of the template method is that segmented or multicomponent nanoparticles can be fabricated in a rational fashion (Figure 1.1).<sup>19, 20</sup> This has led to an impressive breadth of research into the area of post-fabrication modifications of segmented nanoparticles.<sup>21</sup> Multicomponent nanorods can be selectively functionalized for different multiplexing, sensing and self-assembly applications.<sup>21, 22 23, 24</sup>



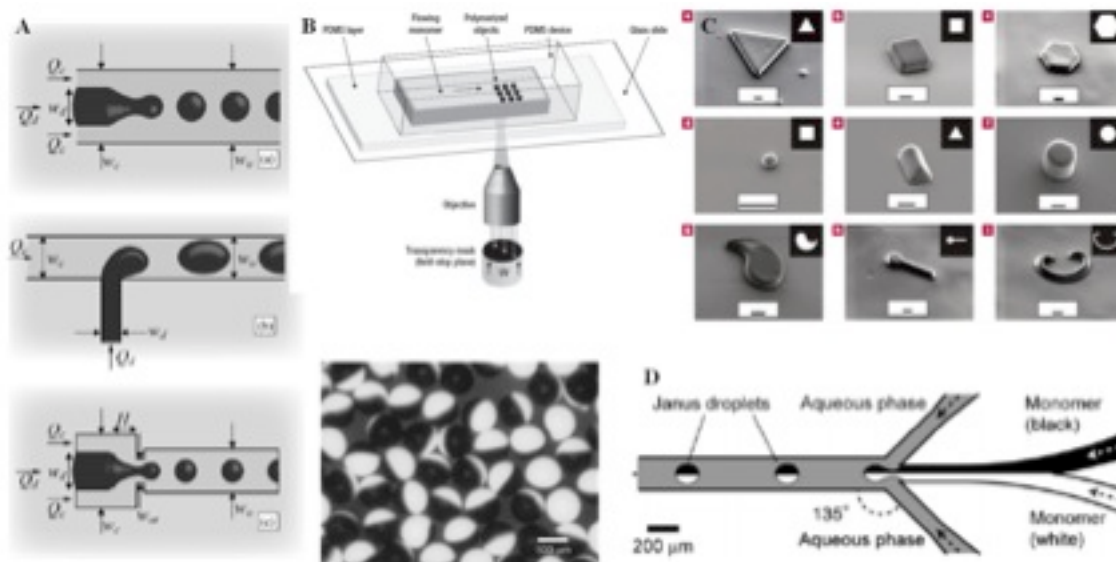
**Figure 1.1.** (A) General scheme for nanorod synthesis via the deposition of materials into a nanoporous template,<sup>19</sup> (B) Bright-field optical micrographs of Au/Pt/Au rods,<sup>22</sup> (C) SEM images of Au-Ni multisegmented nanorods,<sup>23</sup> and (D) SEM image of Au-polypyrrole rods.<sup>20</sup>

#### 1.1.2.2 Microfluidics Approaches to Top-Down Particle Fabrication

One emerging strategy for the fabrication of particles with control over particle size and shape is fabrication with microfluidic devices. In early microfluidic particle fabrication studies, the shapes produced in these channels were limited to spheres, cylinders and spherically derived shapes such as discs and ellipsoids. More complex and chemically anisotropic shapes such as hemispheres<sup>25</sup>, core-shell<sup>25</sup> and janus particles<sup>26</sup> were produced by confining the droplets with the geometry of the device and with coflowing laminar streams, though these remain derivatives of the original spherical shape. Recently, the Doyle group

has developed photolithographically coupled approaches, which have produced more complex shapes by use of a photolithographic mask.<sup>27, 28</sup> Particles were crosslinked by the UV light exposure almost instantaneously, and did not plug up the channel due to the oxygen mediated inhibition of polymerization at PDMS surfaces, which left a thin layer of unpolymerized monomer at the channel walls.<sup>29</sup> Exposures across several fluid streams resulted in the formation of janus type particles with two or more chemically distinct regions on each particle.<sup>27, 30</sup> Higher resolution has been achieved with the use of stop-flow lithography (SFL), a process during which the flow of monomer was stopped briefly during each exposure. Complex shapes have been formed with high resolution in the micron scale, including a range of concave and convex sided pyramids, rectangles, and spheres, and rectangular toroids - all with multiple, chemically distinct phases possible.<sup>28, 31</sup>

Microfluidic methods have demonstrated their versatility in terms of particle shape and chemical anisotropy of the particles produced (see Figure 1.2). The emergence of SFL techniques have increased the resolution of this technique though there are material limitations; particles made in this way have been limited to polymerizable fluids and selection of the mobile phase has been limited due to the swelling of the device material, PDMS, in many solvents. Another limitation has been the size of particles which can be produced with these methods. Particles on the order of 3-100  $\mu\text{m}$  were readily fabricated, but sub-micron particle sizes remain a challenge for microfluidic technology.



**Figure 1.2.** (A) Illustrations of the three main microfluidic geometries used for droplet formation,<sup>32</sup> (B) A schematic used for continuous-flow lithography and (C) microparticles of varying shapes fabricated with this method,<sup>27</sup> (D) Right: A schematic for the channel and flow configuration used for the formation of the bicolored janus particles shown on the left.<sup>33</sup>

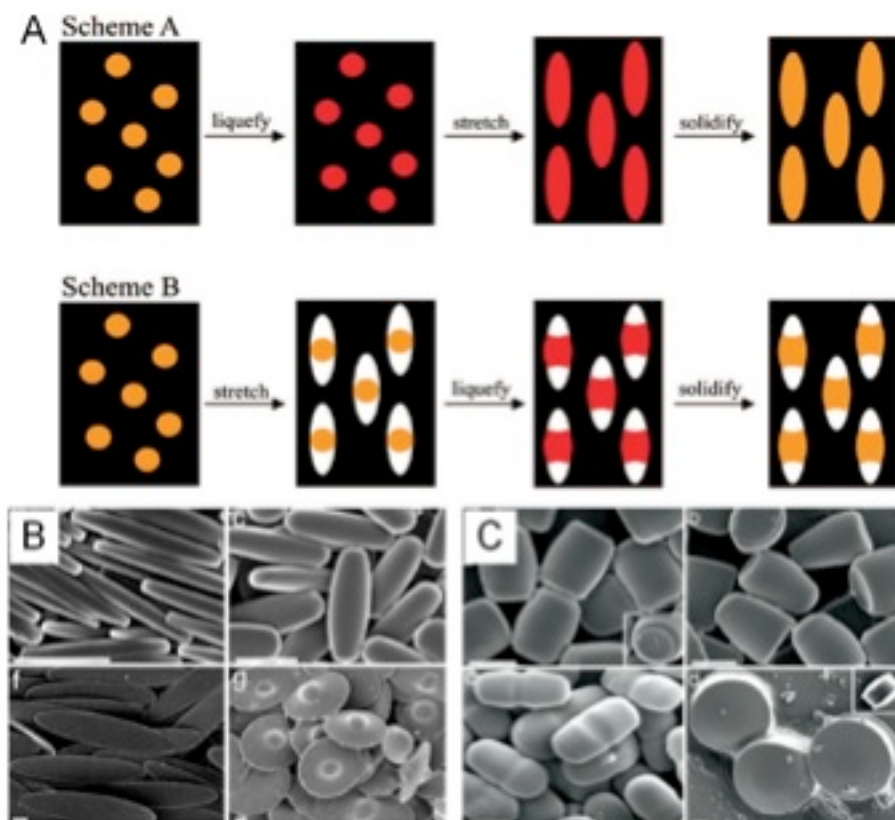
### 1.1.2.3 Mechanical Stretching as a Top-Down Approach to Particle Fabrication

One relatively new method for the fabrication of shape and size specific colloids relies on the mechanical stretching of spherical particles. Particle stretching was initially used to deform polystyrene (PS) particles that were embedded in a polyvinyl alcohol (PVA) film. Upon heating to a temperature at which the particles could deform, the film was stretched, then rapidly quenched, yielding ellipsoidal particles upon dissolution of the PVA film.<sup>34</sup> Recently, Champion *et. al.* reported the formation of complex shapes via a similar method (Figure 1.3). In this method, as before, (PS) particles were embedded in a PVA film. The PS particles were liquidized by addition of heat or solvent, allowing the PS to flow, filling void spaces in the surrounding film, or to stretch with the film due to hydrogen bonding based attraction to the surrounding film. Manipulation of the PS particles required exposure to temperatures on the order of 140 °C or organic solvents (toluene), which places some limits on the encapsulation of cargos by these particles. Careful modifications to the



stretching protocol allowed for selective formation of over twenty distinct particle shapes upon solidification of the particles by cooling or removal of solvent and subsequent release from the PVA film.<sup>35</sup>

One distinct advantage of the particle stretching technique has been the ability to compare differently shaped particles with identical volumes by preparing different particle shapes from the same stock of spherical particles. Material compatibility is a concern for this method, as the bulk of the literature deals with PS and poly(lactic-co-glycolic acid) (PLGA) based particles – though one can imagine that many materials could be manipulated in this way by adjusting the conditions used to fluidize the particles and the material in which the particles are embedded. This method is versatile with respect to particle size, as spherical PS particles with diameters from 60 nm to 100  $\mu$ m have been subjected to these stretching protocols. Polydispersity of the particles prepared by stretching methods was reflected by the polydispersity in the spherical particles before stretching. Careful selection of a spherical particle source could lead to the formation of more monodisperse populations of stretched particles.



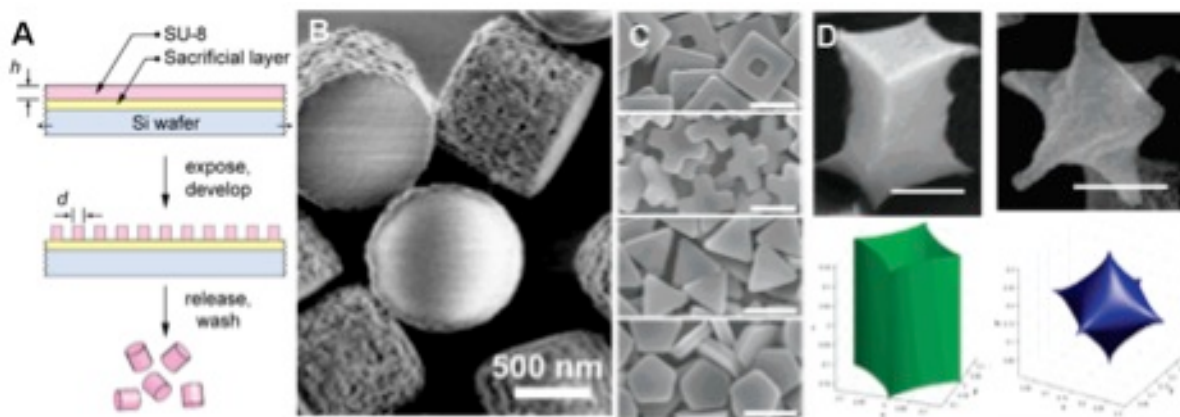
**Figure 1.3.** (A) The two general schemes used in stretching spherical particles to different shapes. In Scheme A, particles are liquefied prior to stretching the film, while Scheme B has the film stretched prior to particle liquidification. (B) Polystyrene particles prepared via the method shown in scheme A. (C) Polystyrene particles prepared Scheme B.<sup>35</sup>

#### 1.1.2.4 Photolithographic Approaches to Top-Down Particle Fabrication

Photolithography, the workhorse of the semiconductor industry for high volume manufacturing<sup>36, 37</sup>, has also been directly applied to the fabrication of discrete monodisperse colloidal particles.<sup>38-41</sup> A simple illustration of this process is shown in Figure 1.4A. Both Mason *et al.*<sup>39</sup> and Stroock *et al.*<sup>42</sup> have reported using this type of approach to generate highly monodisperse, shape-specific colloidal particles. Stroock *et al.*<sup>43</sup> demonstrated the ability to tailor the surface roughness of the particles by modifying the development conditions (Figure 1.4 B). Mason *et al.*<sup>39</sup> illustrated the shape versatility of this process by generating particles with a wide range of shapes (Figure 1.4 C), including all 26 letters of the

English alphabet. The fabrication of the lithographically-derived particles, or LithoParticles as coined by Mason, was also found to be amenable to the incorporation of both organic dyes and nanoparticles such as iron oxide. It was even feasible to fabricate hybrid bilayer Janus particles, through the successive exposure of two different masks.

Clear advantages of this type of processing include excellent shape fidelity down to the submicrometer level and the ability to fabricate particles in a high throughput fashion. A major stumbling block for using this process is the enormous capital required to continuously run such an expensive lithographic exposure system. Another issue with this type of processing is the limitations in the chemistries that can be used in the particle fabrication. These issues have led to the development of alternative routes to LithoParticle production that take advantage of templating, where only the initial reusable template requires photolithography.<sup>44, 45</sup>



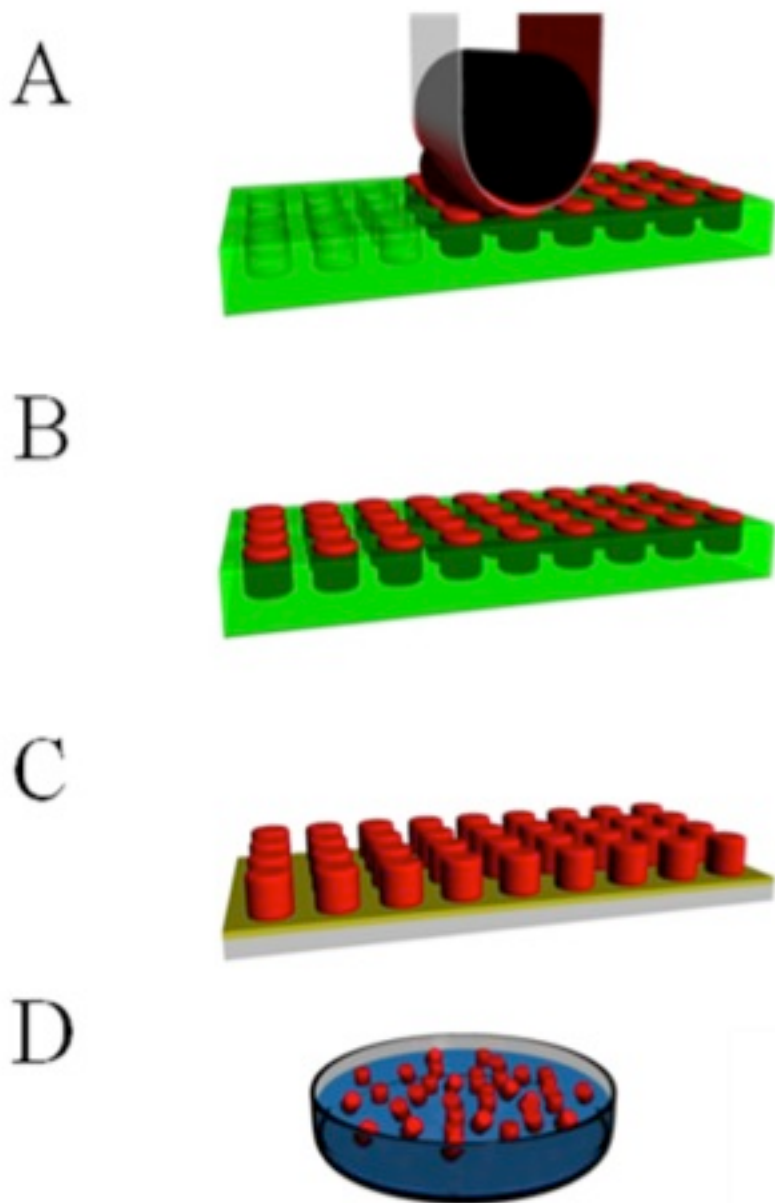
**Figure 1.4.** (A) Simple scheme showing the photolithographic fabrication of colloidal particles,<sup>42</sup> (B) Cylindrical photoresist particles engineered with rough side walls (particle radius = 520 nm, height = 875 nm),<sup>43</sup> (C) Photoresist particles of varying shapes (scale bars represent 3 μm): square donuts, square crosses, triangular prisms and pentagonal prisms (from top to bottom),<sup>39</sup> and (D) 4-valent and 6-valent nanoparticles fabricated using interference lithography (scale bars represent 300 nm).<sup>40</sup>

#### 1.1.2.5 Imprint Lithography Approaches to Top-Down Particle Fabrication

Imprint lithography based methods have emerged in recent years as promising techniques for scalable fabrication of shape specific colloidal particles. Soft lithography based techniques, which were pioneered by Whitesides et al. in the late 1990's, begin with the use of a rigid template which is used to fabricate an elastomeric mold, which can then be used to replicate the shape of the original template in a molding or stamping process.<sup>46</sup> Imprint methods were first envisioned as a high-resolution, low-cost alternative to traditional photolithographic techniques for micro- and nanoscale pattern replication rather than fabrication of distinct particles. Particle fabrication has been a challenge due in large part to the persistent formation of a residual layer of molded material, called a flash layer, which connects the potential particles.<sup>47</sup> Much attention has been directed towards the removal or avoidance of this flash layer with the goal of particle fabrication. Step and flash imprint lithography (S-FIL) uses a rigid, UV transparent template as a mold material, creating an embossed film of particles from a UV curable material. The interconnecting flash layer is removed by an etching step, with dissolution of a sacrificial layer yielding distinct particles.<sup>48, 49</sup> Removal of the flash layer via an oxygen plasma etch can be energetically expensive and time consuming.

Soft lithography applications that utilize crosslinked poly(dimethyl siloxane) (PDMS) elastomer, typically result in particles connected by a flash layer. Recently, microparticles were fabricated with PDMS molds without formation of a flash layer by careful applications of photocurable acrylate resins, as well as aqueous and organic solutions of polymers, to the molds.<sup>50</sup> Surface treatments were shown to increase or decrease the hydrophilicity of the mold, facilitating mold-filling, mold de-wetting, and particle release.<sup>51, 52</sup> PRINT technology (Figure 1.5), which utilizes a fluorinated elastomeric mold in an imprint lithographic

technique, allows for facile fabrication of distinct particles without formation of a flash layer while maintaining many of the advantages of the soft lithography technique and avoiding some of the difficulties associated with PDMS.<sup>53</sup>



**Figure 1.5:** A general schematic representation of the PRINT process. (A) A pre-particle solution (red) is distributed evenly in the elastomeric mold (green) by a roller (black) with a high surface energy polymer sheet, which wicks away excess solution. (B) The particle solution is solidified in the mold. (C) Particles are removed from the mold with a harvesting film (yellow). (D) Dissolution of the film yields free flowing particles in solution.

## 1.2 Particle Replication In Non-wetting Templates (PRINT)

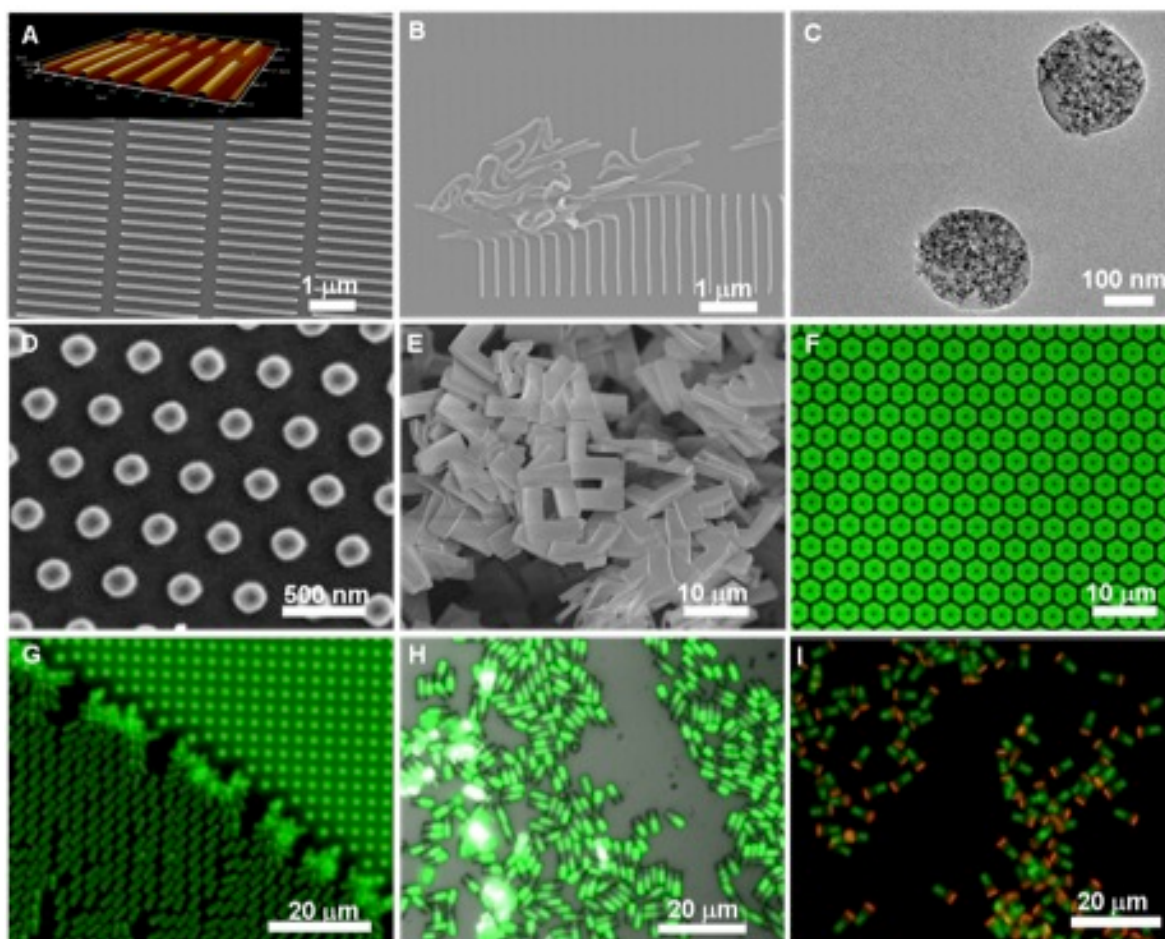
### 1.2.1 PRINT Overview

In 2004, Rolland et al. reported the synthesis of a new perfluoropolyether (PFPE) based elastomer<sup>54</sup>, a material that proved to be more effective than PDMS as a template for soft lithography based particle fabrication. Photocurable PFPE (Fluorocur<sup>TM</sup>, Liquidia Technologies Inc., NC) was synthesized by endcapping a fluorinated PFPE diol (Solvay) with isocyanatoethyl methacrylate to form PFPE dimethacrylate. The end-functionalized fluorinated oil had a positive spreading coefficient allowing it to completely wet and envelope the delicate details of a master template. Curing of the oil was accomplished under UV light (365 nm, ~10-15,000 mJ/cm<sup>2</sup>) after the addition of a photoinitiator. The resulting PFPE elastomers have three distinct advantages over silicone templates for use in soft lithography. First the low surface energy of the elastomer (8-10 dyn/cm)<sup>55</sup> facilitates the removal of an excess flash layer. Other lithographic methods typically require an etch step to remove this layer, complicating the scale up of these methods.<sup>46, 56</sup> Second, PFPE was observed to be compatible with a number of organic solvents that were incompatible with silicone molds.<sup>54</sup> It was found that, while both Sylgard 184 (a silicone material) and PFPE molds exhibited negligible swelling in the presence of water and methanol, Sylgard 184 molds were permeable to toluene and dichloromethane. An examination of several other common solvents and polymerizable organics showed a similar trend, with PDMS coupons generally showing a higher retention of these organic fluids (table 1.1). With the elimination of swelling, master-to-replica fidelity was improved and the reproduction of much smaller feature sizes was possible. In 2006, Maynor et al. showed that a variety of nanoscale artifacts could be reproduced using the PRINT technique including 60 nm adenoviruses, 45

nm polymeric toroidal micelles, and single walled carbon nanotubes with heights as low as 2 nm.<sup>55</sup> Third, the highly fluorinated nature of the mold (similar to that of Teflon<sup>TM</sup>) facilitated the removal of particles from the mold. In contrast, other soft lithography methods required surface modification of the molds to facilitate particle removal.<sup>51, 52</sup> A number of published manuscripts are available describing a wide variety of particles fabricated using the PRINT technique (Figure 1.6)<sup>8, 53, 57-64</sup>

**Table 1.1.** A comparison of swelling behavior, reported as the percent increase in weight of coupons of crosslinked elastomeric materials after soaking overnight. Traditional soft lithography mold material, poly (dimethylsiloxane) (PDMS), and PRINT mold material, perfluoropolyether (PFPE) were compared with regards to several solvents and polymerizable monomers.<sup>65</sup>

	<b>PDMS (weight % uptake)</b>	<b>PFPE (weight % uptake)</b>
<b>Water</b>	0.37 ± 0.04	0.39 ± 0.16
<b>Hexane</b>	109.82 ± 1.41	1.72 ± 0.25
<b>THF</b>	145.46 ± 1.68	6.95 ± 0.08
<b>DMSO</b>	2.36 ± 0.50	1.98 ± 0.17
<b>Isopropanol</b>	17.65 ± 2.44	2.38 ± 0.06
<b>Acetone</b>	20.15 ± 1.05	4.81 ± 0.06
<b>Poly (ethylene glycol) methyl ether</b>	1.04 ± 0.45	0.36 ± 0.07
<b>2-hydroxyethyl acrylate</b>	1.45 ± 0.23	1.03 ± 0.22
<b>N-Vinyl-2-pyrrolidone</b>	5.55 ± 0.31	2.34 ± 0.27
<b>PEG triacrylate</b>	1.40 ± 0.06	0.31 ± 0.05



**Figure 1.6.** Illustrative examples of size, shape, composition, cargo and surface chemistry control with the PRINT process (A-B) 80 nm x 2000 nm worm-like cross-linked poly(ethylene glycol) (PEG) nanoparticles on a harvesting layer, inset showing AFM image of harvested layer, (C) 10 wt. % iron oxide-loaded 200 nm cylindrical cross-linked PEG particles, (D) siRNA-loaded 200 nm albumin nanoparticles harvested onto a medical adhesive, (E) boomerang-shaped cross-linked PEG microparticles, (F) hexnut-shaped cross-linked PEG microparticles on a cyanoacrylate harvesting layer, (G-I) 2x2x6 mm cross-linked PEG rectangular prisms showing increasing chemical anisotropy: (G) one-phase, (H) biphasic, and (I) triphasic. D<sup>62</sup> and H, I.<sup>66</sup>

### 1.2.2 Master Fabrication

Typically, patterned silicon wafers were used as masters from which a pattern is transferred to a PFPE mold. Fabrication of silicon masters was performed using standard photolithographic instrumentation and techniques. In its most basic form, photolithography is a process in which a thin film of photoresist on a silicon wafer is exposed to light that has



passed through a patterned reticle. The light induces a change in solubility in the photoresist. In a positive photoresist, whatever is exposed becomes soluble. This change in solubility is typically due to the cleavage of a photoacid generator group pendant to the backbone of the polymer. In negative photoresists crosslinking occurs upon exposure to light that eliminates the ability to dissolve the exposed regions. After exposure and removal of the soluble portion of the photoresist, one of any number of etching processes can be used to etch the silicon. Finally, cleaning steps are used to remove residual photoresist from the wafer. Achievable feature sizes for each technique are largely dictated by the wavelength of light that is used to expose the photoresist.

Patterned masters with micron scale features were fabricated at the Cornell Nanoscale Science and Technology Facility (CNF). Briefly, 4 x 4" chrome on glass reticles (50 mm field size) were either fabricated using a Heidelberg DWL66 Mask Writer or they were purchased from Holographix, LLC. Feature sizes in the reticle were 5 times the size of the desired features of the master. Wafers were cleaned with 1:1  $\text{NH}_4\text{OH}:\text{H}_2\text{O}_2$  then with 1:1  $\text{HCl}:\text{H}_2\text{O}_2$  and were rinsed with d.i. water and dried (a process known as metal-oxide semiconductor (MOS) cleaning). Wafers were then primed for photoresist with hexamethyl disylazane (HMDS) using a YES LP-III vacuum oven. Next, the wafers were placed in a Brewer Science CEE Model 600 and were coated with SPR 220-3.0 photoresist which was spun cast at 5000 rpm for 60 seconds. The wafers were baked at 115 °C for 60 seconds to remove residual solvent then cooled to room temperature. Photoresist along the edge of the wafer was removed to facilitate later etching steps. After edgebead removal, micron scale feature sizes (0.5, 1, 2, 3, 5, 7 and 10  $\mu\text{m}$ ) were exposed into photoresist using a GCA Autostep 200 DSW i-line (365 nm laser) wafer stepper with a 5 x reduction lens. The

exposed photoresist was then developed with 300 MIF developer for 60 seconds using a Hematech-Steag Wafer Processor. An O<sub>2</sub> plasma clean was then performed to remove excess photoresist. To etch the silicon, a Bosch Etch procedure was employed using a Unaxis 770 couple plasma/reactive ion etcher. The etching process used C<sub>4</sub>F<sub>8</sub>, SF<sub>6</sub>, and Ar gases for an etch rate of 1 μm/minute. Finally, any residual photoresist was removed from the wafers in a two part process involving first, a two tank hot resist strip bath/rinse/dry cycle and second, a 15 second oxygen plasma removal cycle a Branso P2000 barrel etcher. Silicon masters were characterized by SEM.

Masters with smaller feature sizes (< 500 nm) were provided by Liquidia and were typically made using 193 nm photolithography technology. Other lithographic techniques with even higher resolution are available. E-beam photolithography for example, is capable of creating 10-20 nm feature sizes. Another technique using self assembled block copolymer masters have been shown to be effective in highly regular feature sizes smaller than 20 nm.<sup>67</sup>

### **1.2.3 Mold Fabrication**

Initially, mold fabrication was performed by drop casting 20-30 mL of Fluorocur resin onto a 6-8 inch diameter patterned silicon master template that was then cured photochemically in a UV oven.<sup>53</sup> Molds were released from the template by slowly peeling them back from silicon wafer using PTFE tweezers so as not to scratch the fragile surface features. Because of the delicate nature and the high cost associated with using large quantities of Fluorocur Resin for the thick molds, the scale of particle production was limited. With this in mind, a proprietary roll-to-roll system capable of producing thousands of linear feet per day of PFPE molds on a flexible poly (ethyleneterephthalate) (PET) backing, was recently engineered by Liquidia Technologies, Inc. The new process yields

more mechanically robust molds and reduces the Fluorocur resin requirements by several orders of magnitude making the process more time effective, less costly, and highly scalable.

Thin molds have also been successfully fabricated in the lab. Typically, a 500  $\mu\text{L}$  aliquot of Fluorocur is gently spread over a silicon master using a sheet of PET specially treated for adhesion with PFPE. Air bubbles are removed from between the master and the PET by peeling the PET all the way off of the PFPE-wetted master surface and *gently* rolling the PET back over the master using a small hand roller. The master/PFPE/PET sandwich is then placed in a UV oven which is then purged of  $\text{O}_2$  using  $\text{N}_2$ . The mold is cured for 3 minutes and allowed to cool to room temperature. The mold is then gently peeled off the master revealing a clean mold bound to a PET backing sheet.

#### **1.2.4 Mold Filling**

Filling of any patterned mold is a process that relies heavily on surface energies of the materials in play. In order to effectively fill the cavities, a pre-particle solution should have the ability to partially wet the surface of the mold. Solutions capable of wetting the surface of a mold are drawn into the mold cavities by capillary forces. At this point excess pre-particles solution covers the entire surface of the mold in what is referred to as a flash layer. Excess pre-particle solution was removed by first laminating the filled mold with a high surface energy material (i.e. PET, surface energy =  $42.1 \text{ mN/m}$ )<sup>68</sup> and second, peeling back the laminate material. Capillary forces trap the liquid in the mold while excess solution adheres preferentially to the high surface energy material and is wicked away, leaving isolated reservoirs of pre-particle solution, thus eliminating the need for a scum removal step.

Film thickness of the pre-particle solution, like surface energy, also plays an important role in effective large scale particle fabrication. Films that are too thick make the

removal of excess solution difficult and often lead to the formation of scum. Films that are too thin lead to patchy filling or shortened particles. As such, uniform films were drawn on a PET sheet using a metal Mayer rod with grooved surface features and a mechanical film coating instrument (R.D. Speicalties Inc). Film thickness was dictated by both the grooved feature size of the Mayer rod and the concentration of the pre-particle solution. Best results were observed when the film thickness was on the order of the feature height of the mold. For example, a 200 nm tall particle would fill best with a 200 nm film. In addition, it was determined that performing the filling and splitting steps in one continuous movement provided the best results.

Unlike patterning on a solid substrate, or with a rigid patterned template which can be time consuming, patterning of the pre-particle solution can be done in a continuous fashion when the template and pre-particle solution are both on flexible backing. Other particle fabrication methods like S-FIL involve a step by step procedure in which a master template is brought into contact with a solid substrate in the presence of a pre-particle solution, a step that can damage the master template if performed without care. In the PRINT process, after a uniform film was cast on PET as described above, the PET was laminated to an empty mold using an in-house single-nip lamination system. Lamination conditions (pressure, speed, temperature, and humidity) were optimized for each new class of particle. Monomer-based pre-particle films that flowed freely into the cavities of the mold and had low vapor pressure were laminated at room temperature.<sup>61</sup> Volatile monomers and other small molecule systems required that the lamination temperature be reduced and that the lamination take place in glove bag or other controlled environment. Polymeric films like PEG or PLGA

sometimes required heat to raise the temperature of the film above the glass transition temperature of the polymer allowing the polymer to flow into the mold.

### **1.2.5 Particle Curing and / or Solidification**

While the majority of “Top Down” particle fabrication processes rely on photochemical curing, particle solidification using the PRINT technique can be quickly accomplished by a variety of different methods. Monomer systems incorporating a small amount (~ 1 % or less) photochemical initiator such as 1-hydroxycyclohexyl phenyl ketone or 2,2-diethoxyacetophenone (HCPK and DEAP, Aldrich) were cured in a UV chamber.<sup>63</sup> Some monomeric pre-particle systems that were sensitive to light were instead cured thermally using a temperature sensitive initiator such as 2,2-bis-azobutronitrile (AIBN, Aldrich). Polymeric systems cast from a solvent were dried and solidified under vacuum while neat polymeric systems were dropped below their glass transition temperatures causing them to become glassy and solid. Small molecule and protein based “biological” systems that were cast from a solution were typically lyophilized.<sup>62</sup>

Particle solidification, regardless of the chemical process of solidification, was typically performed either closed-faced, with a PET sheet laminated to the surface of the filled mold or open-faced<sup>69</sup> with the filled mold exposed to a N<sub>2</sub> purge. Solidified particles trapped in the mold or bound to a harvesting layer of PET could be harvested immediately or wound up and stored until harvesting at a later date.

### **1.2.6 Particle Harvesting**

In early particle fabrication experiments using the PRINT method, removing particles from the mold was initially performed by physical agitation of the particles with the sharp end of a glass slide.<sup>59</sup> A number of problems were associated with this harvesting technique.

First, this method was found to damage the surface of the molds creating large chunks of PFPE mold that would have to be filtered out later. Second, scraping dry particles could cause them to aerosolize. And third, the harvesting process was not scalable. With the introduction of thinner molds from, scraping caused even more damage to the molds than with the thick PFPE molds because there was less elastomeric material to dampen the force of the scraping glass edge.

As a result, new harvesting techniques were developed that were more gentle, safe, and scalable. If solidified with an open face as noted above, the particles in the mold could be laminated to an adhesive layer such as poly(vinyl pyrrolidone) (PVP) or cyanoacrylate on a flexible or rigid backing such as PET or glass slides. Once the adhesive solidified, the mold was peeled away from the substrate revealing an array of free-standing particles. The adhesive was then dissolved and the particles collected in solution. This method was found to be especially useful for larger micron scale particles that required the strength of cyanoacrylate to be removed from the mold.

While this method appears straightforward in its implementation, it can be difficult to successfully harvest particles in this manner. The reasoning behind this, is that particles are strongly trapped within the cavities of the mold by capillary forces and Van der Waals interactions with the PFPE. As a result a great deal of force is required to remove the particles from the mold. This means that any adhesive used to perform this task needs to have strong interactions with the surface of the particle. Therefore the sacrificial adhesive layer needs to be chosen with each particle's surface chemistry in mind. Hydrophilic particles should be harvested with hydrophilic adhesives etc.

If the particles were solidified with a closed face (laminated to PET), the particles adhered to the raw PET once the mold was peeled back. This works well for particles that are hydrophobic in nature (ie. triacrylate or poly(styrene)-co-poly(butadiene)). For particles that are more hydrophilic (ie. particles with long PEG chains or charged monomers), the surface energy of PET was readily increased through the process of corona surface treatment. Pre-treated PET sheets (Melinex 453) were also used for higher surface energy removal of hydrophilic particles. Caution here is necessary as curing particles in the presence of a surface that is too similar in nature can lead to irreversible binding of the particles to the surface. Once removed from the mold, free-standing particles that are physisorbed to a sheet of PET can be harvested by lamination to another adhesive layer or by physical agitation with a soft rubber cell scraper in the presence of a solvent.

### **1.2.7 Particle Purification**

Regardless of the fabrication method, after harvesting, particles made from “Top-down” techniques generally require some form of purification to remove debris or residual compounds from the fabrication process, and also to prepare particles for their intended use. As mentioned above, when using AAO as a template, particle fragmentation often occurred.<sup>70</sup> Even particles that only required minimal manipulation by physical stretching on a sheet of PVA required multiple rinsing steps to remove excess PVA from solution.<sup>35</sup> Fortunately, a wide variety of purification methods are currently available and it is usually possible to find at least one method that fits well with a particle fabrication technique.

Dialysis (>100,000 MWCO, Float-a-lyzer, Spectrum Labs, Inc) was originally used for PRINT particle fabrication to remove impurities such as sol fraction and to exchange buffer solutions. This method was found to be a relatively slow and ineffective process

because particles were often physisorbed to the membrane surface. In a typical purification, spent solvent had to be switched for clean solvent at least three times over the course of 1-2 days.

Centrifugation is perhaps the simplest method of particle purification and it is used widely as a quick method to rinse particles and separate various sized populations of particles gravimetrically.<sup>58</sup> In centrifugation, particles are spun out of solution under high centrifugal forces. As particle size decreases, the centrifugal speed and the time required to effectively pellet out particles effectively increases. Particle yield can be reduced when centrifugation is halted prematurely. As such, purification of small stable particles, less than a few hundred nanometers in diameter, can be quite time consuming requiring hours or days to fully pellet a sample. Other problems including irreversible aggregation may be encountered when particles are centrifuged for long periods (>1hr) at high speed (14,000 rpm / 20,000 G). Additionally, resuspending pelleted particles by vigorous mixing and/or sonication can damage particles composed of less robust matrix materials or with high aspect ratios as well as fragile cargos, such as proteins and other biologically active cargo, and should be performed with care.

Centrifugal filtration using 0.1  $\mu\text{m}$  cutoff poly(vinylidene fluoride) (PVDF) membranes (Microcon-MC, Millipore) proved to be an efficient alternative to standard centrifugation. Lower speeds are required than normal filtration and therefore aggregation is typically reversible. Unfortunately, once spun down, particles are partially adhered to the PVDF membrane. The strength of particle adhesion to the membrane depends strongly on both the chemistry of the particles as well as that of the membrane. Removal of particles from the membrane was found to be optimal when the membrane was physically removed



from its housing and sonicated in solution. While a variety of polymeric membranes and pore sizes are available making this technique adaptable for a variety of particle fabrication methods, particle loss is often dramatic (as much as 50% loss of mass), and the batch process with repeated rinsing can be slow and therefore it is not ideal for high throughput particle fabrication.

Filtration using indirect or tangential flow filtration (TFF) systems appeared to be the most promising approach for particle purification. In TFF filtration systems such as KrosFlo (Spectrum Labs, Inc) particle solutions traveled tangential to the membrane. Both diafiltration as well as concentration are possible without changing particles from one set up to another. Particle loss by adsorption to the membrane and to surfaces was reduced as particles were not forced to interact directly with the membrane or multiple vials and/or pipet tips. Stirred Cell filtration (Millipore), another indirect filtration method, was also examined. While this method of purification appears promising, inadequate stirring can lead to filters clogged with particles creating prolonged filtration times. Additionally, if the cell is allowed to run dry, dramatic loss of particle yield is observed due to irreversible adhesion of the particles to the filter membrane.

Other methods of particle purification are also under development. Magnetic purification for example is currently being used for particles containing magnetic cargo. While it was strictly limited to magnetic particles, this method, using magnetic columns (Minisep, Miltenyi Biotec) appeared promising for purification and other functionalized particle applications. In addition to magnetic filtration, Flow Field Fractionation (FFF) is of interest for future purification and separation of particles as particle aggregation is not as prevalent as in other centrifugal techniques.

### **1.2.8 Particle Surface Modification**

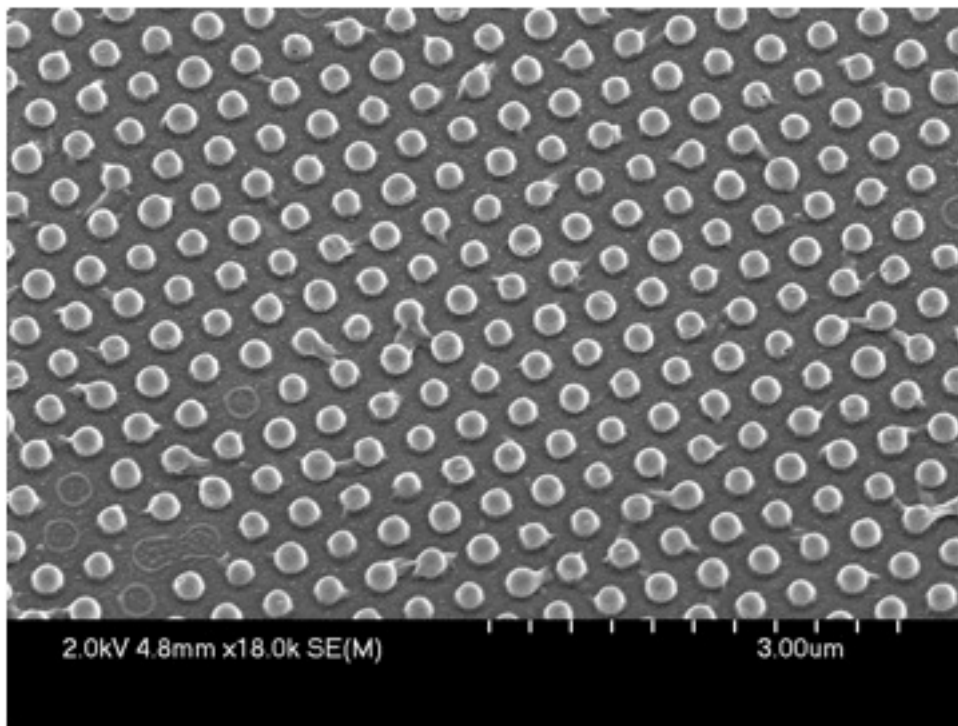
One unique feature of template based particle fabrication is that solidified particles, either in the mold or on a harvesting layer of PET, are easily subjected to a number of regiospecific chemical modifications.<sup>66</sup> Chemical modification of particles while in the mold made it possible to manipulate one face of the particle. Once removed from the mold, modification of particles on a harvesting layer allowed the manipulation of the remaining sides of the particle. This is an exciting development for a number of fields of research including nano- and microrobotics<sup>71-73</sup> and targeted drug delivery.<sup>66</sup> Ongoing research in our lab is focused towards directed cellular uptake of regio-modified particles as well as the beginnings of shape-specific building blocks for directed assembly in smart fluids and microrobotics applications.

### **1.2.10 Particle Characterization**

Particles were analyzed using a number of different techniques. Techniques for imaging particles included scanning electron microscopy (SEM), transmission electron microscopy (TEM), atomic force microscopy (AFM), optical and fluorescence microscopy. Surface chemistry and stability was determined using dynamic light scattering (DLS), zeta potential analysis, and turbidity as well as a number of other indirect assays that are described in detail in later sections. Particle concentration was typically determined gravimetrically using a thermogravimetric analysis (TGA) instrument. While individually, each method provided one or two attributes of a particular particle sample, typically a combination of the above characterization techniques was required to get the full picture of what a particle sample was. Below are typical conditions and sample preparations for each characterization technique.

### 1.2.10.1 SEM

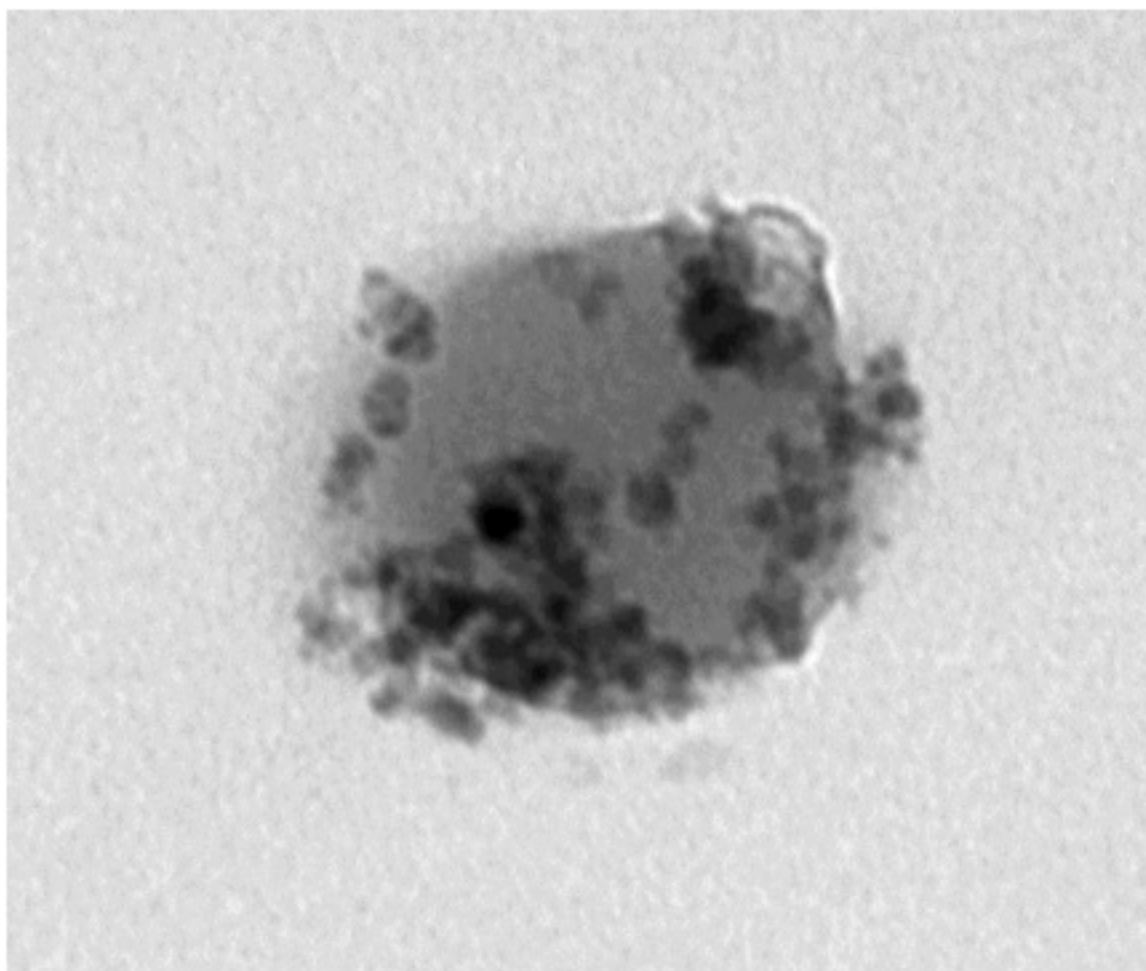
SEM was used as a method to rapidly examine particle morphology. Particle samples were imaged by SEM in an array (ie. harvesting layer) or cast from solution. When cast from solution, particles were thoroughly rinsed with filtered deionized (d.i.) water then drop cast in low (0.001 mg / mL), medium (0.1 mg / mL), and high (1-10 mg / mL) concentrations onto a clean glass slide. After drying at room temperature the particles were coated using with 3 - 5 nm gold / palladium using a Model 108 Auto Sputter Coater (Cressington Scientific Instruments). Particles were then imaged using a Hitachi model S-4700 SEM at 2 kV acceleration voltage. A typical SEM of 200 x 200 nm PEG-based PRINT particles is shown in Figure 1.7.



**Figure 1.7** Scanning electron micrograph of 200 x 200 nm cylindrical particles on a harvesting layer of PET.

### 1.2.10.2 TEM

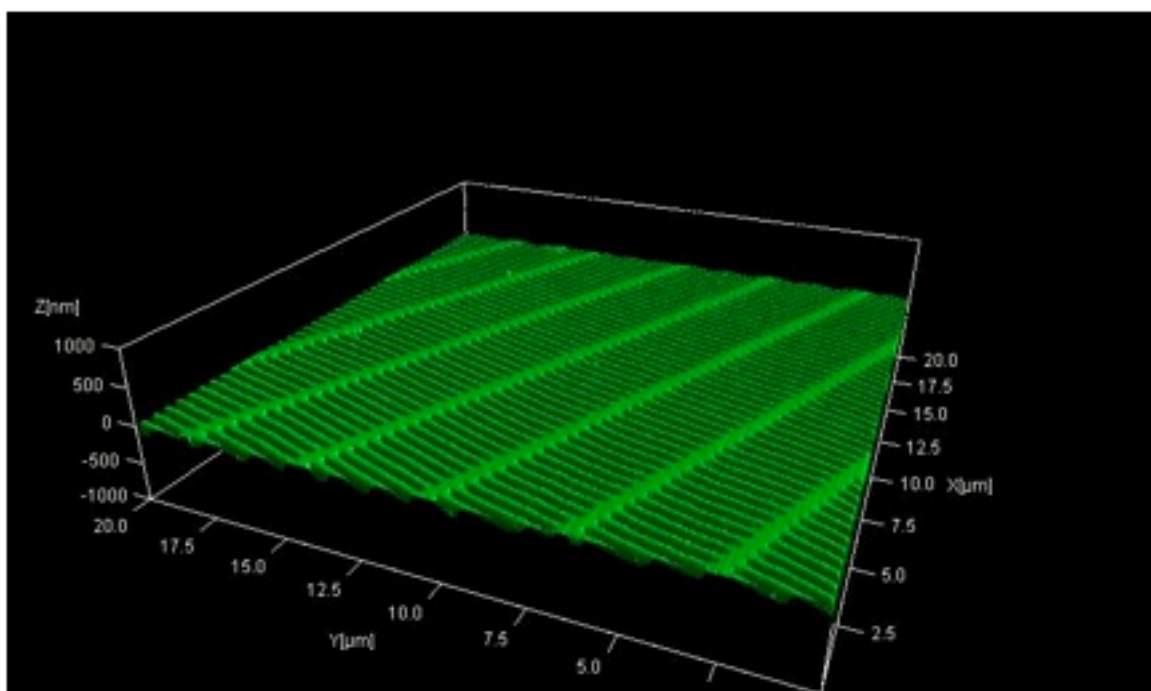
TEM was often used to examine the loading of magnetic iron oxide into the core of the particle. Samples were prepared by dipping a carbon-formvar coated TEM grid into aqueous dispersion of particles of varying concentrations (see above). The samples were wicked dry using a piece of filter paper and allowed to dry completely at room temperature. Samples were then imaged as is using a Jeol 100 CX II instrument with a 40 kV acceleration voltage operating in bright field mode. A typical example of a 200 x 200 nm particle with encapsulated iron oxide nanoparticles is demonstrated in Figure 1.8.



**Figure 1.8** Transmission electron micrograph of 200 x 200 nm cylindrical particle containing 10 wt % iron oxide nanocrystals.

#### **1.2.10.3 AFM**

Samples were typically imaged in an array in order to determine the depth of filling in the mold itself or to determine the height of particles on a harvesting layer. Samples were prepared for AFM by adhering a small square to the sample stage using cyanoacrylate adhesive which was allowed to dry at room temperature for 10 minutes. The sample was then imaged using a Nanosurf Easyscan 2 AFM (Nanoscience, Inc.) in dynamic contact mode using an ACLA tip. Examination of an 80 x 2000 nm patterned PFPE mold by AFM is demonstrated in Figure 1.9.



**Figure 1.9** Atomic force microscopy image of a patterned PFPE mold with 80 x 2000 nm “worm-like” surface features. The AFM image shows that the mold is clean and free of defects.

#### 1.2.10.4 Particle Stability

Particle stability was determined either by dynamic light scattering or by turbidity experiments, a spectrophotometric technique that monitors the transmittance of light through a particle dispersion over time. Samples were prepared for DLS and Zeta potential experiments by dilution of particles ( $\sim 0.001 - 0.050$  mg / mL) in a low concentration

electrolyte (1.0 mM NaCl). Typically, both Zeta and DLS experiments were performed at 25 °C and could be run in the same cuvette using the Malvern Instruments Zetasizer Nano ZS equipped with an autotitrator. Particle polydispersity and hydrodynamic radius were determined. Low polydispersity ( $PDI < 0.1$ ) and particle sizes slightly larger than the feature size of the mold used to make the particle indicated that the particles were stable and had not formed large aggregates in solution. Particle isoelectric points were determined using this instrument providing crucial information on the operational pH range of the particles.

Turbidity was useful in determining how stable concentrated samples of particles were. Particle samples (5-20 mg/mL) were prepared in 0.2, 1.0, and 5.0% (w/v) aqueous CTAB solutions. The particle sample in a cuvette (100  $\mu$ L, QS) with a path length of 1 cm was then vortex mixed and placed in a plate reader (Spectra Max M5, Molecular Devices). A kinetic experiment was performed at 490 nm, and an absorbance reading was taken every 30 s for 1 h at 22 °C. All experiments were repeated three times to establish reproducibility. The turbidity,  $\tau$ , defined as the attenuation of the light beam by scattering when passing through a sample, was determined from equation 1.1, where  $I_o$  is the incident intensity of light,  $I_t$  is the transmitted intensity, and  $l$  is the optical path length. See Section 3 Chapter 2 on particle stability for an example of turbidity experiments.

$$\lambda = l^{-1} \ln(I_o / I_t) \quad (\text{eq. 1.1})$$

#### 1.2.10.5 Particle Concentration

Accurate particle concentration was essential for all experiments and particle analysis. Therefore a rapid, effective means of particle concentration determination using TGA was developed. In a typical experiment, a 25  $\mu$ L aliquot of purified particle dispersion in d.i. water (typically cloudy to the eye) is placed in a pre-tared aluminum pan on the TGA.

The sample is then heated well above 100 °C (typically 130-105 °C) to drive the evaporation of all water. The sample is then cooled to room temperature. Particle concentration is calculated as the dry particle mass divided by the initial sample mass.

### **1.3 Summary**

An increase in demand for monodisperse, shape and size specific colloidal particles for both the academic and industrial sectors has driven the development of multiple new synthetic techniques for colloidal particle fabrication. While a number of fabrication techniques have been shown to make such shape and size specific particles, all such methods, until now, have exhibited a number of inherent disadvantages. The DeSimone Lab has developed a scalable platform for particle fabrication that surmounts all of these obstacles. The current state of the art in bench top particle fabrication using the PRINT technique was detailed as it was used during my studies at UNC. Fabrication of the particles was described from start to finish with an emphasis on the most basic methods used for making and analyzing the particles. The following sections will describe in greater detail three projects that were based on particles fabricated using the PRINT technique.

## References

1. Glotzer, S. C.; Solomon, M. J., *Nat Mater* **2007**, 6 (7), 557-562.
2. Velev, O. D., *Science* **2006**, 312 (5772), 376-7.
3. Champion, J. A.; Katare, Y. K.; Mitragotri, S., *J Control Release* **2007**, 121 (1-2), 3-9.
4. Glotzer, S. C.; Solomon, M. J., *Nature materials* **2007**, 6 (8), 557-62.
5. Rosi, N. L.; Mirkin, C. A., *Chemical reviews* **2005**, 105 (4), 1547-62.
6. Milliron, D. J.; Hughes, S. M.; Cui, Y.; Manna, L.; Li, J.; Wang, L. W.; Alivisatos, A. P., *Nature* **2004**, 430 (6996), 190-5.
7. Champion, J. A.; Mitragotri, S., *Pharmaceutical research* **2009**, 26 (1), 244-9.
8. Gratton, S. E.; Ropp, P. A.; Pohlhaus, P. D.; Luft, J. C.; Madden, V. J.; Napier, M. E.; DeSimone, J. M., *Proceedings of the National Academy of Sciences of the United States of America* **2008**, 105 (33), 11613-8.
9. Geng, Y.; Dalhaimer, P.; Cai, S.; Tsai, R.; Tewari, M.; Minko, T.; Discher, D. E., *Nature nanotechnology* **2007**, 2 (4), 249-55.
10. Thurmond, K. B., 2nd; Remsen, E. E.; Kowalewski, T.; Wooley, K. L., *Nucleic acids research* **1999**, 27 (14), 2966-71.
11. Sun, G.; Hagooly, A.; Xu, J.; Nystrom, A. M.; Li, Z.; Rossin, R.; Moore, D. A.; Wooley, K. L.; Welch, M. J., *Biomacromolecules* **2008**, 9 (7), 1997-2006.
12. Qi, K.; Ma, Q.; Remsen, E. E.; Clark, C. G., Jr.; Wooley, K. L., *Journal of the American Chemical Society* **2004**, 126 (21), 6599-607.
13. Nystrom, A. M.; Xu, Z.; Xu, J.; Taylor, S.; Nittis, T.; Stewart, S. A.; Leonard, J.; Wooley, K. L., *Chemical communications (Cambridge, England)* **2008**, (30), 3579-81.
14. Al-Mawlawi, D.; Lui, C. Z.; Moskovits, M., *J. Mater. Res.* **1994**, 9 (4), 1014-1018.
15. Cai, Z.; Martin, C. R., *J. Am. Chem. Soc.* **1989**, 111 (11), 4138-4139.
16. Martin, C. R., *Science* **1994**, 266 (5193), 1961-1966.
17. Preston, C. K.; Moskovits, M., *J. Phys. Chem.* **1993**, 97 (32), 8495-8503.



18. Brumlik, C. J.; Martin, C. R., *J. Am. Chem. Soc.* **1991**, *113* (8), 3174-3175.
19. Hurst, S., J.; Payne, E. K.; Qin, L.; Mirkin, C., A., *Angew. Chem., Int. Ed.* **2006**, *45* (17), 2672-2692.
20. Park, S.; Lim, J.-H.; Chung, S.-W.; Mirkin, C. A., *Science* **2004**, *303* (5656), 348-351.
21. Pearce, M. E.; Melanko, J. B.; Salem, A. K., *Pharm. Res.* **2007**, *24* (12), 2335-2352.
22. Martin, B., R.; Dermody, D., J.; Reiss, B., D.; Fang, M.; Lyon, L. A.; Natan, M., J. ; Mallouk, T. E., *Adv. Mater.* **1999**, *11* (12), 1021-1025.
23. Banholzer, M. J.; Qin, L.; Millstone, J. E.; Osberg, K. D.; Mirkin, C. A., *Nat. Protoc.* **2009**, *4* (6), 838-848.
24. Wei, W.; Li, S.; Millstone, J., E.; Banholzer, M. J.; Chen, X.; Xu, X.; Schatz, G., C.; Mirkin, C., A., *Angew. Chem., Int. Ed.* **2009**, *48* (23), 4210-4212.
25. Zhihong Nie, Shengqing Xu,, Minseok Seo,, Patrick C. Lewis, and, Eugenia Kumacheva, *Journal of the American Chemical Society* **2005**, *127* (22), 8058-8063.
26. Shepherd, R. F.; Conrad, J. C.; Rhodes, S. K.; Link, D. R.; Marquez, M.; Weitz, D. A.; Lewis, J. A., *Langmuir* **2006**, *22* (21), 8618-22.
27. Dendukuri, D.; Pregibon, D. C.; Collins, J.; Hatton, T. A.; Doyle, P. S., *Nature materials* **2006**, *5* (5), 365-9.
28. Dendukuri, D.; Gu, S. S.; Pregibon, D. C.; Hatton, T. A.; Doyle, P. S., *Lab on a chip* **2007**, *7* (7), 818-28.
29. Christian Decker, A. D. J., *Macromolecules* **1985**, *18* (6), 1241-1244.
30. Dendukuri, D.; Hatton, T. A.; Doyle, P. S., *Langmuir* **2007**, *23* (8), 4669-74.
31. Panda, P.; Yuet, K. P.; Hatton, T. A.; Doyle, P. S., *Langmuir* **2009**, *25* (10), 5986-92.
32. Christopher, G. F., Anna, S. L., *J. Phys. D: Appl. Phys.* **2007**, *40*, R319-R336.
33. Nisisako, T.; Torii, T.; Takahashi, T.; Takizawa, Y., *Advanced Materials* **2006**, *18* (9), 1152-1156.
34. Ho, C. C., Keller, A., Odell, J. A., and Ottewill, R.H. , *Colloid Polym Sci* **1993**, *271*, 469-479.

35. Champion, J. A.; Katare, Y. K.; Mitragotri, S., *Proceedings of the National Academy of Sciences of the United States of America* **2007**, *104* (29), 11901-4.
36. Geissler, M.; Xia, Y., *Advanced Materials* **2004**, *16* (15), 1249-1269.
37. Sreenivasan, S. V., *MRS Bulletin* **2008**, *33*, 854-863.
38. Badaire, S.; Cottin-Bizonne, C.; Woody, J. W.; Yang, A.; Stroock, A. D., *Journal of the American Chemical Society* **2006**, *129* (1), 40-41.
39. Hernandez, C. J.; Mason, T. G., *The Journal of Physical Chemistry C* **2007**, *111* (12), 4477-4480.
40. Jang, J.-H.; Ullal, C. K.; Kooi, S. E.; Koh; Thomas, E. L., *Nano Letters* **2007**, *7* (3), 647-651.
41. Moon, J. H.; Kim, A. J.; Crocker, J. C.; Yang, S., *Advanced Materials* **2007**, *19* (18), 2508-2512.
42. Badaire, S.; Cottin-Bizonne, C.; Woody, J. W.; Yang, A.; Stroock, A. D., *Journal of the American Chemical Society* **2007**, *129* (1), 40-41.
43. Badaire, S.; Cottin-Bizonne, C.; Stroock, A. D., *Langmuir* **2008**, *24* (20), 11451-11463.
44. Hernandez, C. J.; Kun, Z.; Mason, T. G., *Soft Materials* **2007**, *5* (1), 1-11.
45. Hernandez, C. J.; Kun, Z.; Mason, T. G., *Soft Materials* **2007**, *5* (1), 13-31.
46. Xia, Y.; Whitesides, G. M., *Angew. Chem. Int. Ed.* **1998**, *34* (5), 550-575.
47. Dumond, J. L. H. Y., *Advanced Materials* **2008**, *20* (7), 1291-1297.
48. Glangchai, L. C.; Caldorera-Moore, M.; Shi, L.; Roy, K., *J Control Release* **2008**, *125* (3), 263-72.
49. Johnson, S. C.; Bailey, T. C.; Dickey, M. D.; Kim, E. K.; Smith, B. J.; Stacey, N. A.; Ekerdt, J. G.; Wilson, C. G.; Jamieson, A. T.; Resnick, D. J.; Mancini, D. P.; Dauksher, W. J.; Nordquist, K. J., *Proc. SPIE* **2003**, 5037.
50. Guan, J.; Ferrell, N.; James Lee, L.; Hansford, D. J., *Biomaterials* **2006**, *27* (21), 4034-41.
51. Oudshoorn, M. H.; Penterman, R.; Rissmann, R.; Bouwstra, J. A.; Broer, D. J.; Hennink, W. E., *Langmuir* **2007**, *23* (23), 11819-25.

52. Moran, I. W. C.; Dalton F.; Jhaveri, Sarav B.; and Carter, Kenneth R. , *Soft Matter* **2008**, 4, 168-176.
53. Rolland, J. P.; Maynor, B. W.; Euliss, L. E.; Exner, A. E.; Denison, G. M.; DeSimone, J. M., *Journal of the American Chemical Society* **2005**, 127 (28), 10096-100.
54. Rolland, J. P.; Van Dam, R. M.; Schorzman, D. A.; Quake, S. R.; Desimone, J. M., Solvent-resistant photocurable "liquid teflon" for microfluidic device fabrication. In *Journal of the American Chemical Society*, 2004; Vol. 126, pp 2322-2323.
55. Maynor, B. W.; Larue, I.; Hu, Z.; Rolland, J. P.; Pandya, A.; Fu, Q.; Liu, J.; Spontak, R.; Sheiko, S.; Samulski, R.; Samulski, E.; Desimone, J. M., *Small (Weinheim an der Bergstrasse, Germany)* **2007**, 3 (5), 845-849.
56. Xia, Y.; Rogers, J. A.; Paul, K. E.; Whitesides, G. M., *Chemical reviews* **1999**, 99 (7), 1823-1848.
57. Euliss, L. E.; Dupont, J.; Gratton, S. E.; Desimone, J. M., *Chem. Soc. Rev.* **2006**, 35 (11), 1095.
58. Gratton, S. E.; Napier, M. E.; Ropp, P. A.; Tian, S.; Desimone, J. M., *Pharmaceutical research* **2008**, 25 (12), 2845-52.
59. Gratton, S. E.; Pohlhaus, P. D.; Lee, J.; Guo, J.; Cho, M.; Desimone, J. M., *Journal of Controlled Release* **2007**, 121 (1-2), 10-18.
60. Gratton, S. E.; Williams, S. S.; Napier, M. E.; Pohlhaus, P. D.; Zhou, Z.; Wiles, K. B.; Maynor, B. W.; Shen, C.; Olafsen, T.; Samulski, E. T.; Desimone, J. M., *Accounts of chemical research* **2008**, 41 (12), 1685-95.
61. Herlihy, K. P.; Nunes, J.; Desimone, J. M., *Langmuir : the ACS journal of surfaces and colloids* **2008**, 24 (16), 8421-6.
62. Kelly, J. Y.; Desimone, J. M., *Journal of the American Chemical Society* **2008**, 130 (16), 5438-9.
63. Petros, R. A.; Ropp, P. A.; Desimone, J. M., *Journal of the American Chemical Society* **2008**, 130 (15), 5008-9.
64. Rolland, J. P.; Maynor, B. W.; Euliss, L. E.; Exner, A. E., *Curr. Opin. Colloid Interface Sci* **2004**.
65. Orgel, R.; Merkel, T. J.; Desimone, J. M., Unpublished work. 2008.

66. Zhang, H. N., J. K.; Gratton, S. E. A.; Herlihy, K. P.; Pohlhaus, P. D.; DeSimone, *New Journal of Physics* **2009**, *11*, 075018.
67. Park, H. J. K., Myuung-Gyu; Guo, L. Jay, *ACS Nano* **2009**, *XXX* (XXX), XXXX.
68. Smithson, R.; McClure, D.; Fennell Evans, D., *Thin Solid Films* **1997**, *307* (1-2), 110-112.
69. Gratton, S. E.; Ropp, P. A.; Pohlhaus, P. D.; Luft, J. C.; Madden, V. J.; Napier, M. E.; Desimone, J. M., *Proc Natl Acad Sci USA* **2008**, *105* (33), 11613-8.
70. Hou, S.; Wang, J.; Martin, C. R., *Nano Lett.* **2005**, *5* (2), 231-234.
71. Glotzer, S. C.; Solomon, M., *Nature materials* **2007**, *6* (7), 557-562.
72. Sundararajan, S.; Lammert, P. E.; Zudans, A. W.; Crespi, V. H.; Sen, A., *Nano letters* **2008**, *8* (5), 1271-6.
73. Teranishi, T., *Small (Weinheim an der Bergstrasse, Germany)* **2006**, *2* (5), 596-8.

## **Section 2: Shape and Size Specific Contrast Agent Fabrication, Characterization and Early Biodistribution Studies**

### **2.1 Introduction to Nanomedicine and Nanodiagnostics**

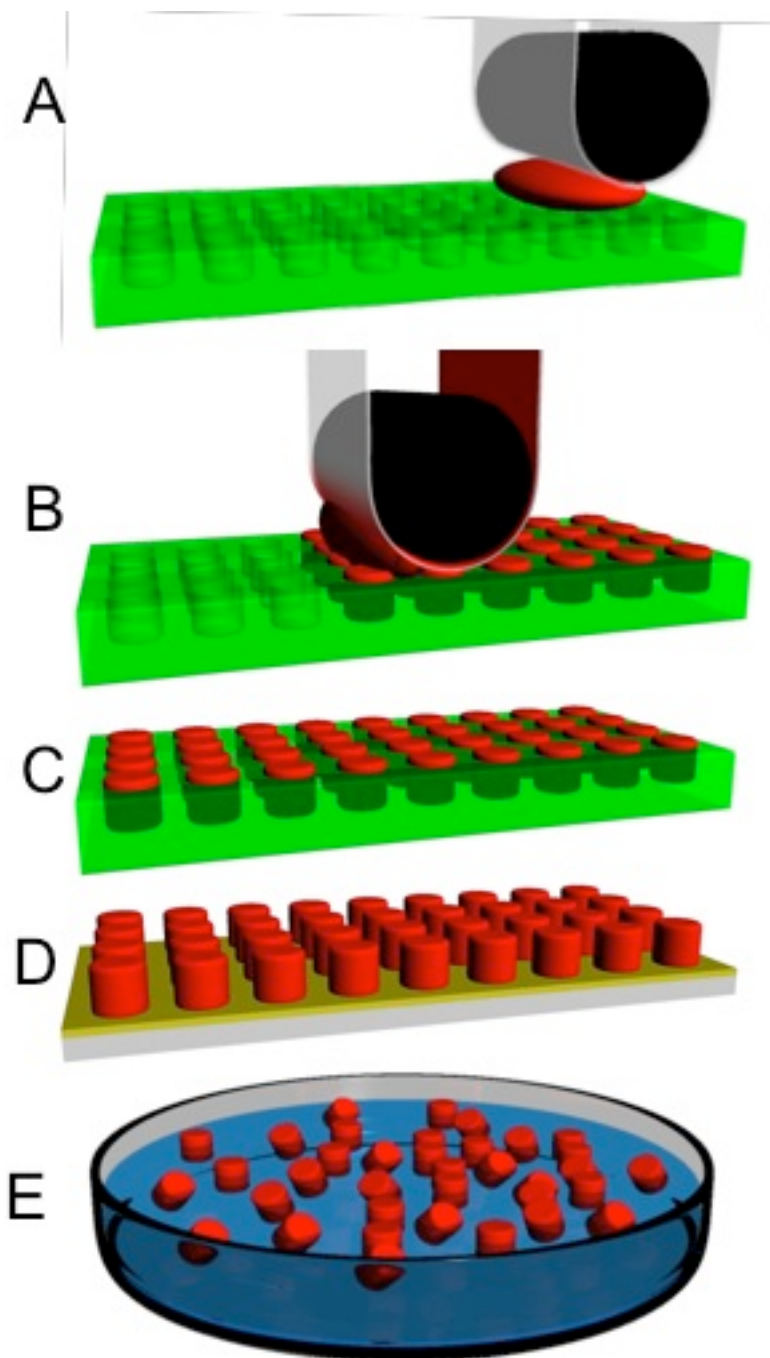
As new nanopharmaceuticals and nanocontrast agents are being developed, researchers are focusing on minimizing side effects and improving specific biodistribution found in their traditional small molecule counterparts. Overcoming barriers for effective bioavailability of small molecule therapeutic agents has been especially challenging in the fields of gene therapy<sup>1</sup> and oncology.<sup>2</sup> As an illustration, despite their potential for wide application, only a few antisense oligonucleotides or small interfering RNA's (siRNA) have entered the clinic. The prevalence of hydrophobic drugs constitutes the need for nanocarriers; for these systems, direct dissolution in the bloodstream is limited without the formation of a salt or use of a delivery vector.<sup>3</sup> One solution to this problem is the delivery of drugs, gene therapy agents, and imaging contrast agents via nano-scale vectors, and this has been an area of intense study for decades. Although multiple approaches have been explored and great strides have been made in therapeutic drug delivery and diagnostic imaging agent carriers, a set of rules for the rational design of nanocarriers has not yet been fully established. This is due in part to limited understanding of how their size, shape, matrix functionality, porosity, flexibility, and surface chemistry interact. Clearly, a strong motivation for the development of nanocarriers exists in cases in which the drug or imaging agent is too fragile, insoluble, or toxic for direct in vivo administration.

Potential delivery solutions including liposomal pharmaceutical carriers<sup>4</sup>, polyplexes,<sup>5, 6</sup> and polymer-drug conjugates,<sup>7, 8</sup> have shown promise on several fronts for decades. Indeed, the breadth and volume of therapeutic and imaging nanoparticle literature is considerable. However, the development of shape and size specific therapeutics and imaging agents has only now begun to gain traction. Research groups focusing on the effect of shape and size of nanocarriers are beginning to make significant progress towards shape driven biodistribution.<sup>9, 10</sup> In this subsection, the latest advances in shape and size specific nanotherapeutics are briefly reviewed setting the stage for shape specific multimodal contrast agents. The fabrication, characterization and initial biodistribution studies of multimodal shape and size specific PRINT particles are described in detail in the following subsections.

## **2.2 Background on Nanotherapeutics**

Several critical factors that must be considered in the design of contrast agent and/or polymeric drug carriers include the chemical functionality and mechanical flexibility of the matrix, the degree of cross-linking, if any, the dispersion or encapsulation of the drug within the matrix, the permeability of the cargo through the matrix of the particle, the number and the nature of phases that comprise the particle (one phase versus two or more phases e. g. drug rich phase and matrix rich phase), the size and shape of the particle, and the surface chemistry. Many of these factors have been varied extensively as imaging contrast agents and therapeutic cargos ranging from small molecules to proteins and nucleotides have all been encapsulated. A large body of *in vivo* studies has proven that particle size is a crucial factor in biodistribution, treatment of inflammation, and tumor bed penetration. The effect of particle shape, on the other hand, has received much less attention and is not well understood.

Using advances at the interface between biology and the traditionally materials science-based field of soft lithography,<sup>11</sup> researchers have only recently been able to access interesting shapes at the sub-micron size range on a sufficient volume scale to allow for extensive *in vitro* and *in vivo* biological studies. In this technique, a biological pattern or the pattern on a hard substrate master, typically a silicon wafer, is embossed onto to a more flexible, crosslinked polymer material, the mold. Soft lithography has been used extensively to mold naturally occurring objects and prepare patterns for microfluidics, and these topics have been the subject of recent reviews.<sup>12</sup> A modification of these traditional lithographic methods, known as Particle Replication In Non-wetting Templates (PRINT®) (Figure 2.1),<sup>13-21</sup> has proven to be valuable for producing precisely-controlled polymeric vectors in the tens of nanometers to micron size range. The PRINT process constitutes a tunable particle preparation platform by allowing entrapment (transiently, if desired) of diagnostic imaging agents and a wide variety of therapeutic cargo types while simultaneously providing tremendous latitude in the chemical composition of the carrier matrix. In addition, the PRINT process is well suited for independent and precise variation shape, size, and modulus (stiffness) of the particle. Indeed, PRINT affords unprecedented control and flexibility in the engineering of rationally designed particles, and thus it offers advantages as a fabrication method when compared to techniques employed to prepare traditional carriers such as liposomes, dendrimers, and colloidal particles.



**Figure 2.1** Schematic representation of the PRINT process. First an empty mold (green), a high surface energy polymer sheet (clear), and a roller (black) is brought into contact with the particle precursor solution and the mold (A); second, a roller evenly distributes particle precursor solution into the cavities of mold (B). Third, excess particle precursor solution is wicked away by the high surface energy polymer sheet; Fourth, individual particles are cured in the mold (C); Fifth, particles are removed from the mold using a sacrificial adhesive layer (D); And sixth, particles are collected or harvested using a number of different film based techniques and ultimately are dispersed in solution (E).



Until recently, the general conclusions drawn about particle size effects on various biological processes relied on studies using primarily spherical particles. This is due to the fact that drug or contrast agent-loaded spherical particles with a narrow size distribution can be fabricated in a straight forward manner by a number of methods including emulsion, dispersion, and suspension polymerizations as well as precipitation and spraying techniques. The roles that particle size and composition play in biodistribution,<sup>22</sup> cellular binding,<sup>23</sup> cell entry pathways,<sup>24</sup> cell uptake,<sup>25-27</sup> and tumor bed penetration<sup>28, 29</sup> have been studied extensively for macromolecular carriers and spherical particles.

This work with spherical particles has resulted in valuable insights, but many naturally occurring objects are non-spherical, and biological processes typically occur under dynamic conditions in which the motion of spherical and non-spherical objects will differ. Indeed, Decuzzi and Ferrari's theoretical work predicts that, under conditions of linear shear flow such as that in the bloodstream, oblate particles adhere more strongly to biological substrate than spherical particles; use of non-spherical particles for delivery is predicted to improve therapeutic and imaging efficacy.<sup>30</sup> Experimentally, the combined effects of particle size, shape, charge, and chemical composition on biodistribution and cell entry have not yet been fully studied,<sup>28</sup> but data suggest that seemingly small changes in chemical composition and modulus of the particle materials can have profound effects *in vivo*. Clearly the major roadblock to examining the interdependence of particle size, shape, surface chemistry, and modulus is the previous lack of a suitable particle fabrication technique.

Recently, techniques have been developed to prepare non-spherical particles by molding techniques such as the PRINT process, post-fabrication manipulation of spherical particles, or directly through microfluidics. Although particle size impact on bioavailability

has been the subject of numerous studies, particle shape, on the other hand, has received less attention. It is clear that particle shape is crucial to the mechanism of cellular entry<sup>17, 29, 31, 32</sup> and the release rate of the therapeutic cargo.<sup>33, 34</sup> Shape effects on biological processes, however, are still not fully understood, particularly at the nanoscale, primarily due to past limitations in the control of particle fabrication. Experimental explorations into the idea that unpredicted biological effects could result from non-spherical particle shapes are described in this section.

A preliminary study of the biodistribution and pharmacokinetic study of <sup>125</sup>I-labeled non-targeted, cylindrical particles prepared by the PRINT process in the 200 nm size range in healthy mice showed the expected uptake primarily in the liver and spleen.<sup>16, 18</sup> The conventional strategies to reduce the rapid clearance from the bloodstream and uptake by the liver and spleen have been to increase hydrophilicity of the particle surface and reduce particle size. In an alternative approach, however, Discher and coworkers have compared soft spherical assemblies to flexible filaments (worm-like particles) and found that the *in vivo* circulation time for the non-spherical filomicelles was about ten times longer than their analogous spherical counterparts.<sup>35</sup> They extended their study to the delivery of paclitaxel and showed significant tumor shrinkage in a xenograft mouse tumor model, and showed that an increase in the filomicelle length had the same relative therapeutic effect as a similar increase in the paclitaxel dosage. These results show that, in applications where a prolonged circulation time is desired, a long, worm-like structure can be more effective than a sphere.

Besides the effect that particle shape can play on biodistribution parameters, particle size and shape also play a key role in the mechanism of passage through the cell membrane into the cell. The biological details of cell internalization of macromolecules and particles

have been reviewed.<sup>36</sup> Gratton et al. completed experiments showing size and shape effects on the uptake of highly crosslinked acrylic particles fabricated via the PRINT process by HeLa cells.<sup>17</sup> In this work, a large library of crosslinked, poly(ethylene glycol) (PEG)-based particles of various sizes and shapes were prepared via the PRINT process with sizes ranging from 100 nm up to 5  $\mu$ m and aspect ratios from 1 to 3. Non-targeting particles fabricated from this formulation showed excellent uptake by HeLa cells, and cellular uptake mechanisms have been elucidated. Interestingly, this work showed that it is not the particles of lowest volume that enter cells at the fastest rate. Instead, rod like particles similar in shape and size to many bacteria showed kinetically preferential uptake.

The emerging understanding of the importance of particle shape in macrophage phagocytosis has been described and carefully studied by Champion.<sup>29, 37</sup> Recognition of the fact that naturally occurring immunological targets vary widely in both size and shape provided motivation for this work. By carefully varying shape at constant size, the authors concluded that it is indeed particle shape, rather than size, which plays a dominant role for determining the complexity of the local actin structure, and ultimately whether phagocytosis or simply spreading processes occur.

Studies have also shed light on the roles played by size and shape of particulate carriers in the complicated biological processes of biodistribution, cell uptake, and bioavailability. The ability to prepare particles in a manner that allows independent alteration of one variable at a time has proven fruitful for gaining insights into shape-dependent biological processes such as phagocytosis. Many techniques, such as stretching thermoplastic particles<sup>37</sup> or S-FIL preparation of crosslinked particles as described above,<sup>38</sup> can be employed to prepare small amounts of shape-specific particles. Practical, large-scale

manufacturing techniques for fabrication of non-spherical, shape-specific particles, however, is perhaps the biggest advantage gained by the application of the PRINT process to this area.

### **2.3 Background on Nanoparticle Imaging Agents**

While size and shape clearly play an important role in nanoparticle drug delivery, the field of medical imaging has seen very few applications or systematic studies exploring the effect of variation in particle size and shape. Therefore, the potential for important discoveries in the field of size and shape dependence on nanoparticle biodistribution and targeting is enormous. Without a doubt, studies directed toward successful targeted delivery of size and shape-specific nanoparticles as novel therapeutic agents will be contingent on the successful visualization of their whereabouts *in vivo*. Moreover, nanoparticle-mediated delivery of contrast agents provides an opportunity to reduce the toxicity effects associated with commonly employed contrast enhancement agents by improving specific biodistribution and reducing the required dosage.

A number of different imaging modalities can be drawn upon for successful imaging of tissue through nanoparticle mediated delivery. Such modalities include, but are not limited to, magnetic resonance (MR) imaging, positron emission tomography (PET), single photon emission computed tomography (SPECT), ultrasound imaging, and near infrared fluorescent (NIRf) imaging. Here we focus on recent advances for imaging agent carriers in MR, PET, and NIRf imaging.

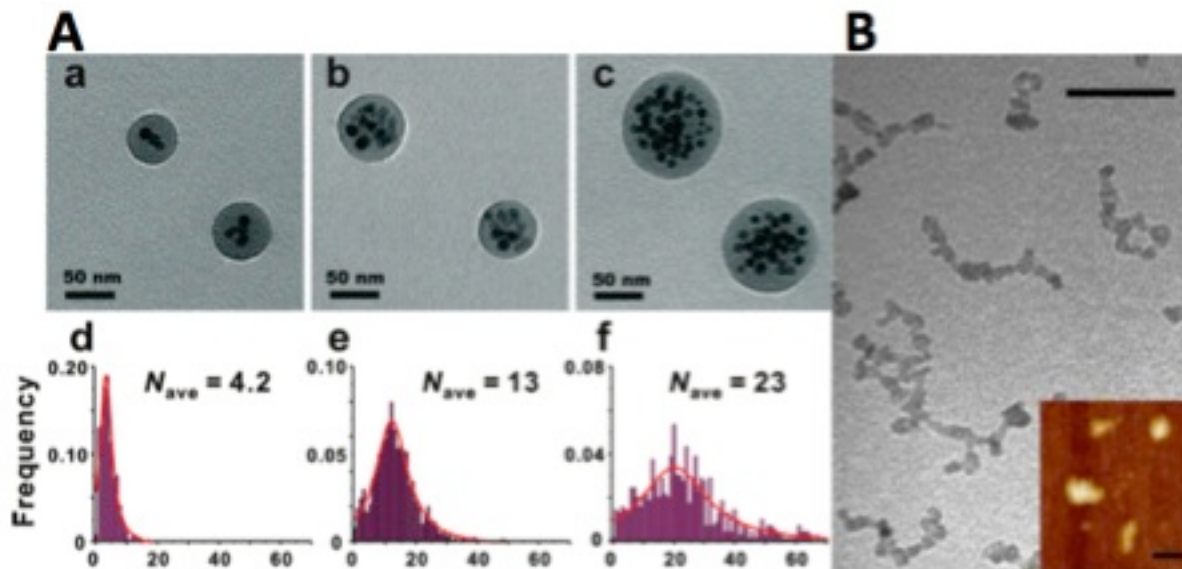
#### **2.3.1 MR Imaging**

Magnetic Resonance (MR) imaging plays an ever increasing role in the development of targeted nanoparticle therapeutics and imaging agents because of its high spatial resolution and unparalleled imaging of soft tissue. Using conventional contrast agents such as iron

oxide nanoparticles and small molecule gadolinium (Gd) chelates, MR imaging is capable of providing excellent spatial resolution and 3D anatomical information. Because of its low sensitivity, however, relatively large concentrations of contrast agent are required to observe a modest increase in contrast. The potential side effects caused by these relatively large contrast agent doses and decreased kidney function have spurred interest in particle-mediated delivery of MR contrast agents which can create contrast with lower doses and which generally avoid the kidney due to size constraints. These contrast agents carry multiple MR beacons per particle and are capable of drastically improving the local contrast. Nanoparticle contrast agents are paving the way for a new generation of imaging in which smaller doses will be required both to monitor the in vivo distribution of nanoparticles and to perform targeted imaging of diseased tissue and tumors. Some of the most recent efforts to exploit polymer-based nanoparticles for delivery of iron oxide, Gd, and other paramagnetic moieties, are summarized below.

In many respects, iron oxide nanocrystals are close to ideal nanoparticle contrast agents. They are nontoxic and are easily surface functionalized with stealthing and targeting agents.<sup>39</sup> Monodisperse samples of iron oxide nanocrystals have been shown to have different R1 and R2 relaxivities based solely on crystal size<sup>40</sup> as well as on the surface coating.<sup>41</sup> Spherical micelles of poly(styrene-*b*-acrylic acid) containing multiple iron oxide nanoparticles were recently reported by Taton and coworkers.<sup>42</sup> The micelles were surface crosslinked into covalently bound assemblies in the 40-140 nm size range using a diamine and functionalized further with a fluorescein derivative. Using this method, larger polymer particles necessarily contained a larger number of iron oxide particles. A different method recently reported by Sailor et al. describes improved relaxivity and improved targeting of

tumor cells over traditional iron oxide nanoparticles using worm-like particles.<sup>10</sup> The worms were composed of iron oxide nanoparticles trapped in strands of dextran.<sup>43</sup> The authors believe that the unique shape of the elongated particles is the key to improving their efficacy. Figure 2.2 demonstrates two examples of different approaches to magnetic nanoparticle fabrication.



**Figure 2.2** TEM images of crosslinked block copolymer (PAA-co-PS) magneto-micelles containing 10 nm iron oxide crystals (A)<sup>42</sup> and linear chains of dextran-coated magnetite (B)<sup>10</sup>.

As stated earlier, iron oxide based imaging agents are popular because of their low level of toxicity and the ease with which one can modify their surface with a variety of ligands, stealthy polymer coatings and fluorescent beacons for multimodal imaging. Because the majority of iron oxide contrast agents create a decrease in signal intensity, causing tissue containing the contrast agent to “go dark,” researchers have pursued other compounds for contrast agents that increase signal intensity.

Small molecule chelates of Gd such as Gd-diethylenetriaminepentaacetic acid (DTPA) and Gd-1,4,7,10-tetraazacyclododecane-1,4,7,10-tetraacetic acid (DOTA) and their derivatives create an increase in MR signal intensity. Caravan has described how the limited sensitivity of MR requires millimolar concentrations of these agents before any contrast is observed.<sup>44</sup> Coupling multiple Gd chelates to a single nanoparticle carrier can increase contrast enhancement per molecule. A number of other synthetic approaches towards gadolinium-bound particles have been described including crosslinked micelles,<sup>45</sup> peptide containing liposomes,<sup>46</sup> dendrimers<sup>47</sup> and hybrid systems.<sup>48</sup>

Very few shape and size specific examples of nanoparticles were found that were capable of creating contrast for MR imaging. One approach involved the encapsulation of MR contrast agent within spherical nanocapsules. Landfester et al. demonstrate the use of inverse miniemulsions to encapsulate commercially available gadolinium-containing contrast agents inside spherical crosslinked dextran nanocapsules.<sup>49</sup> The capsules are porous in nature allowing water exchange across the surface. While the nanocapsules show a small reduction in relaxivity from that of the small molecule encapsulated within, the crosslinked dextran coating provides potential for surface functionalization and altered biodistribution.

Recently our group demonstrated the first example of Gd-containing shape and size specific particles for MR imaging.<sup>50</sup> Two sets of biocompatible hydrogel particles encapsulating a commercially available Gd contrast agent (Omniscan<sup>TM</sup>) were administered to healthy mice. The two particle shapes were: 1.) cylindrical with a diameter of 200 nm and a height of 200 nm, 2.) cuboid particles measuring 2  $\mu$ m on all sides. Particle biodistribution was different depending on the size of the particles. The small particles created an increase in contrast in the liver, kidney and blood vessels while the larger particles were observed

mostly in the liver and blood vessels. Increased contrast was observed up to 3 hours after injection.

### **2.3.2 Positron Emission Tomography**

A number of groups have also adopted a nanoparticle platform for imaging using positron emission tomography (PET). PET imaging uses positron emitting radioisotopes that can easily be bound to the surface, or interior, of a nanoparticle by simple metal chelation chemistry. Positron emitters such as  $^{64}\text{Cu}$  are detectable at concentrations as low as picograms per milliliter. The high sensitivity of PET makes it ideal for quantitative data analysis. Additionally, the ability of positrons to easily penetrate tissue makes PET ideal for deep tissue imaging. Some limitations of PET include low spatial resolution, the inability to provide significant anatomical information, and need for contrast agents that are not widely available.

In 2007, Wooley et al. reported the optimization of radiolabeling crosslinked micellar assemblies poly(styrene)-b-poly(acrylic acid) with  $^{64}\text{Cu}$ -DOTA.<sup>51</sup> In this work, a DOTA-lysine derivative is covalently bound to the acrylic acid units of the copolymer that is subsequently labeled with  $^{64}\text{Cu}$ . The copolymers were then used to form micelles and were surface-crosslinked using 2,2'-(ethylenedioxy)-bis(ethylamine). By varying the relative amounts of DOTA-lysines per chain and the crosslinking ratio they were able to optimize signal enhancement as high as 400  $\mu\text{Ci} / \mu\text{g}$ . Interestingly, the researchers found that the non-crosslinked micelles provided the most intense signal but pointed to the necessity of surface crosslinking for stable nanocontrast agents. Wooley also showed that the particle size plays an important role in circulation times.



More recently, Scheinberg et al. showed the development of positron emitting hydrophilic carbon nanotubes.<sup>52-54</sup> The nanotubes exhibited prolonged blood circulation times and improved tumor accumulation when compared to controls. While carbon nanotubes have a number of interesting attributes for applications in targeted nanoparticle drug delivery, concerns exist about toxicity.<sup>55</sup> Such concerns are leading many researchers to consider other carriers including biocompatible polymer matrices. To the best of our knowledge, no examples of shape specific polymeric particles tagged with radioisotopes currently exist.

### **2.3.3 Near Infrared Fluorescence Imaging**

Interest in NIRf imaging research in small animals has exploded in recent years due largely to low costs, absence of ionizing radiation, and high sensitivity. A gap in the near infrared spectrum found in most tissue makes it possible to image fluorescent tracers tagged to nanoparticles using sensitive NIR cameras. Discher has exploited the use of these to examine the effect of particle shape on circulation times and tumor accumulation.<sup>9</sup> Recently, his group showed that by increasing the particle shape from spherical to long worm-like filomicelles created a marked increase both in blood circulation times and in tumor accumulation.

## **2.4 Multimodal Shape and Size Specific Contrast Agents Fabricated Using the PRINT Process**

As mentioned above, a variety of imaging modalities are currently available for use as nanoparticle conjugated tracers for *in vivo* studies. In addition, MR, PET, and NIRf have all been shown to effectively complement one another for use in small animal imaging studies. While each modality has its own strengths and weaknesses,<sup>56</sup> it would be advantageous to have one particle that utilizes multiple imaging modalities.<sup>57</sup> In this way, one could

capitalize on the strengths and circumvent the weakness of each modality.<sup>58</sup> Conjugation of two or more types of imaging beacons to a shape and size specific nanoparticle would further compound the advantages of multimodal imaging with the ability of shape and size specific particles to plot specific biodistribution maps. This would allow researchers not only to precisely follow the distribution of particles *in vivo*, but also to tailor the distribution properties themselves by changing the shape and size of the particles

In this work, biocompatible shape and size specific particles were fabricated using the PRINT process and used as multimodal contrast agents. Particles were fabricated in four sizes and shapes. First, a series of three particle shapes each with a critical diameter of 80 nm was fabricated. Particles in this series were either 90, 360, or 2000 nm in length. In addition cylindrical particles 200 nm tall with a diameter of 200 nm were also fabricated. The particles were loaded with superparamagnetic iron oxide and a NIR fluorescent dye. After harvesting, particles were post functionalized with bifunctional ligand that was used to chelate <sup>64</sup>Cu. As such, the shape and size specific particles were traceable using three different imaging modalities, PET, MRI, and NIRf.

#### **2.4.1 Particle Composition**

Particles were made up of five major components and were photochemically cured by radical polymerization in order to hold their shape in aqueous suspensions and to prevent the escape of paramagnetic cargo. Particles were primarily composed of a poly(ethylene glycol) (PEG) diacrylate matrix. This matrix was chosen because of excellent hydrophilic and biocompatible characteristics. Next 20 wt % of aminopropyl methacrylamide (APMA) was added to impart primary amine functionality. Aminoethyl methacrylate has been used historically in our lab for this purpose but has recently been shown to undergo numerous side

reactions at elevated pH.<sup>59</sup> These side reactions can eliminate the amine functionality making it impossible to surface functionalize particles through amine chemistry. Iron oxide nanocrystals (10 wt %, 20 nm dextran coated, Chemicell, GmbH) was added to impart paramagnetic behavior. This causes a decrease in T1 (longitudinal) and T2 (transverse) relaxation times and causes a decrease in MR signal intensity (ie. negative contrast). DyLight 680 maleimide (1.5 wt %) was added to facilitate imaging by NIRf. Finally, 1 wt % 1-hydroxycyclohexylphenyl ketone was added as a soluble photo initiator. See table 2.1 for details on particle composition.

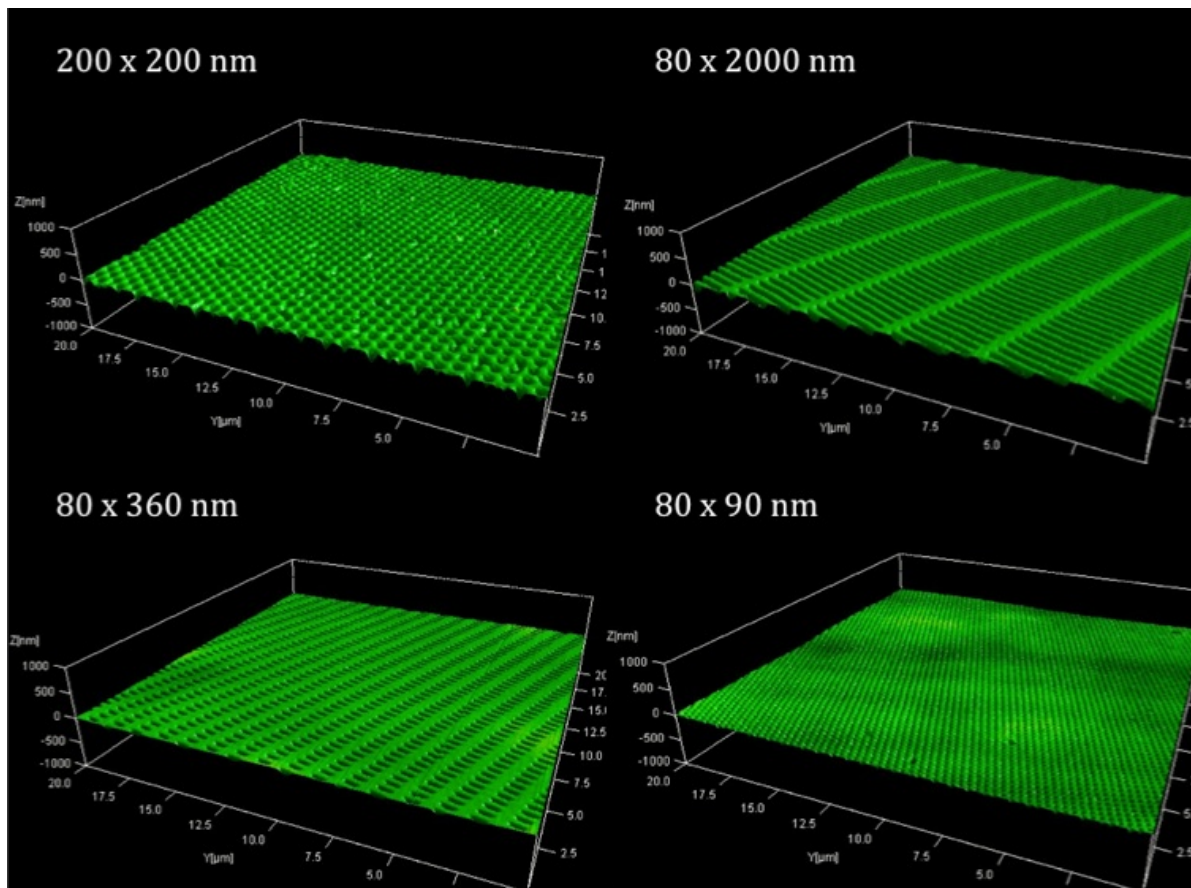
**Table 2.1** Multimodal shape and size specific particle composition.

<b>Particle Composition</b>	
<b>Component</b>	<b>Wt%</b>
PEG <sub>700</sub> -diacrylate	67.5
N-(3-aminopropyl)methacrylamide	20
Dextran-coated iron oxide (20 nm)	10
Dylight 680 maleimide	1.5
1-Hydroxycyclohexyl phenyl ketone	1

#### **2.4.2 Particle Fabrication, Harvesting, and Purification**

The pre-particle solution was diluted with dimethylformamide (DMF) to a concentration between 2.5-4.5 wt %. This solution was drawn over a high surface energy sheet of poly(ethylene terephthalate) (PET) using a Mayer rod (2.54  $\mu$ m, #2 RD Specialties Inc.) and dried briefly to remove excess DMF. Patterned perfluoropolyether (PFPE) molds (Lot # MC1-0175-131) from Liquidia Inc. were used to fabricate particles (Figure 2.3). Using an in-house single nip lamination system, the thin film was laminated to, and peeled away from the patterned PFPE mold in one continuous motion. Capillary forces of the mold

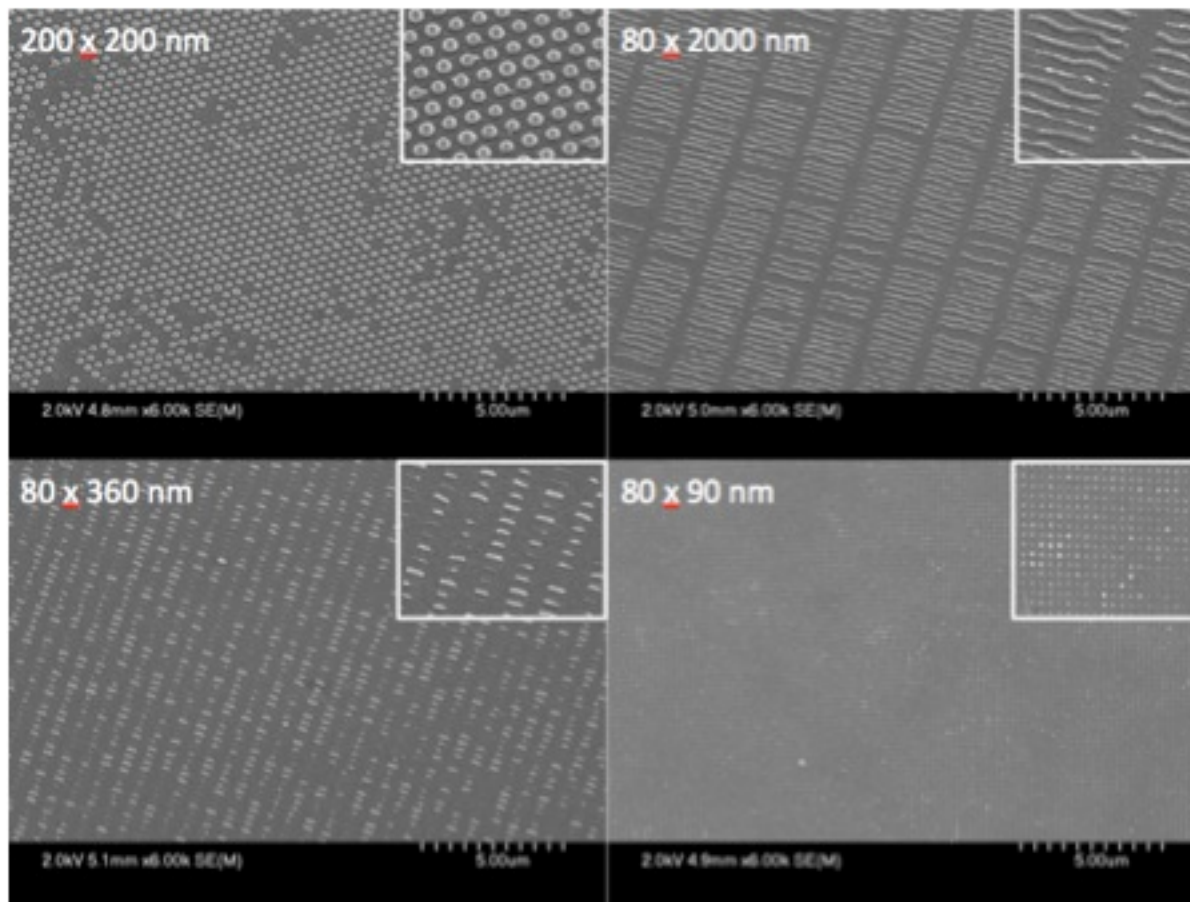
cavities cause the monomer solution to be preferentially trapped within the wells. The low surface energy of the PFPE mold (8-10 dyn/cm)<sup>14</sup> allowed excess monomer solution to be wicked away by the high surface energy PET (42 dyn/cm). The filled PFPE mold was then relaminated to a sheet of PET and cured under UV light (365 nm, 12 J / cm<sup>2</sup>).



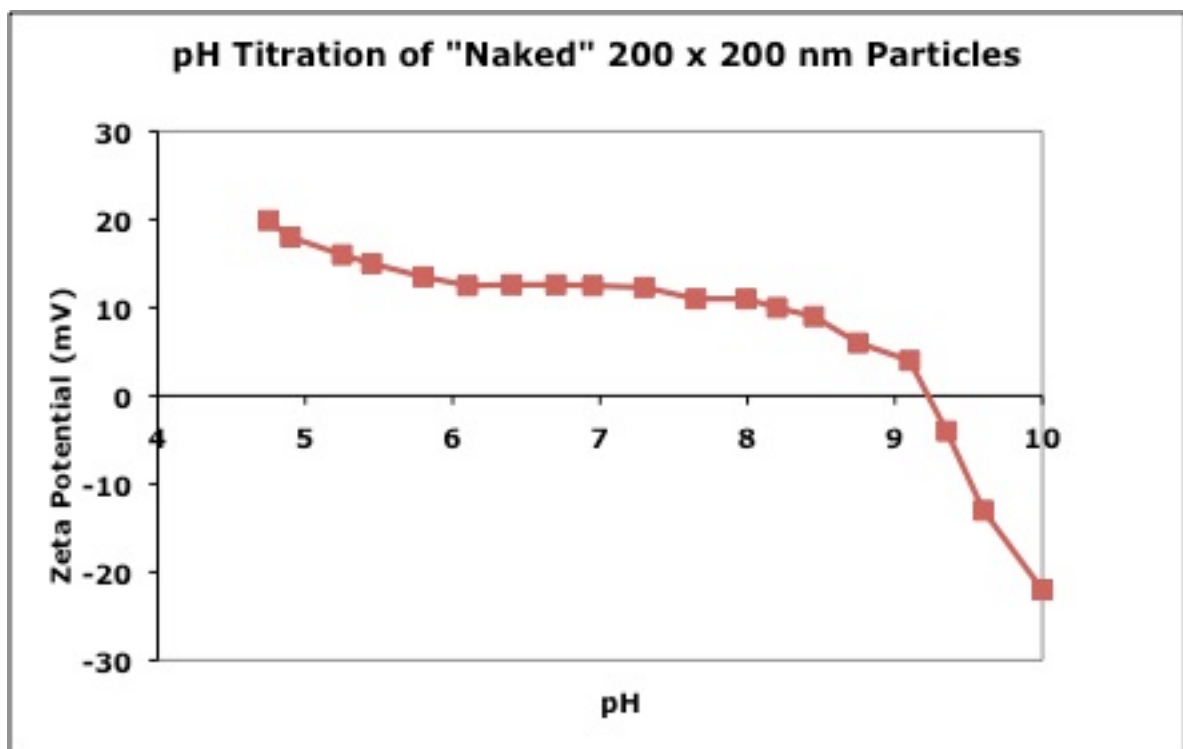
**Figure 2.3** AFM images of empty molds for each of the four particle sizes.

After curing, particles preferentially bound to the PET sheet and the PET sheet was delaminated from the mold (Figure 2.4). Using a drop of filtered d.i. water, particles were gently removed from the PET sheet by agitation with a rubber scraper. The particles were collected and centrifuged in order to remove large debris. Small debris was then removed using a centrifugal filtration device (Ultraclear-MC 100 nm cutoff, PVDF, Millipore Inc.). Because iron oxide formed aggregates in the pre-particle solution, the magnetic character

varies from particle to particle (see TEM image below). As such, particles were then selected for high magnetic loading using a magnetic filtration device (MiniMACS, Miltenyi Biotec, Inc.). The presences of primary amines on the surface of the particle played a large role in its stability as was shown by the change in zeta potential as a function of pH titration (See Figure 2.5).

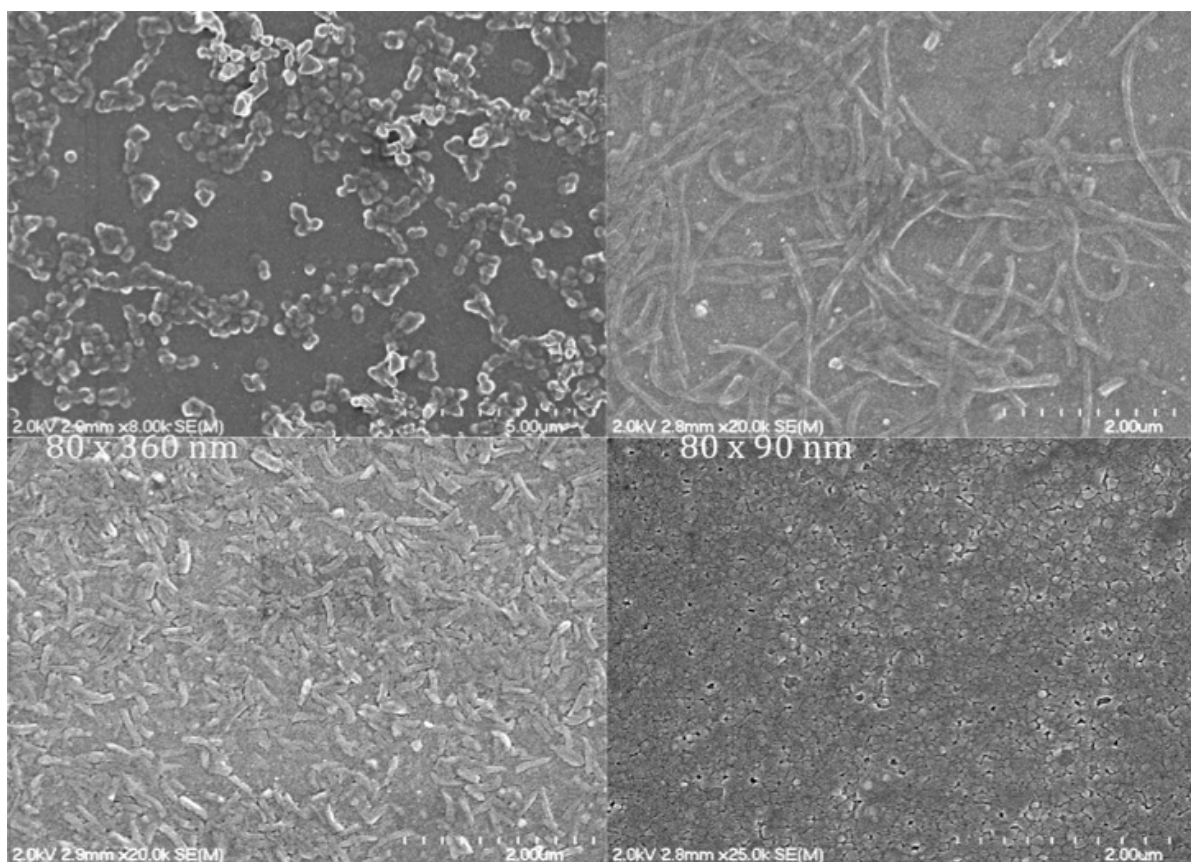


**Figure 2.4** SEM images of particles of each particle size fixed to a PET harvesting layer. Insets show magnified particles from the same harvesting layer.

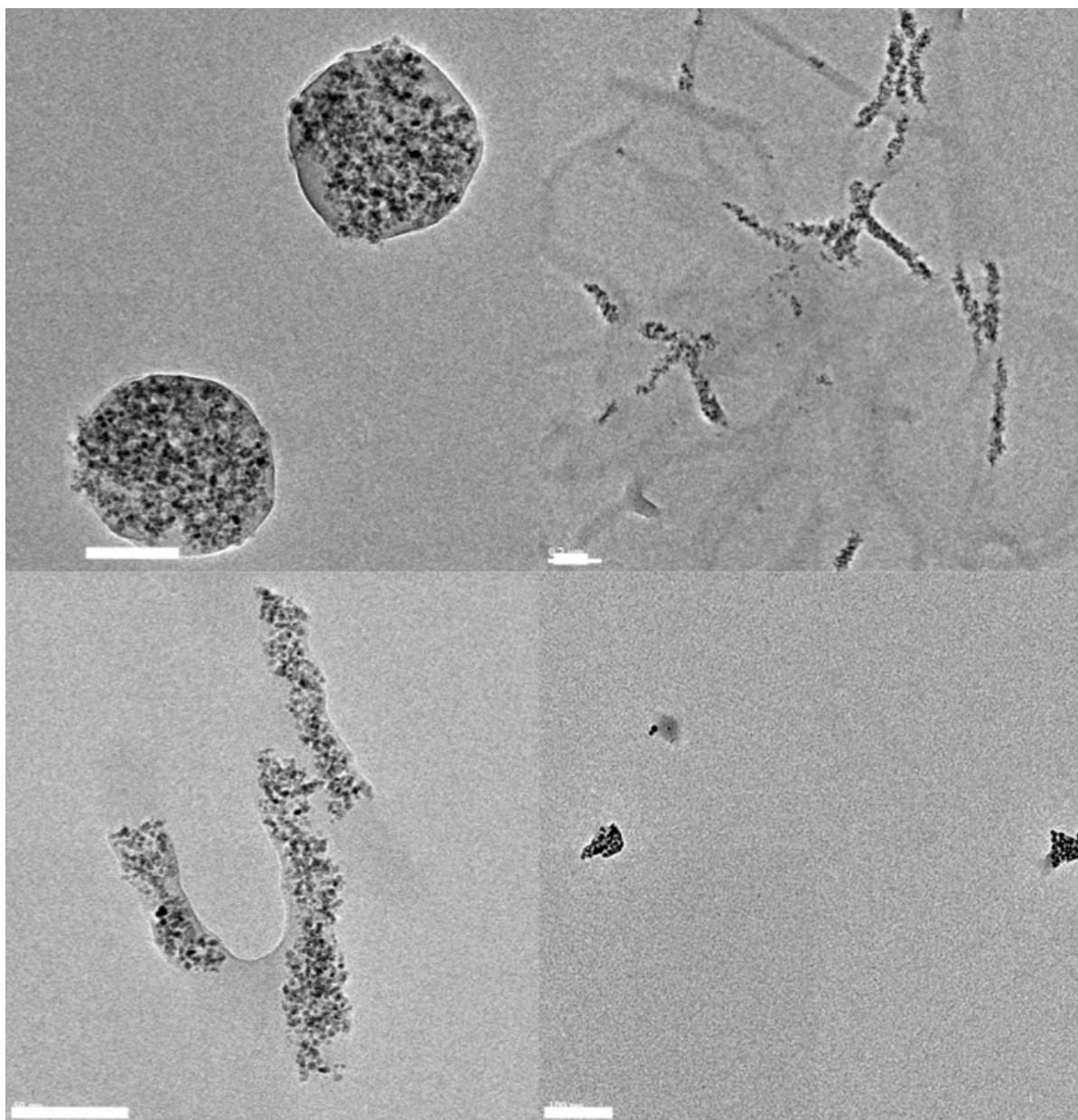


**Figure 2.5** Titration of particle by addition of 25 mM NaOH. Zeta potential is largely positive at physiological pHs.

The particles were then drop cast from solution on a glass slide for imaging by SEM (Figure 2.6). Particles were also imaged by TEM to show iron oxide loading (Figure 2.7). In these images it is evident that the iron oxide is not evenly dispersed throughout the PRINT particle. This is most likely a result of incomplete stabilization of the iron oxide in the pre-particle solution. While stability of the iron oxide nanocrystals can be improved by the addition of surfactants and other stabilizing agent, it was deemed unnecessary for these experiments. A sample of the “naked” particles was saved for characterization purposes.



**Figure 2.6** SEM images of free particles of each particle size drop cast from aqueous solution.



**Figure 2.7** TEM images of all particle sizes containing iron oxide nanoparticles. Scale bar is 100 nm for each image.

### **2.4.3 Particle Surface Functionalization**

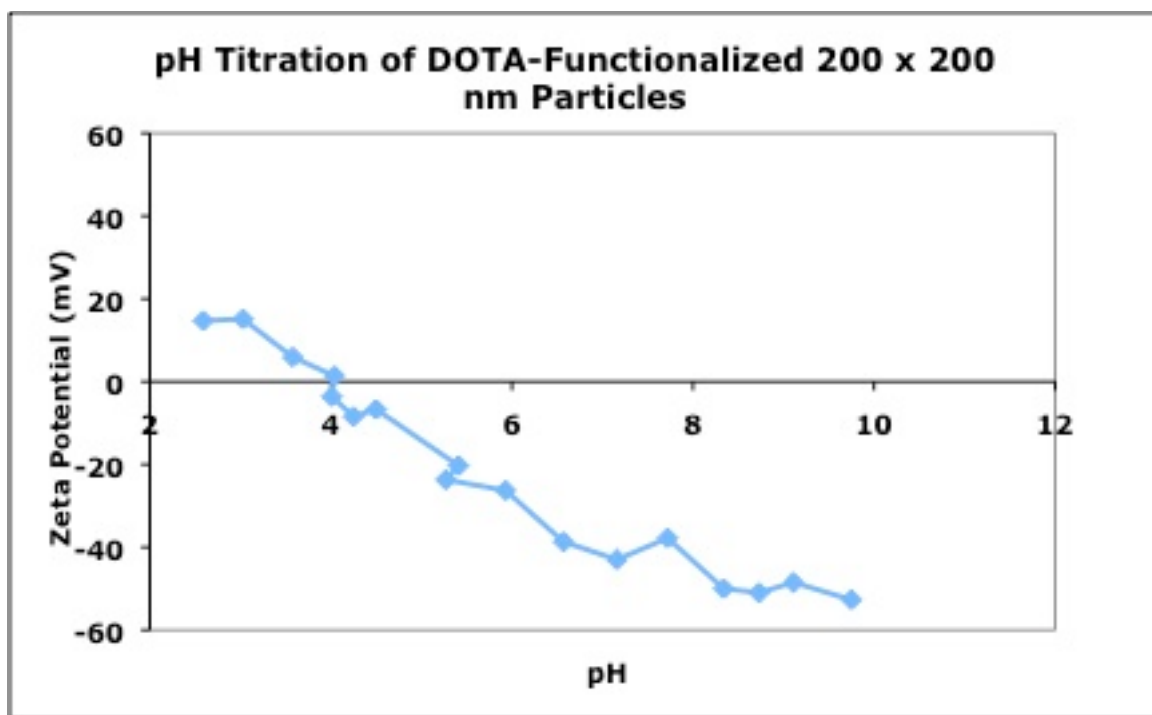
#### **2.4.3.1 Surface Functionalization with DOTA-bz-SCN**

After purification and redispersed in metal free water, 10 mM DTPA (pH 8) was added to chelate any free metal from solution. Particles were vortexed in DTPA overnight then centrifuged out of solution. From this point on in the particle surface functionalization,



all aqueous solvents and buffers were purified using a Chelex® 100 resin to remove trace amounts of metal that could competitively bind to the DOTA ligand and prevent  $^{64}\text{Cu}$  binding. In addition, all glassware was substituted with plastic containers. Metal spatulas were substituted with poly(tetrafluoroethylene) (PTFE) coated spatulas. And pipet tips were purchased from BioRad which was determined by the Scheinberg lab to have the lowest levels of residual metal contaminants.

Residual DTPA was allowed to remain in the particle dispersion to prevent contamination by iron that might leach from the magnetite trapped within the particles. Next, the pH was adjusted to 8.5 using a sodium bicarbonate buffer solution (0.5 M). In a separate vial, a bifunctional macrocyclic ligand (DOTA-bz-SCN, Macrocyclics Inc.) was dissolved in metal free water (10 mg / mL). The DOTA solution was then added to the particle dispersion (0.5 : 1.0, DOTA :  $-\text{NH}_2$ ), briefly sonicated, and then vortexed at room temperature for 1 hour. A sample of the DOTA-functionalized particles was saved for further characterization. A drop in zeta potential at all pHs is observed due to the presence of carboxylic acid groups in the place of primary amines (see Figure 2.8).



**Figure 2.8** Zeta potential of DOTA-functionalized 200 x 200 nm cylindrical particles as a function of the pH.

#### 2.4.3.2 Surface Functionalization with PEG-NHS

Methoxy-poly(ethylene glycol) N-hydroxy succinate (mPEG-NHS) with a molecular weight of 5000 g / mol was then added to the dispersion at a ratio of 1 : 1 mPEG-NHS : -NH<sub>2</sub>. The PEG was allowed to react with the particles for 2 hours under constant vortexing. After the initial PEG conjugation, a second addition of 1 : 1 mPEG-NHS : -NH<sub>2</sub> was added which was allowed to react for an additional 12 hours. Samples of particles were taken after each addition of PEG for further characterization. With each addition of PEG the zeta potential was brought closer to zero (see Table 2.2). As the zeta potential approaches zero, the particle hydrodynamic radius increases. This is a result of the loss of electrostatic stability as primary amines are converted to neutral PEG chains. Finally, the particles were pelleted out of solution by centrifugation (14,000 rpm / 20,000 G) and resuspended in metal

free water. This process was repeated two times to remove excess buffer and unreacted DOTA-bz-SCN and mPEG-NHS reagents.

**Table 2.2** Zeta potential of 200 x 200 nm cylindrical particles as a function of pH and number of PEGylations.

	“Naked” Particles	1 <sup>st</sup> PEGylation	2 <sup>nd</sup> PEGylation
pH 4	DLS = 309	DLS = 339	DLS = 533
	Zeta = 39.8	Zeta = 31.1	Zeta = 17.5
pH 6		DLS = 224	DLS = 351
		Zeta = -18.7	Zeta = -5.64

#### 2.4.3.3 “Cold” Copper Chelation

Copper chloride in HCl was buffered to pH 4.5 with 3 M sodium acetate (NaOAc). Particles were then dispersed in 3 M NaOAc at pH 4.5. An aliquot of copper solution was added to the particles in a screw-top eppendorf tube (used to prevent radioactive contamination with the gloves). The particles were briefly sonicated and vortexed, then placed in a dry well incubator at 55-60 °C. After 45 minutes, the particles were cooled to room temperature and a 10 µL aliquot of 10 mM DTPA was added to the dispersion to chelate any free copper. The dispersion was mixed briefly and allowed to sit for an additional 10 minutes. Finally, the particles were spun out of solution at 14,000 rpm. If the particles were going to be used for characterization, they were redispersed in metal free water.

Particles that were used for *in vivo* imaging were redispersed in a solution of 5 wt % dextrose in 0.9 % saline. This solution was diluted to 1µg / mL with d.i. water and the zeta

potential and hydrodynamic radius of the particles was determined at pH 5 and 7 to be +27 mV and -3.6 mV respectively. The particles were shown to have an isoelectric point between these two pH ranges. This is important to note because of the dramatic affect that particle zeta potential can have on biodistribution. Particles with large positive zeta potentials are known to be rapidly taken up by the macrophages of the Reticulo Endothelial System (RES).<sup>60</sup>

#### **2.4.3.4 <sup>64</sup>Cu Chelation**

Chelation of <sup>64</sup>Cu by surface functionalized PRINT particles was performed using the same chemical procedure as with “cold” copper. Extra precautions, however, were taken to limit exposure to ionizing radiation created by <sup>64</sup>Cu decay. All wet chemistry was performed behind a 2” thick lead shield. An upright plexiglass shield was used to eliminate the chance of splash back. All of the standard personal protective equipment (PPE) was used including gloves, safety goggles, and a lab coat. In addition, waterproof sleeves were worn along with a radioisotope counting badge and ring that was worn on my dominant hand.

In a typical experiment, <sup>64</sup>CuCl<sub>2</sub> from Washington University was diluted to 200 µL with 3 M HCl in order to make it easier to handle. An aliquot of this solution was diluted with metal free 3 M NaOAc. For a set of 3 animals, 3 mCi of <sup>64</sup>Cu solution was added to 1 mg of particles in 100 µL 3 M NaOAc and the pH was adjusted to between 4.5 and 5. After sonicating and mixing, the particles were incubated at 55-60 °C. After 45 minutes the particles were cooled to room temperature and 10 µL of 10 mM DTPA was added to chelate any free <sup>64</sup>Cu. After a 10 minute DTPA challenge the particles were pelleted out and redispersed in a solution of 5 wt % dextrose in 0.9 % saline to a concentration of 1 mg particles / mL. Activity of the injected doses was typically 2-4 Ci / L although activity as

high as 8 Ci / L has been observed. Higher activity is certainly achievable but was not desired because of the required dosage.

## **2.5 Particle Characterization**

### **2.5.1 Particle Concentration and Iron Oxide Content Determination by Thermogravimetric Analysis**

Purified particles were dispersed in metal free d.i. water. A 25  $\mu$ L aliquot of particles was deposited in a tared aluminum sample pan in the TGA. Samples were brought to 150 °C at a rate of 10 °C / minute and held for 15 minutes in order to remove water from the dispersion and from the particles. After 15 minutes, the sample temperature was raised to 600 °C at a rate of 20 °C / minute and held at 600 °C for 10 minutes to burn off any remaining organic. The particle concentration was calculated as the remainder of the mass after the 150 °C isotherm divided by the initial mass (Equation 2.1). Iron oxide concentration was determined as the mass remaining after the 600 °C isotherm divided by the mass after the 150 °C isotherm (Equation 2.2).

$$\textit{ParticleConcentration} = \frac{\textit{dryparticlemass}}{\textit{totalsamplemass}} \quad (\text{Eqn 2.1})$$

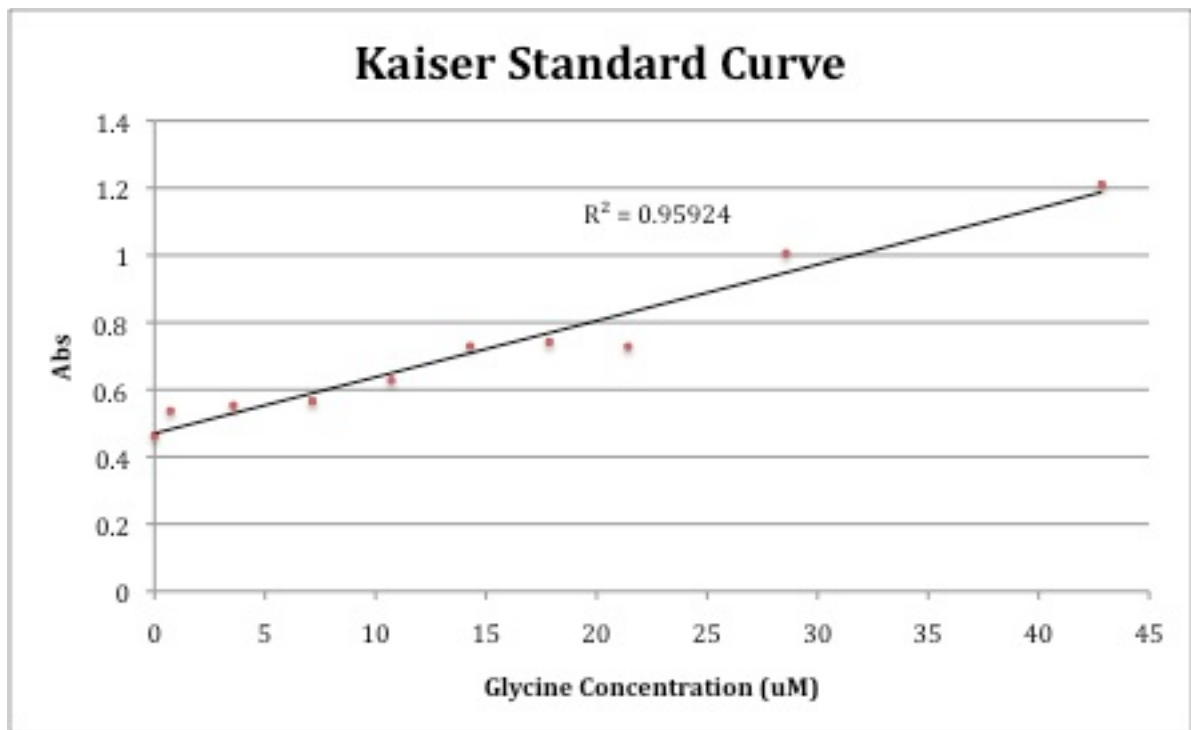
$$\% \textit{IronOxide} = \frac{\textit{massafter600Cbake}}{\textit{massafter150Cbake}} \quad (\text{Eqn 2.2})$$

### **2.5.2 Dynamic Light Scattering and Zeta Potential Analysis**

Particle stability was examined using a Malvern ZetaPlus 90ZS Zetasizer instrument. Particles were typically dispersed in a low concentration electrolyte solution (1 mM NaCl or 1/1000 PBS buffer). See section 1.2.10.4 for further details on DLS/Zeta potential measurements.

### **2.5.3 Determining Available Primary Amine Concentration by Kaiser Assay Analysis**

A colorimetric kit used to determine the primary amine content in a solution was purchased from Sigma. The assay is ninhydrin based and a deep blue color occurs in the presence of primary amines. The assay was calibrated using a glycine standard curve (Figure 2.9).<sup>54</sup> A 96 well plate was used in order to reduce error associated with the test. Results for this assay should not be taken at face value. Porous hydrogel particles most likely have a large amount of primary amines beneath the surface of the particle that may react with the ninhydrin to give a larger value than would be expected. Additionally, particles in spectrophotometric studies are known to cause scattering that can potentially skew the results. To circumvent this issue, the assay solution was filtered using a centrifugal filter to separate the particles prior to spectrophotometric analysis.



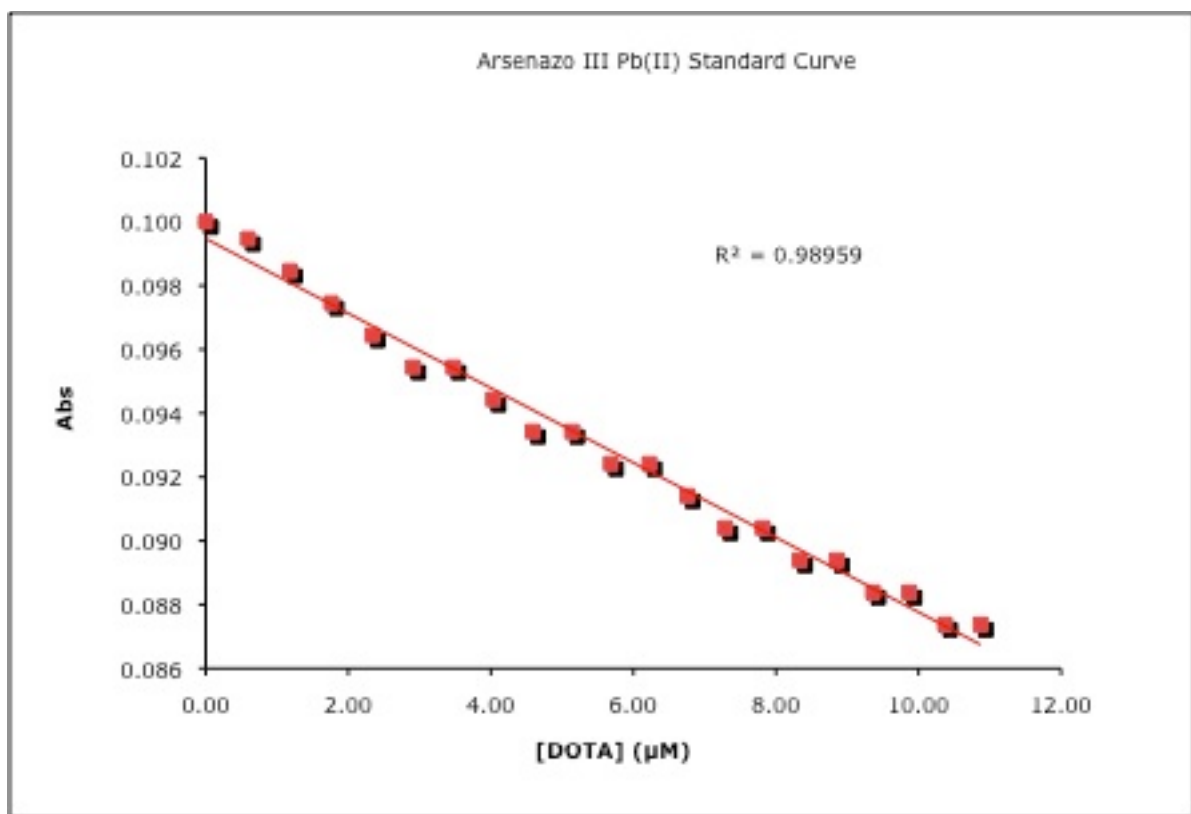
**Figure 2.9** Standard curve showing the linear relationship of absorbance at 405 nm vs primary amine concentration.

Amine concentration was determined for 200 x 200 nm cylindrical particles before and after PEGylation. Prior to PEGylation, the Kaiser assay showed that there were, on

average, ~44,000 primary amines available. On a weight percent basis, this corresponds to 45 % of the total primary amines available per particle. It is unlikely that this large of a percentage of the primary amines are actually available on the surface of the particle. Therefore, it is believed that the ninhydrin was able to penetrate into the particle and react with amines buried deep within.

#### **2.5.4 Determining DOTA Surface Concentration by Arsenazo III Transchelation Assay Analysis**

DOTA concentrations were determined using another, different, colorimetric assay.<sup>61</sup> The Arsenazo III assay is a transchelation assay based on the loose complexation of Pb(II) with Arsenazo III (pink in color). In the presence of DOTA, Pb(II) is quantitatively removed from Arsenazo III causing the arsenazo III to change colors. When using this assay with particles that may nonspecifically bind to metal (ie. particles heavy in primary amines or carboxylic acid) it is a good idea to use blank particles (particles without DOTA) as a control. See the standard curve in Figure 2.10.



**Figure 2.10** Standard curve demonstrating the linear relationship of absorbance at 630 nm vs the concentration of DOTA.

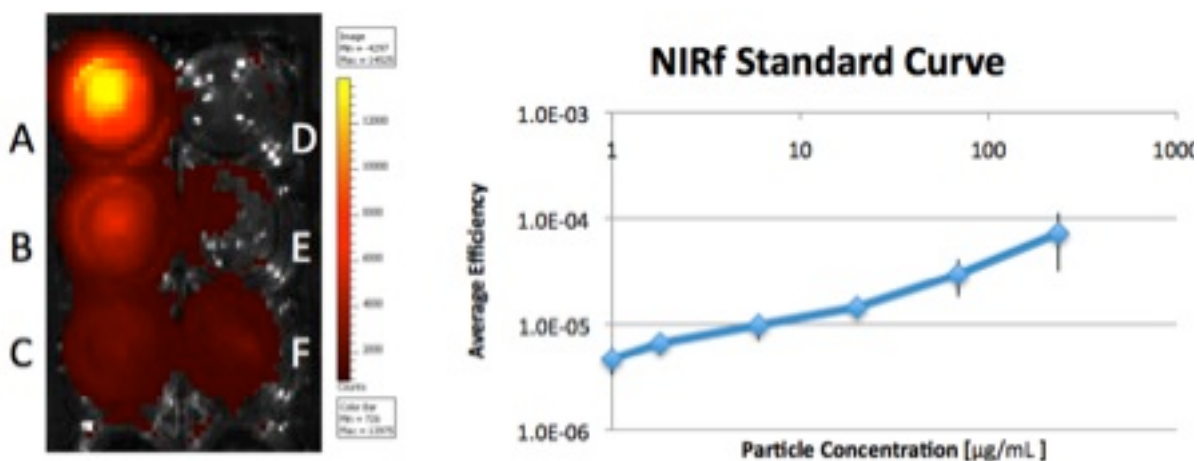
Using the concentration of the particles, the estimated mass per particle ( $1.5 \times 10^{-9}$  g / particle), and the determined DOTA concentration, it was possible to find the number of DOTA per particle. The amount of DOTA per particle appeared to be somewhat dependent on the particle size. For example the large particles (200 nm diameter, 200 nm height cylinders and 80 nm diameter, 2000 nm length wormlike particles) had ~25,000 DOTA per particle (0.130 DOTA / nm<sup>2</sup>). The smaller 80 x 90 nm particles had only ~3,300 DOTA per particle (0.129 DOTA / nm<sup>2</sup>). This was a relatively high number of DOTA which may have been a unique factor contributing to the highly pH sensitive zeta potential. It was suspected that this pH dependence may have been the primary cause of high lung accumulation in *in vivo* studies.



### 2.5.5 Characterization of Near Infrared Particle Fluorescence

For NIRf imaging, particles were imaged using a Ivis Kinetic Optical Imaging system equipped with a EMCCD camera. An excitation filter of 640 nm and an emission filter of 740 nm were utilized. The following parameters were used during NIRf imaging: f number, binning factor, field of view, and exposure times were 1, 4, 12.5, and 5 – 30 seconds respectively. Data from animal and phantom study samples were acquired using Living Image® software. The total efficiency from each region of interest (ROI) derived from the total counts per sample was used for comparison across animals, tissue samples, and phantom studies.

A phantom study of 200 nm diameter, 200 nm height cylinders chelated with “cold” copper was performed with a standard dilution curve of particles starting at 235  $\mu\text{g} / \text{mL}$  down to 1.8  $\mu\text{g} / \text{mL}$ . Particles were prepared in 2 % agarose gel in 0.9 % saline solution. Particles exhibited detectable levels of fluorescence throughout this range of concentration (see Figure 2.11). Therefore, in a mouse with an estimated 1.5 mL of blood, and an injected dose of 250  $\mu\text{g}$ , concentrations as low as 1.1 % the injected dose (i.d.) would be detectable.

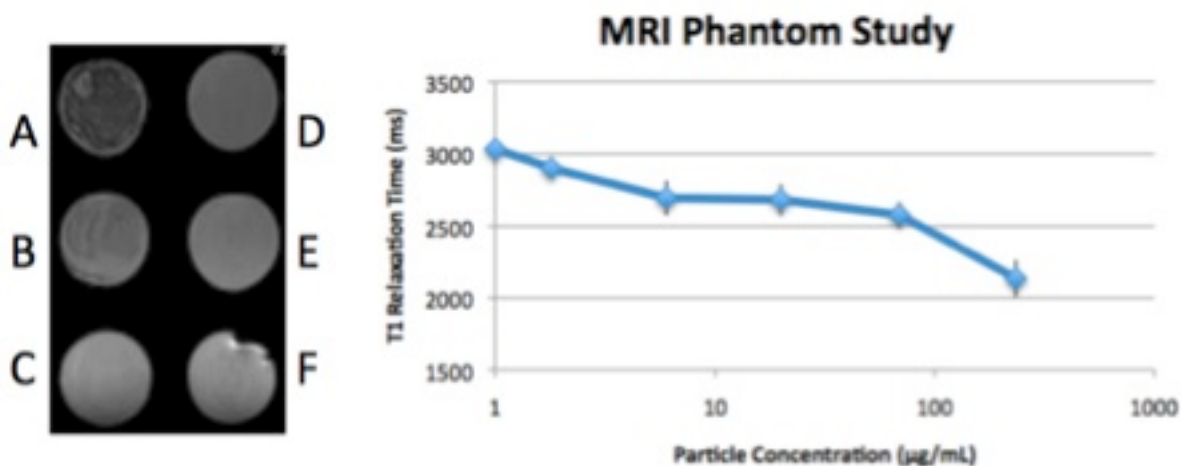


**Figure 2.11** A NIRf phantom study of particles in 2 wt % agarose gel was performed to determine an estimate of the limit of detection for particles *in vivo*. Particle concentrations are 235 (A), 69 (B), 11 (C), 5.6 (D), 1.8 (E), 0 mg / mL (F).

### 2.5.6 Characterization of MRI Particle Contrast

For MRI imaging, particles were imaged using a 9.4 Tesla (T) Bruker Biospec instrument. The instrument was equipped with a 25 mm QuadTransceiver mouse coil. A small animal monitoring system was used to monitor temperature and breathing rate. All scans were gated for animal breathing.

A phantom study of 200 nm diameter, 200 nm height cylinders was performed using the same sample that was used for the NIRf phantom study. A RARE VTR T1 scanning sequence was used to quantify T1 relaxation times of the particles in agarose. As demonstrated in figure 2.12, particles caused a marked decrease in intensity especially at high concentrations (69 - 235 mg / mL). Lower concentrations however did not appear to significantly alter the T1 relaxation time. As a result, for MRI to be useful for *in vivo* imaging with these particles, a targeted approach was most likely necessary to obtain high enough concentrations to create significant contrast.



**Figure 2.12** RARE VTR T1 Map of standard dilution phantom (left) and plot of T1 relaxation time vs particle concentration (right). Particle concentrations are 235 (A), 69 (B), 11 (C), 5.6 (D), 1.8 (E), 0 mg / mL (F).

### 2.5.7 Characterization of PRINT Particles as PET Contrast Agents

Cylindrical 200 nm diameter, 200 nm height cylinders were chelated to  $^{64}\text{Cu}$  at the Biomedical Research and Imaging Center (BRIC) at the University of North Carolina at Chapel Hill (UNC-CH). Radio labeling efficiency was calculated as the amount of radioactivity bound to the particles divided by the total radioactivity in the chelation reaction (Equation 2.3). To determine the radio labeling efficiency, a known amount of activity of  $^{64}\text{Cu}$  was incubated with particles as described above. Particles then were purified by centrifugal filtration. The radioactivity remaining in the filter was bound to the particles. Typical radiolabeling efficiencies were between 85 – 90 %, a highly effective reaction yield when compared with work by other researchers.<sup>55</sup>

$$\text{Radiolabeling efficiency} = \frac{A_{\text{particles}}}{A_{\text{total}}} \quad (\text{Eqn 2.3})$$

Radiochemical purity, defined as the radioactivity in a particle dispersion that is bound to the particle, was also determined. To find the free  $^{64}\text{Cu}$  and  $^{64}\text{Cu}$ -DTPA, an instant thin layer chromatography technique (I-TLC) was performed according to the literature.<sup>52</sup> Two strips of silica-impregnated paper (Whatman, Inc.) were spotted with a particle dispersion that was ready for injection. The strips were developed according to a procedure developed by Scheinberg.<sup>62</sup> The first strip was developed in 10 mM ethylenediamine tetraacetic acid (EDTA) while the second strip was developed in 10 mM NaOH in 0.9% saline solution. Free  $^{64}\text{Cu}$  travels at the solvent front in EDTA and is found at  $R_f = 1.0$ . Free  $^{64}\text{Cu}$ -DTPA travels at the solvent front of NaOH and is stabilized by the sodium chloride in this solution and, therefore, it ends up at  $R_f = 1.0$ . Particles did not travel with either solvent front and had the value  $R_f = 0.0$ . Strips were cut in half at  $R_f = 0.5$ . Radiochemical purity was determined using equation 2.4. Typical radiochemical purities were 95-99%. Higher

purities were possible by repeating the purification steps, however, particle loss was substantial with each additional step and 99% purity was therefore deemed sufficient.

$$\textit{RadiochemicalPurity} = \frac{\textit{ActivityBound}}{\textit{TotalActivity}} \quad (\text{Eqn 2.4})$$

The specific activity of the particles was calculated by dividing the activity of particles in solution by the mass of the particles in solution (see Equation 2.5). According to this equation particle activity was typically > 5 Ci / g. Specific activities of 15 Ci / g have been reported for nanoparticle-based imaging using PET.<sup>52</sup> Other groups have also reported much higher specific activities (>100 Ci / g) for PET imaging but these groups typically inject much lower quantities of particles (ie. 0.25 mg particles / kg animal).<sup>63</sup> With specific activities of 5 Ci / g, it was possible to inject animals with particle concentrations similar to what have been performed in the past in our group (3.3 mg / mL)<sup>16</sup> and still get high enough activity for PET imaging over 24 hrs (typically need 500 – 800 µCi).

$$\textit{SpecificActivity} = \frac{\textit{ParticleActivity}[\textit{Ci}]}{\textit{ParticleMass}[\textit{g}]} \quad (\text{Eqn 2.5})$$

## 2.6 *In Vivo* Imaging Study

All animal studies were conducted in accordance with the Animal Welfare Act and the Guide for Care and Use of Laboratory animals. The animal protocol was approved by the Institutional Animal Care and Use Committee (IACUC) for the UNC-CH. Healthy female BALB/c mice (6-8 weeks old, ~20 g) were injected using a tail vein catheter set up (Figure 2.13) which made it possible to get an image prior to and immediately post injection. Animals were anesthetized with 1.8-2% isofluorane. Breathing rate was either monitored using a small animal monitoring system or by constant visual inspection. Animal temperature was maintained using a warm air heating system for all MRI studies in which

animal core temperature, as measured by rectal thermometer, was used to keep the animal at a comfortable resting temperature. A 250  $\mu$ L bolus injection of 1 mg / mL ( $\sim$ 12.5 mg particle / kg mouse) was used in all experiments. Just prior to injection, particles were thoroughly sonicated (pulsed 1 second on one second off for 3 minutes) using a cup horn sonicator at 100 % power. This was done to reduce the occurrence of particle aggregation. After imaging animals were sacrificed and organs were harvested for further characterization. All PET scans were performed on n = 3 animals in order to demonstrate quantitative analysis of particle biodistribution and pharmacokinetics. Imaging performed using MRI and NIRf modalities was performed on one animal for each particle size in order to demonstrate proof of concept for imaging in multiple modalities with one particle.



**Figure 2.13** Cartoon of tail vein catheter setup.

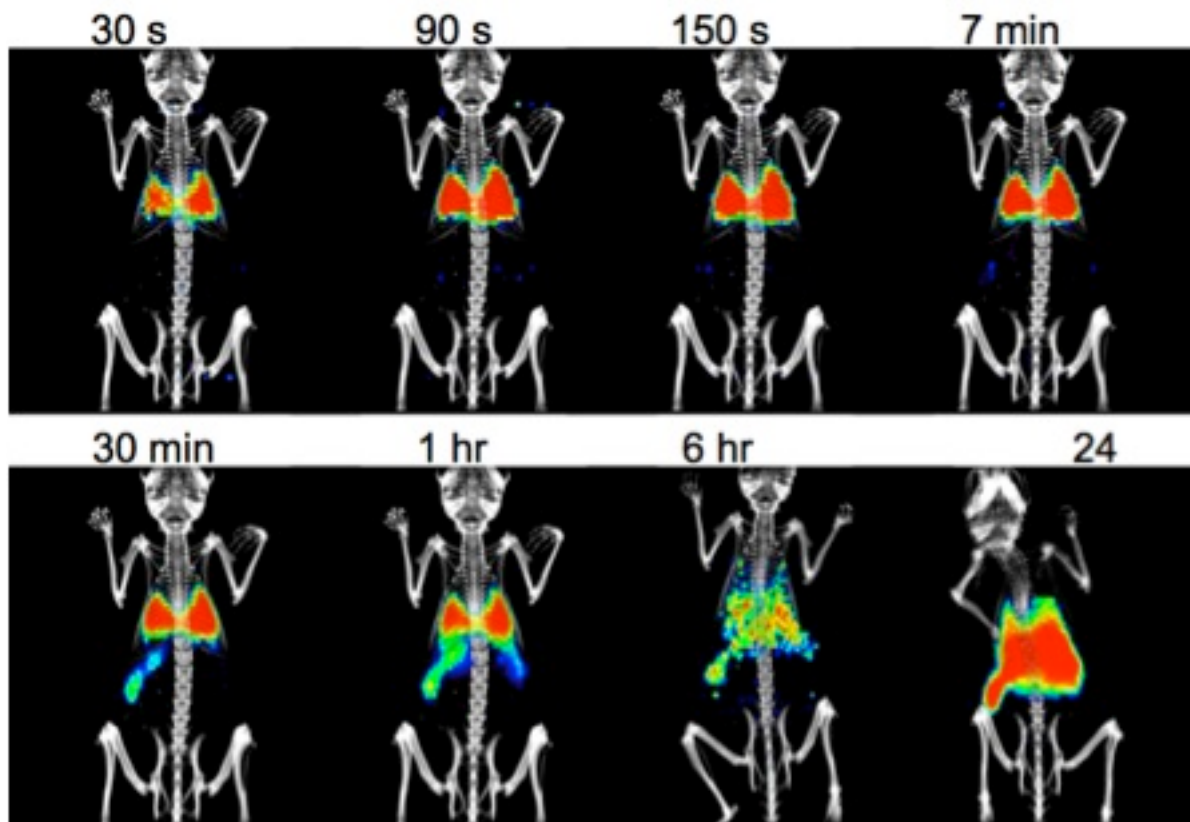
### **2.6.1 *In Vivo* PET/CT Results**

Animals were fitted with a tail vein catheter with a hold up volume of 50 – 100  $\mu$ L and placed in a GE Explore Vista PET / Computed Tomography (CT) small animal imaging system. Animals were imaged by CT prior to injection. PET scanning was started as soon as particle injection began (bolus injections lasted 30 seconds). The images from CT and PET scans were overlaid using Amide software. Regions of interest were selected by hand.

Typically, the outline of an organ was selected in the PET or CT view. At least 5 focal planes were averaged together and used for each organ in an effort to reduce error.

A heparin / saline flush was used through the tail vein catheter to ensure that the entire dose had been administered to each animal. A dynamic scan lasting one hour was taken to monitor particle biodistribution over this time. Next, animals were scanned at 6 hours, and again at 24 hrs. Animals were then sacrificed and their organs were harvested for examination using a gamma counter.

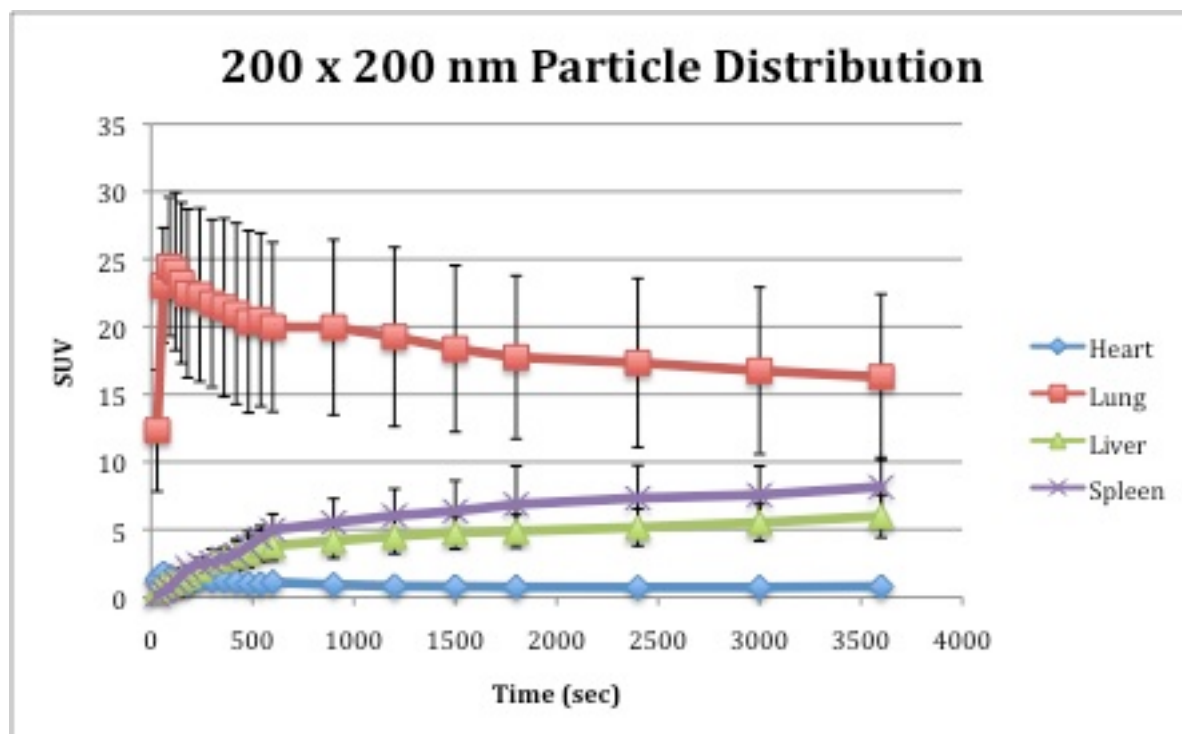
Particles were observed to travel through a major blood vessel to the heart where they were distributed to the lungs. Particles accumulated quickly in the lungs. They then were distributed much more slowly to the other organs. The majority of particles ended up in the liver, spleen, and lungs. Figure 2.14 demonstrates this effect in which one animal was injected with 200 nm diameter, 200 nm height cylinders and was imaged continuously for 1 hour, then again at 6 hours, and finally at 24 hrs. A large increase in intensity is observed first in the lungs. After about 30 minutes a significant accumulation of particles is observed in the spleen. Accumulation of particles in the liver can also be distinguished from 30 minutes on.



**Figure 2.14** A representative dynamic PET scan ( $t = 0 - 60$  min) and two static scans (6 and 24 hrs) of a mouse injected with 200 nm diameter, 200 nm height cylinders.

In addition to visual observation of the intensities of organs over time, it was possible to compare the relative intensities of the ROIs graphically. Figure 2.15 demonstrates the standard uptake value, or SUV, (Equation 2.6) of particles over time in the lung, liver, spleen, and heart. Here, it is readily apparent that there is a large accumulation of particles in the lung.

$$SUV = \frac{RadioactivityConcentrationInROI}{InjectedDose / AnimalWeight} \quad (Eqn. 2.6)$$



**Figure 2.15** Averaged SUV data (n = 3 mice) for particle accumulation in the liver, spleen, lung and heart.

All PRINT particles exhibited short, irregular blood circulation half-lives ( $t_{1/2}$ ). When compared to the literature (2.5  $\mu\text{m}$  length filomicelles  $t_{1/2} = 5.2$  days)<sup>35</sup>, these PRINT particles had relatively poor performance as shown by their short circulation times demonstrated in Table 2.3. The short half-life is probably the result of rapid uptake by the RES and entrapment of particles in capillary beds. This is supported largely by the high signal intensities found in the liver, spleen, and lungs. It is believed that this is largely due to the large number of DOTA ligands on the surface of the particle. Improved electrostatic and steric stability through optimized surface PEGylation will be required for improved circulation half-lives. Flexibility of the higher aspect ratio particles may also be an important factor in improving particle circulation times.

**Table 2.3** Particle half-life in blood circulation.

	Control	80 x 90 nm	80 x 360 nm	80 x 2000 nm	200 x 200nm
--	---------	------------	-------------	--------------	-------------



<b>Time (min)</b>	12.90	31.9	21.4	15.1	32.2
<b>Stdev (min)</b>	0.4	26.4	16.1	4.4	19.8

Over the first hour p.i., particle accumulation in the lungs was high for all four particle sizes. The total exposure, or area under the curve (AUC), of the lungs to particles was compared to the AUC of the liver and spleen (see Table 2.4). Lung exposure at 45 minutes was much higher than in the spleen or liver. After 24 hours exposure to particles, the liver and lungs experienced similar levels of exposure to the particles with the exception of the 80 x 360 nm particles. It is not fully understood why exposure of these particles to the lung is so much higher than to the liver and spleen. But our suspicion is that when the particles are injected (injection is pH 5, zeta potential is +15 mV) they are highly positive and may be targeted by the RES. Additionally, the level of DOTA per particle was maximized for these early studies in order to ensure positive results with <sup>64</sup>Cu chelation. As a result, PEG densities on the particle surface were not as high as one would like. Low PEG densities have been shown to lead to higher levels of particle aggregation and rapid elimination by the RES.<sup>64</sup>

**Table 2.4** Ratio of the AUC of the lungs to the liver and lungs to the spleen at 45 minute and 24 hour exposure times p.i. as a function of particle size.

	<b>Exp. Time</b>	<b>Control</b>	<b>80 x 90 nm</b>	<b>80 x 360 nm</b>	<b>80 x 2000 nm</b>	<b>200 x 200 nm</b>
<b>Lungs:</b>	<b>45 min</b>	1.5±1.2	11±4	13±5	4±2	6±4
<b>Liver</b>	<b>24 hr</b>	4.4±0.7	1.5±7	8±4	0.8±0.1	1.4±0.4
<b>Lungs:</b>	<b>45 min</b>		10±5	17±1	5.1±0.1	6±4
<b>Spleen</b>	<b>24 hr</b>		1.1±0.3	8±2	0.8±0.2	1±0.5

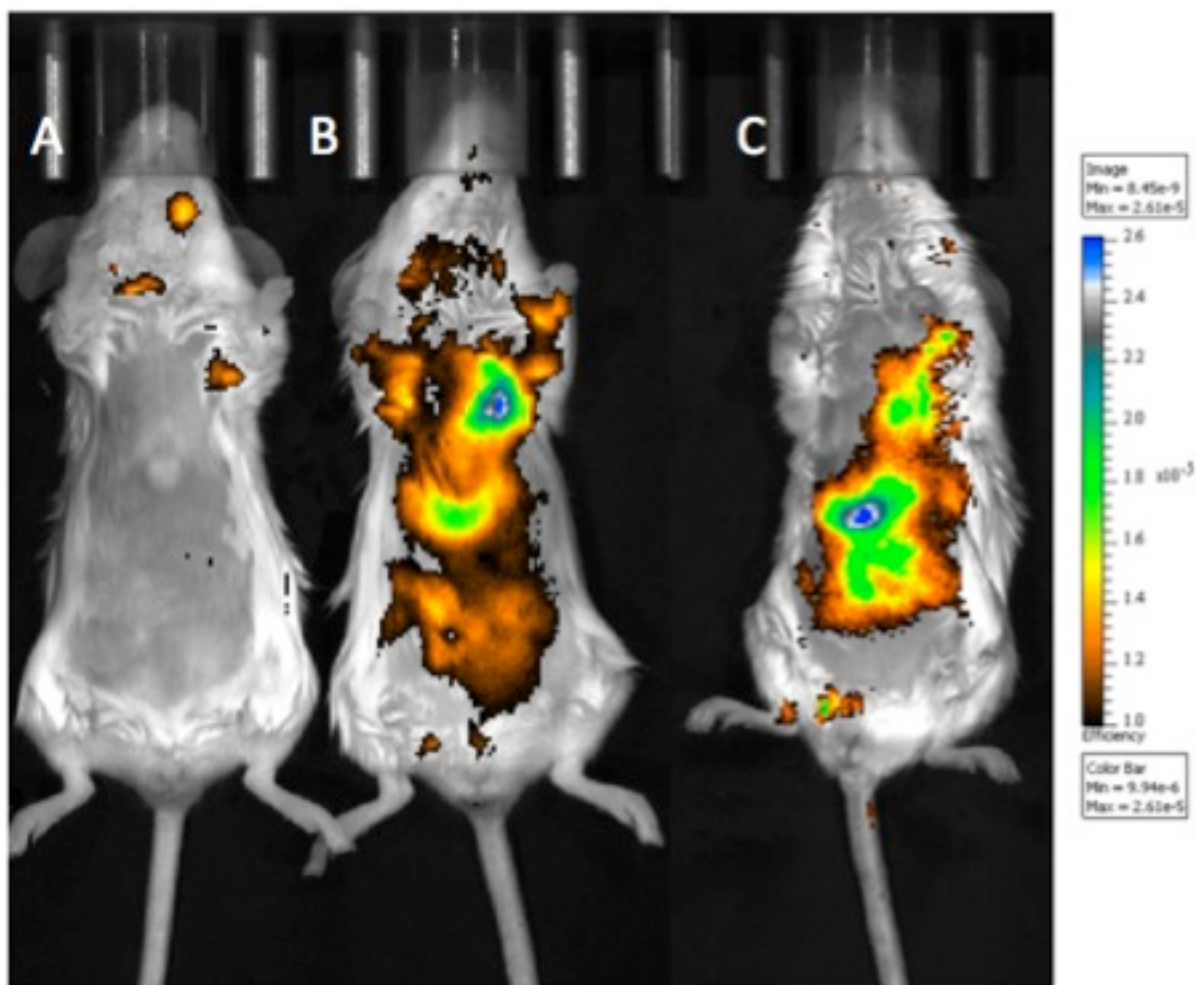
Rapid accumulation in the lung was most likely a result of the positive zeta potential (+27 mV) of the particles prior to injection. Particle concentration in the lungs decreased slowly over the first hour for all of the particle shapes with the exception of the worm-like particles (80 x 2000 nm). It is believed that the length of the particles may have made it difficult for the particles to become lodged in the small capillary beds of the lungs. Further analysis by confocal imaging and TEM will be necessary to elucidate the mechanism that differentiates the worm-like particles from the rest of the shapes in the lung.

## 2.6.2 *In Vivo* Near Infrared Fluorescence Results

In order to demonstrate the ability of the particles to act as a contrast agent for *in vivo* NIRf, one animal per particle size was imaged using Ivis Kinetic NIRf instrument. Animals were imaged at 1.5 hrs, 24 hrs, and after the animals were sacrificed at 24 hrs, their organs

were harvest and imaged. Organs from all of the four animals that were injected with particles and one control animal were compared side by side to show relative amounts of particle accumulation at 24 hrs.

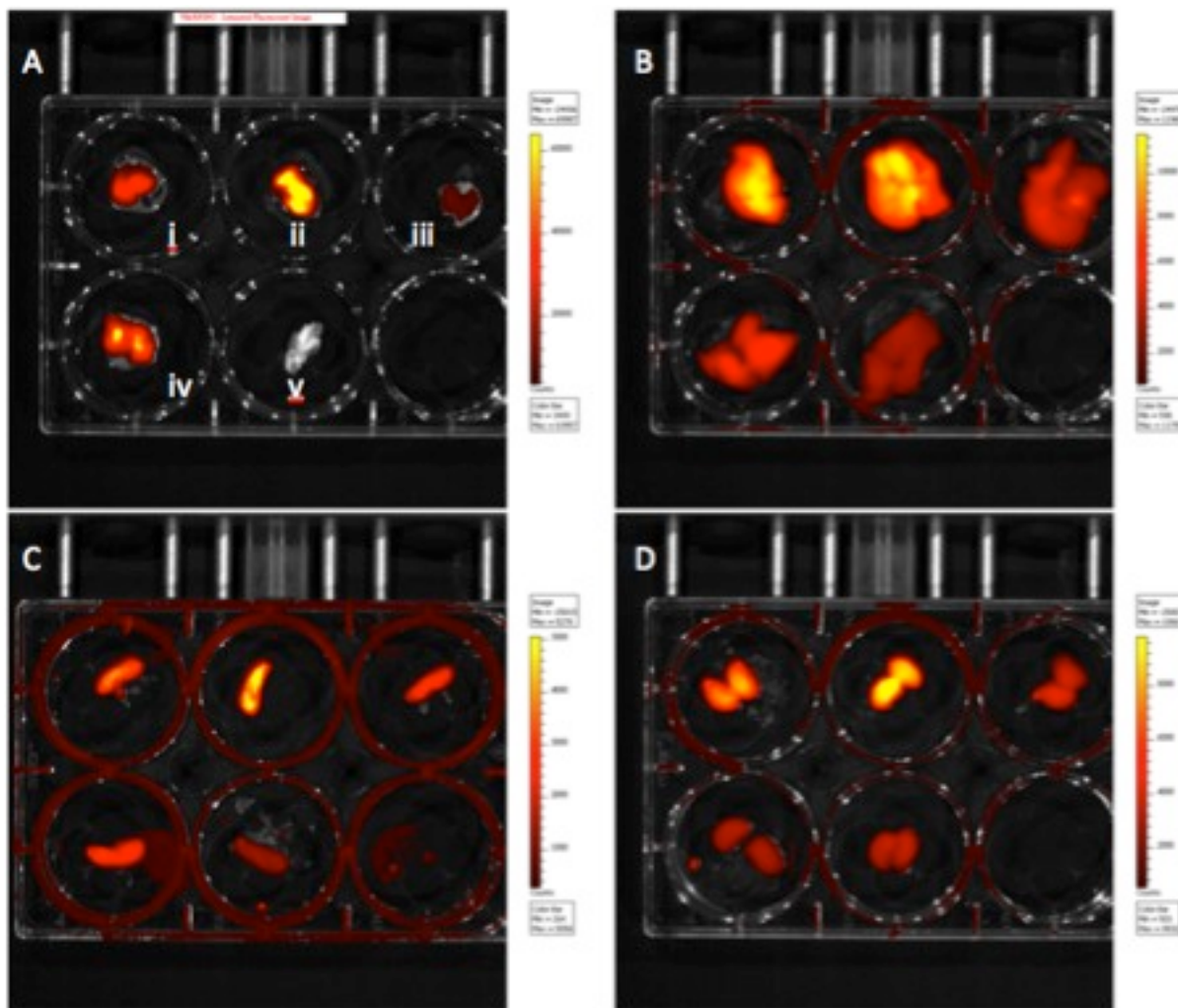
NIRf images of animals 1.5 hrs p.i. corresponded well with the results obtained by PET imaging. High levels of signal intensity were observed in the lungs for all particles as well as just below the lungs in the liver and spleen region. At 24 hrs, signal intensity in the lungs had decreased somewhat while intensity in the liver and spleen increased (see Figure 2.16). Imaging of live animals with NIRf is useful for superficial tumors and for qualitative analysis of particle distribution. Limited depth of penetration, scattering, and other artifacts associated with NIRf make this method inadequate for quantitative analysis of particle biodistribution. To get a better picture of particle biodistribution by NIRf, it was necessary to sacrifice the animal and harvest the organs.



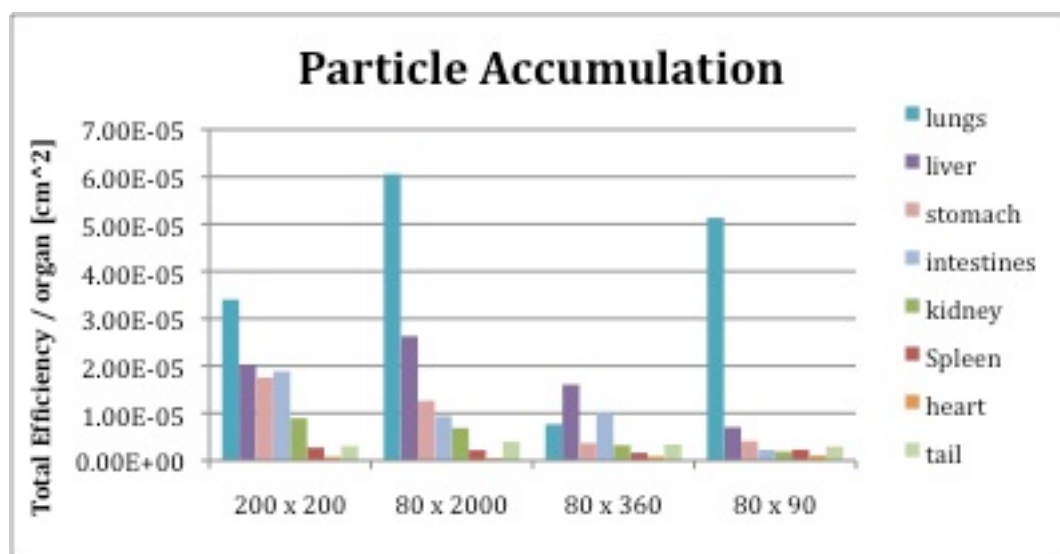
**Figure 2.16** NIRf images of a control mouse with no injected particles (A), a mouse injected with 200 x 200 nm cylindrical particles at 1.5 hrs (B), and the same mouse at 24 hrs (C).

Similar to the PET studies, organs associated with the RES had the highest signal intensities. In general, the lungs showed the highest particle accumulation, followed by the liver, and then the spleen. Particle accumulation in different organs is demonstrated in Figure 2.17 and graphically in Figure 2.18. It is difficult to draw conclusions from these results as only one animal was used per particle size. The use of one animal was deemed sufficient for the purpose here of demonstrating contrast *in vivo* with shape and size specific particles. As a result, one should pay attention to the relative intensities of organs from one animal (ie. lung, liver, and spleen from mouse 1) but not compare the intensity of the same

organs between different animals (livers from mouse 1, 2, and 3). Obviously, for a more detailed study of particle biodistribution, 3 or more animals should be used.



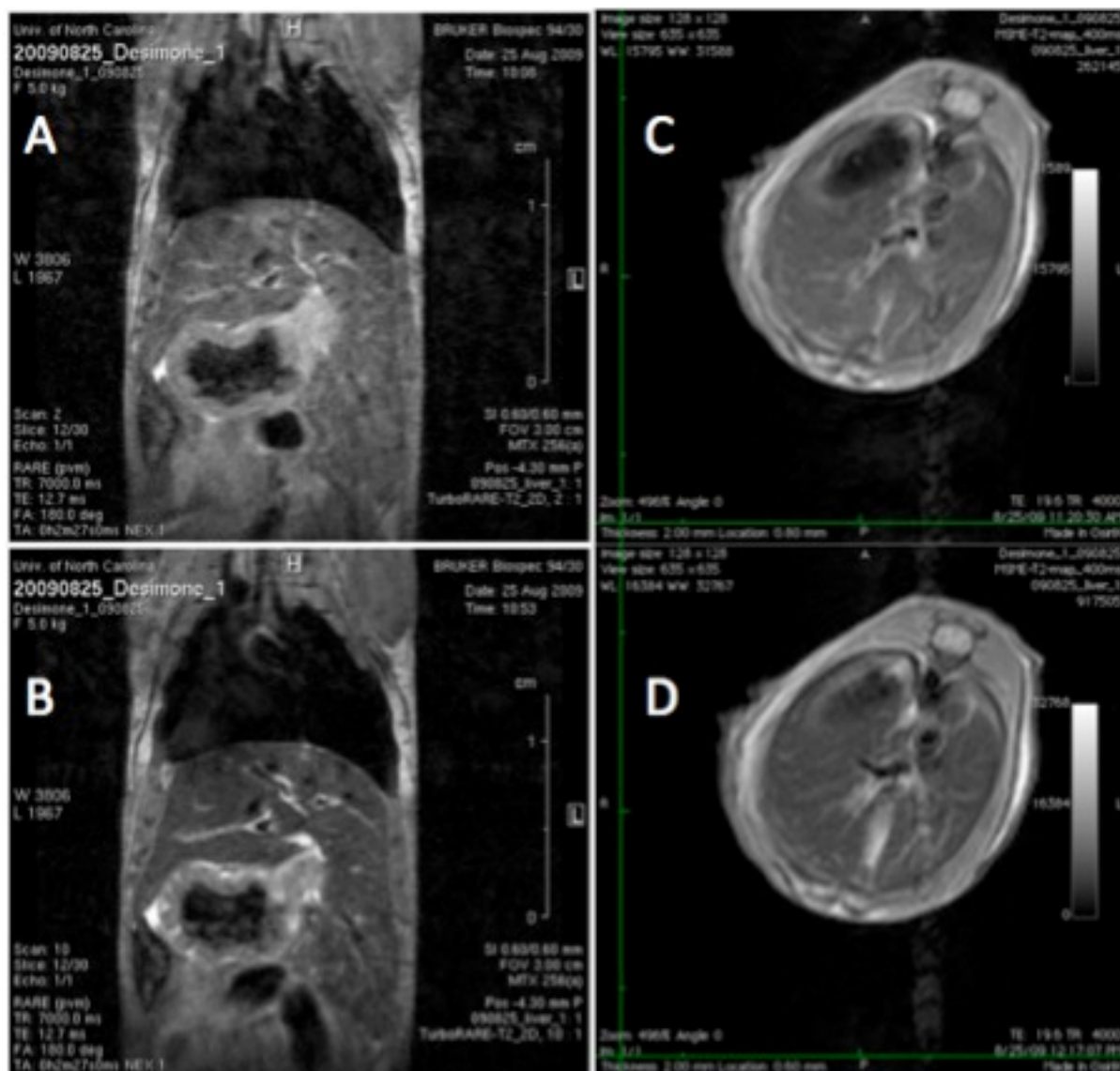
**Figure 2.17** NIRf images of lungs (A), liver (B), spleen (C), and kidney (D) of mice injected with 200 x 200 nm (i), 80 x 2000 nm (ii), 80 x 360 nm (iii), and 80 x 90 nm (iv) PRINT particles. A fifth mouse (v) was not injected with particles and was used as a control.



**Figure 2.18** Particle accumulation determined by NIRf as a function of particle size at 24 hrs p.i.

### 2.6.3 *In Vivo* MRI Results

After inserting a tail vein catheter with a hold up volume of 50 – 100  $\mu$ L, animals were stabilized in the MRI (BR = 60 – 70 bpm, Temperature = 30 – 33  $^{\circ}$ C). Animals were scanned prior to injection using a variety of different scanning parameters including coronal TurboRARE-T2 2D and FLASH multislice as well as axial MSME T2 maps. One animal was injected for each of the 4 particle sizes. Animals exhibited minor decreases in intensity in the liver 1 hour post injection (Figure 2.17). Within error, no quantifiable change in relaxation time was observed but the gray parenchyma of the liver did appear slightly darker. It is obvious that in order for these particles to be useful as contrast agents for MRI, higher local concentrations would be necessary. This is possible by either increasing the injected dose, or by the addition of targeting ligands to the surface of the particle.



**Figure 2.19** *In vivo* MRI scans of a mouse injected with 200 x 200 nm cylindrical particles containing iron oxide nanocrystals. Coronal scans of the mouse take prior to injection (A) and 1 hr p.i. (B) show the vessels delineating the liver parenchyma (grey) just below the dark mass of the lungs. Axial T2 mapping scans prior to (C) and 1 hr p.i. (D) show a minor decrease in signal intensity in the liver.

## 2.7 Summary

A number of studies were reviewed in which polymer-based nanoparticles have been used as carriers for therapeutics and imaging contrast agents. Recent studies have indicated that anisotropic, worm-like particles can enhance circulation time in comparison to previous

studies with spherical particles. Studies such as these lead us to believe that the ability to systematically modify the size and shape of particles may allow us to rationally alter the biodistribution of nanotherapeutics. The PRINT method has allowed us the ability to fabricate multimodal contrast agents of any shape and size allowing us to track the distribution of the particles using a variety of methods. With this new capability, completely monodisperse samples of a variety of particle shapes have been prepared allowing the quantitative and qualitative analysis of particle biodistribution using PET, MRI, and NIRf.

## **2.8 Future Directions**

A number of important questions remain to be answered in the field of nanotherapeutics. Among these questions, some of the most crucial are also the most basic. Can size and shape play an important role in particle circulations times? Will size and shape be important in tumor uptake and retention? Do extreme particle aspect ratios (10:1 and higher) help prevent phagocytosis and allow for prolonged circulation in the blood? The ability to quantify particle biodistribution using radio labeled particles demonstrated in this work will make it possible to rapidly and quantitatively address many of these questions.

Before this happens however, a number of small but significant particle optimization studies should be performed. First off, it is imperative that a strong understanding of particle surface chemistry is obtained. Opsonization and binding of larger proteins has been shown to have deleterious effects on particle elimination from the blood stream by the RES.<sup>65</sup> High density brush conformations of PEG on the surface of nanoparticles has been shown to reduce the rate of clearance from the blood. Optimization of high density PEG on the surface of PRINT particles will be crucial going forward. A number of rapid studies can be performed using a high throughput flow cytometry-based method capable of running up to 96

experiments in less than 30 minutes. Additionally, using PRINT, it is possible to screen surface functionalization chemistries using particles bound to a harvesting layer. In this manner, one can envision running multiple iterations of a reaction on a small batch of particles and rapidly zero in on optimal conditions for PEGylation.

Before PEG studies are performed, it will be necessary to pare down the surface density of DOTA. In this work it was shown that large portion of the particle surface was coated with DOTA. While this high level of DOTA made Cu<sup>64</sup> conjugation straightforward, it also led to instability and aggregation issues that could be solved if more particle surface area was available for PEG which has been shown to work well as a steric stabilizer. It should be possible to reduce the density of DOTA on the surface of the particle by at least 1000 fold and still get acceptable radio labeling levels for PET imaging. This would lead to a large increase of available surface area for PEG functionalization. The resulting particles would still be visible using PET/CT imaging but would be less prone to aggregation.

Another crucial parameter that has yet to be examined is the effect that particle modulus has on circulation times in the blood. It is understood that red blood cells (7  $\mu\text{m}$  diameter) are capable of circulating for prolonged periods of time. In order to navigate capillary beds that contain passages only 3  $\mu\text{m}$  in diameter, these cells must be able to flex and contort themselves up to 100 % of their own length. Indeed, it is believed that part of the criteria for red blood cell removal is based on rigidification of the cells over time.<sup>66</sup> Once the cells are no longer able to bend and stretch, they become trapped in the sinusoids of the spleen and are eliminated from the blood stream. On a smaller scale nanoparticles may have similar interactions with the sinusoids of the liver and spleen. With the ability to manipulate



particle modulus without changing particle size and shape using the PRINT process, we are at a distinct advantage to try to answer this question.

## References

1. Wong, S. Y. P., J. M.; Putnam, D., *Prog Polym Sci* **2007**, *32*, 799-837.
2. Zamboni, W. C., *Oncologist* **2008**, *13* (3), 248-260.
3. Nie, S. X., Y.; Kim, G., J.; Simons, J., W., *Annual Review in Biomedical Engineering* **2007**, *9*, 257-288.
4. Torchilin, V. P., *Nature Reviews Drug Discovery* **2005**, *4*, 145-160.
5. Jeong, J. H. K., S., W.; Park, T., G., *Prog Polym Sci* **2007**, *32* (11), 1239-1274.
6. Heidel, J., D.; Mishra, S.; Davis, M., E., *Gene Therapy and Gene Delivery Systems. Advances in Biochemical Engineering/Biotechnology* **2005**, *99*, 7-39.
7. Duncan, R., *Nature Reviews Drug Discovery* **2003**, *2*, 347-360.
8. Pasut, G., Veronese, F., M., *Programmable Polymer Science* **2007**, *32* (8-9), 933-961.
9. Christian, D.; Cai, S.; Garbuzenko, O.; Harada, T.; Zajac, A.; Minko, T.; Discher, D. E., *Mol Pharm* **2009**.
10. Park, J.; von Maltzahn, G.; Zhang, L.; Schwartz, M.; Ruoslahti, E.; Bhatia, S.; Sailor, M., *Adv. Mater.* **2008**, *20* (9), 1589.
11. Whitesides, G. M. O., E.; Takayama, S.; Jiang, X., *Annual Review in Biomedical Engineering* **2001**, *3*, 335-373.
12. Gates, B., D.; Xu, Q.; Stewart, M.; Ryan, D.; Willson, C., G., *Chem Rev* **2005**, *105* (4), 1171-1196.
13. Rolland, J. P.; Maynor, B. W.; Euliss, L. E.; Exner, A. E.; Denison, G. M.; Desimone, J. M., *J Am Chem Soc* **2005**, *127* (28), 10096-100.
14. Maynor, B. W.; Larue, I.; Hu, Z.; Rolland, J. P.; Pandya, A.; Fu, Q.; Liu, J.; Spontak, R. J.; Sheiko, S. S.; Samulski, R. J.; Samulski, E. T.; Desimone, J. M., *Small* **2007**, *3* (5), 845-849.
15. Olson, D., A.; Gratton, S., E., A.; DeSimone, J., M.; Sheares, V., V., *J Am Chem Soc* **2006**, *128* (41), 13625-13633.
16. Gratton, S. E. A.; Pohlhaus, P. D.; Lee, J.; Guo, J.; Cho, M.; Desimone, J. M., *Journal of Controlled Release* **2007**, *121* (1-2), 10-18.

17. Gratton, S. E. A.; Ropp, P. A.; Pohlhaus, P. D.; Luft, J. C.; Madden, V. J.; Napier, M. E.; Desimone, J. M., *Proc Natl Acad Sci USA* **2008**, *105* (33), 11613-8.
18. Gratton, S. E. A.; Williams, S. S.; Napier, M. E.; Pohlhaus, P. D.; Zhou, Z.; Wiles, K. B.; Maynor, B. W.; Shen, C.; Olafsen, T.; Samulski, E. T.; Desimone, J. M., *Acc Chem Res* **2008**, *41* (12), 1685-95.
19. Herlihy, K. P.; Nunes, J.; Desimone, J. M., *Langmuir : the ACS journal of surfaces and colloids* **2008**, *24* (16), 8421-6.
20. Petros, R. A.; Ropp, P. A.; Desimone, J. M., *J Am Chem Soc* **2008**, *130* (15), 5008-9.
21. Kelly, J. Y.; Desimone, J. M., *J Am Chem Soc* **2008**, *130* (16), 5438-9.
22. Rejman, J. O., V.; Zuhorn, I., S.; Hoekstra, D., *Biochim Biophys Res Commun* **2004**, *377*, 159-169.
23. Zauner, W. F., N., A.; Haines, A., M., R., *Journal of Controlled Release* **2001**, *71* (1), 39-51.
24. Win, K., Y.; Feng, S-S, *Biomaterials* **2005**, *26*, 2713-2722.
25. Hu, Y. X., J.; Tong, Y., W.; Wang, C-H., *Journal of Controlled Release* **2007**, *188*, 7-17.
26. Goodman, T., T.; Olive, P., L.; Pun, S., H., *International journal of nanomedicine* **2007**, *2* (2), 265-274.
27. Dreher, M., R.; Liu, W.; Michelich, C., R.; Dewhirst, M., W.; Yuan, F., *Journal of the National Cancer Institute* **2006**, *98* (5), 335-344.
28. Minchin, R., *Nature Nanotechnology* **2008**, *3* (1), 12-13.
29. Champion, J. A.; Mitragotri, S., *Proc Natl Acad Sci USA* **2006**, *103* (13), 4930-4.
30. Decuzzi, P. F., M., *Biomaterials* **2006**, *27* (30), 5307-5314.
31. Champion, J. A.; Katare, Y. K.; Mitragotri, S., *Journal of controlled release : official journal of the Controlled Release Society* **2007**, *121* (1-2), 3-9.
32. Champion, J. A.; Mitragotri, S., *Pharm Res* **2009**, *26* (1), 244-249.
33. Mader, K. B., G.; Domb, A.; Elmalak, O.; Langer, R., *J Pharm Sci* **1997**, *86* (1), 126-134.
34. Goldberg, M. L., R.; Jia, X., *J Biomater Sci Polym Ed* **2007**, *18* (3), 241-268.

35. Geng, Y.; Dalhaimer, P.; Cai, S.; Tsai, R.; Tewari, M.; Minko, T.; Discher, D. E., *Nat Nanotechnol* **2007**, 2 (4), 249-55.
36. Conner, S., D.; Schmid, S., L., *Nature* **2003**, 422, 37-44.
37. Champion, J. A.; Katare, Y. K.; Mitragotri, S., *Proc Natl Acad Sci USA* **2007**, 104 (29), 11901-4.
38. Dumond, J.; Low, H., *Adv. Mater.* **2008**, 20 (7).
39. Gupta, A. W., S., *IEEE Trans Nanobioscience* **2004**, 3 (1), 66-73.
40. Thomassen, T. W., U., N.; Gundersen, H., K.; Fahlvik, A., K.; Aune, O., *Magn Reson Imaging* **1991**, 9, 255-258.
41. LaConte, L., E., W.; Nitin, N.; Zurkiya, O.; Caruntu, D.; O'Connor, C., J., *J Magn Reson Imaging* **2007**, 26, 1634-1641.
42. Kim, B. Y. S. Q., J-M; Wang, J., P.; Taton, T., A., *Nano Lett* **2005**, 5 (10), 1987-1991.
43. Park, J.; von Maltzahn, G.; Zhang, L.; Derfus, A.; Simberg, D.; Harris, T.; Ruoslahti, E.; Bhatia, S.; Sailor, M., *Small* **2009**.
44. Caravan, P., *Chem. Soc. Rev.* **2006**, 35 (6), 512.
45. Turner, J. L.; Pan, D.; Plummer, R.; Chen, Z.; Whittaker, A. K.; Wooley, K. L., *Adv. Funct. Mater.* **2005**, 15 (8), 1248-1254.
46. Accardo, A. T., D.; Aloj L.; Arra, C., *Chem Med Chem* **2008**, 3 (594-602).
47. Rudovsky, J. B., M.; Hermann, P.; Hardcastle, K., I.; Lukes, I., *17* **2006**, 4 (975-987).
48. Kim, J., S.; Rieter, W. J.; Taylor, K., M., L.; An, H.; Lin, W., *J Am Chem Soc* **2007**, 129 (29), 8962-8963.
49. Jagielski, N.; Sharma, S.; Hombach, V.; Mailänder, V.; Rasche, V.; Landfester, K., *Macromol. Chem. Phys.* **2007**, 208 (19-20), 2229-2241.
50. Herlihy, K. P., Brannen, C., L.; Lin, Weili; An, Hongyu; DeSimone, J., M., *Proc 236th ACS Natl Mtg* **2008**.
51. Sun, G.; Xu, J.; Hagooly, A.; Rossin, R.; Li, Z.; Moore, D. A.; Hawker, C. J.; Welch, M. J.; Wooley, K. L., *Adv. Mater.* **2007**, 19 (20), 3157-3162.

52. McDevitt, M. R.; Chattopadhyay, D.; Jaggi, J. S.; Finn, R. D.; Zanzonico, P. B.; Villa, C. H.; Rey, D.; Mendenhall, J.; Batt, C. A.; Njardarson, J. T.; Scheinberg, D. A., *PLoS ONE* **2007**, 2 (9), e907.
53. McDevitt, M. R.; Chattopadhyay, D.; Kappel, B. J.; Jaggi, J. S.; Schiffman, S. R.; Antczak, C.; Njardarson, J. T.; Brentjens, R.; Scheinberg, D. A., *J Nucl Med* **2007**, 48 (7), 1180-9.
54. Villa, C. H.; McDevitt, M. R.; Escorcia, F. E.; Rey, D.; Bergkvist, M.; Batt, C.; Scheinberg, D. A., *Nano Lett* **2008**.
55. Liu, Z.; Cai, W.; He, L.; Nakayama, N.; Chen, K.; Sun, X.; Chen, X.; Dai, H., *Nat Nanotechnol* **2007**, 2 (1), 47-52.
56. Gillies, R., *Journal of Cellular Biochemistry* **2002**, 87.
57. Jarrett, B. R.; Gustafsson, B.; Kukis, D. L.; Louie, A. Y., *Bioconjug Chem* **2008**, 19 (7), 1496-504.
58. Cherry, S., *The Journal of Clinical Pharmacology* **2001**, 41 (5), 482-491.
59. Thompson, K. L.; Read, E. S.; Armes, S. P., *Polymer Degradation and Stability* **2008**, 93 (8), 1460-1466.
60. Pridgen, E. M.; LANGER, R.; Farokhzad, O. C., *Nanomedicine (London, England)* **2007**, 2 (5), 669-80.
61. Dadachova, E.; Chappell, L.; Brechbiel, M., *Nucl Med Biol* **1999**, 26 (8), 977-982.
62. McDevitt, M. R.; Finn, R. D.; Ma, D.; Larson, S. M.; Scheinberg, D. A., *J Nucl Med* **1999**, 40 (10), 1722-7.
63. Sun, G.; Hagooley, A.; Xu, J.; Nyström, A. M.; Li, Z.; Rossin, R.; Moore, D. A.; Wooley, K. L.; Welch, M. J., *Biomacromolecules* **2008**, 9 (7), 1997-2006.
64. GREF, R.; Lück, M.; QUELLEC, P.; Marchand, M.; Dellacherie, E.; Harnisch, S.; BLUNK, T.; Müller, R., *Colloids and surfaces B, Biointerfaces* **2000**, 18 (3-4), 301-313.
65. Owens, D. E.; Peppas, N. A., *International Journal of Pharmaceutics* **2006**, 307 (1), 93-102.
66. Moghimi, S. M.; Hunter, A. C.; Murray, J. C., *Pharmacol Rev* **2001**, 53 (2), 283-318.

## **Section 3: Microscale Particle Fabrication and Analysis**

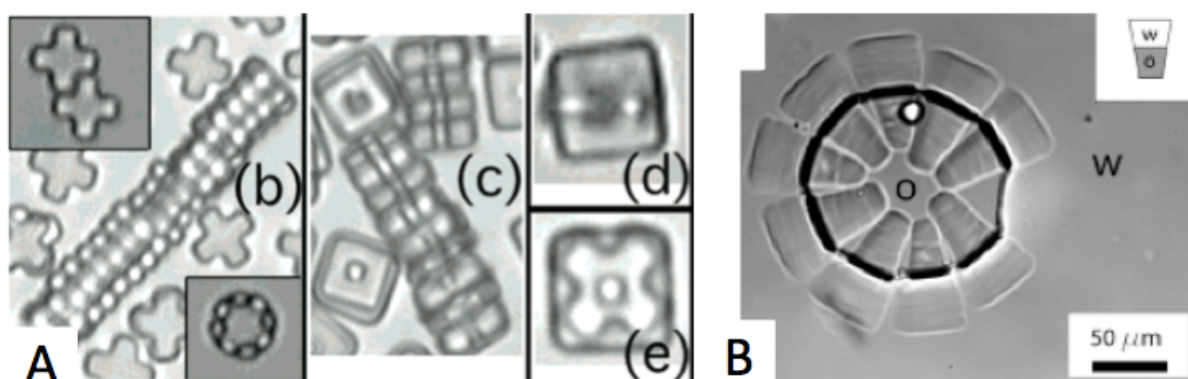
### **Chapter 1:**

#### **3.1 Alignment and Crystallization of Electrically Polarizable Anisotropic Particles Fabricated Using the PRINT Process**

##### **3.1.1 Introduction to the Alignment and Crystallization of Electrically Polarizable Anisotropic Particles**

The assembly of colloidal particles is a rich and growing area of materials science, with great potential for a broad range of applications including electronics, optics and biotechnology. Within this field, the bulk of research has been devoted to studying the assembly of isotropic spherical particles. In spite of this, there has been a growing interest in studying the assembly of anisotropic particles due to the more complex and useful structures that these particles can potentially assemble into.<sup>1, 2</sup> These novel structures are in great demand in the field of photonics where unique crystal symmetries, beyond hexagonally close-packed spheres, are desired. They can also impact the fields of optoelectronics, memory storage,<sup>2, 3</sup> and sensors, as well as providing the platform for new discoveries and phenomena. The fabrication of inorganic anisotropic particles is a heavily-researched field, and a wide range of nanoparticle shapes have been generated using established synthetic routes, including prisms, rods, highly branched particles, and tubes. As a result, the assembly of inorganic anisotropic particles has been studied to some degree.<sup>4-6</sup> There are far fewer reports on the assembly of anisotropic organic particles. This may, in part, be due to a lack of effective fabrication processes for the preparation of these particles with the monodispersity, control and range of compositions required for in-depth study. Of the

published studies, the shapes appear to be limited mainly to rod-like and disc-like particles.<sup>7-</sup>  
<sup>10</sup> There are only a couple of examples of assembling anisotropic organic particles with more exotic shapes. Hernandez and Mason<sup>11</sup> used depletion interactions to observe assemblies of their LithoParticles with cross and donut shapes (1-3  $\mu\text{m}$  in size). They observed columnar assemblies (Figure 3.1 A b & c), as well as lock-and-key aggregation (Figure 3.1 A d & e) of the crosses with the donuts (Figure 3.1 A). Doyle et al.<sup>12</sup> also investigated the assembly of relatively large (approximately 30-50  $\mu\text{m}$  in size) amphiphilic wedge-shaped polymeric particles, which assembled into micelles (Figure 3.1 B).



**Figure 3.1** Lithoparticles formed by automated stepper lithography (A)<sup>11</sup> were assembled via depletion interactions created by nanoemulsion droplets (not shown). Amphiphilic particles formed using Continuous Flow Lithography (CFL) system were assembled into micelles using a oil (o) in water (w) emulsion technique (B).<sup>12</sup>

### 3.1.1.1 Particle Fabrication Background

Both top-down and bottom-up approaches have been used to prepare anisotropic organic particles with varying degrees of success. Bottom-up approaches<sup>13-16</sup> have been used to synthesize anisotropic organic particles in a variety of shapes including discs, ellipsoids, “snowman-like”, and “confetti-like” particles. These processes are, however, sometimes complex and are generally limited in terms of shape, composition and dispersity. Top-down approaches, such as templating,<sup>8,9</sup> microfluidics<sup>12, 17-22</sup> and different lithography approaches<sup>7,</sup>

<sup>11, 23-25</sup> have the advantage of improved control over feature shape and size, and the possibility for more monodisperse particle synthesis, however these processes sometimes suffer from incompatibility with different reagents, limitations on the particle size and scalability. Previously, the nanomolding technique, Particle Replication in Non-wetting Templates (PRINT),<sup>26-31</sup> was reported to fabricate monodisperse, nanometer- and micron-sized particles of varying size, shape and composition, such as conical triacrylate nanoparticles and poly(ethylene glycol) arrows. This technique stands out because of the high degree of molding resolution, the broad range of chemistries that can be molded, and the ease with which reel-to-reel technology can be incorporated for scalability. Thus, it is ideally suited to the synthesis of unique, highly anisotropic particles in a wide range of compositions, and with particular utility in the rapidly growing nanomedicine field. PRINT can also be used in a straightforward manner to investigate the colloidal assemblies generated by such particles. The use of dielectrophoresis to study the assembly of highly anisotropic polymer particles fabricated with the PRINT process is reported in Section 3.1.

### **3.1.1.2 Dielectrophoresis**

Dielectrophoresis, the interaction of liquids or particles with nonuniform AC electric fields, has been shown to be a facile method for the assembly of colloidal suspensions.<sup>32-37</sup> The movement of particles is dependent on the local electric field, the dielectric properties of the particles and the suspending medium, frequency, surface charge density, concentration of free charges in the vicinity of the particle, geometry of the particle, and electrode geometry.<sup>32, 38, 39</sup> Typically, particles exhibit chaining phenomena in nonuniform AC electric fields. This process has been used to align particulates, such as carbon nanotubes, ceramic nanoparticles and glass fiber, in composites for improved mechanical or electrical



performance.<sup>40-43</sup> In these composite examples, the particles were generally highly polydisperse and comprised of random nonspecific shapes, so the assemblies were not well-structured. Most of the examples of the dielectrophoretic assembly of monodisperse colloidal systems have been with spherical particles, which generally crystallize into hexagonal close packed assemblies.<sup>2</sup> Some research has focused on the assembly of anisotropic rod-like particles via dielectrophoresis. This work has primarily focused on biological particles,<sup>39, 44-47</sup> such as cells, viral particles, and bacteria for the fabrication of biofilms and tissue or in diagnostics and separation. Both experimental and theoretical studies have indicated that ellipsoidal particles exhibit more complex behavior in nonuniform electric fields, because there are more degrees of freedom from the typical isotropic case of the sphere.<sup>48</sup> In fact, there is a preferred or more stable orientation for these shapes, where they align with their long axis parallel to the axis of the electric field.<sup>47-49</sup> Here, the effect of particle shape on the behavior of anisotropic polymer particles in nonuniform AC electric fields is explored.

### **3.1.2 Experimental**

#### **3.1.2.1 Particle Composition**

The following reagents were purchased through Sigma Aldrich and used as received: 2,2-diethoxyacetophenone (DEAP) (95%, Aldrich), 2-aminoethyl methacrylate hydrochloride (AEM) (90% Aldrich), fluorescein o-acrylate (97% Aldrich), dimethyl sulfoxide (DMSO) ( $\geq 99.9\%$  Aldrich), hexadecyltrimethylammonium bromide (CTAB) (Aldrich). Trimethylolpropane ethoxylate (14/3 EO/OH) triacrylate (MW 912 g/mol Aldrich) was de-inhibited using adsorption alumina (Fisher). 1-vinyl-2-pyrrolidinone (VP) (Aldrich) was distilled prior to use. 2-propanol (histological, Fisher) and acetone

(histological, Fisher) were both filtered with a 0.2  $\mu\text{m}$  nylon filter (Millipore) prior to use. Cyanoacrylate adhesive (Zap CA PT-08, Pacer Technologies) was used as received. The perfluoropolyether (PFPE) prepolymer resin (Fluorocur<sup>TM</sup>, Liquidia Technologies, Inc.) was thoroughly mixed with 0.1% (w/v) DEAP photoinitiator before use. Double-sided adhesive slide separators (SS1X9, Grace BioLabs) were used with standard 1x3" glass slides (Fisher Scientific) for preparation of the dielectrophoresis (DEP) cell. The untreated side of poly(ethylene terephthalate) (PET) sheets (Melinex 453, DuPont) was used for mold support and for monomer distribution and removal.

#### **3.1.2.2 Master Fabrication**

Silicon wafers were patterned for use as master templates using methods described in Section 1.

#### **3.1.2.3 Mold Fabrication**

Initially, a silicon wafer, patterned with one of the four shapes (boomerang, disc, hexnut, or rod) was placed in a leveled UV-curing chamber. A 5-10 mL aliquot of PFPE prepolymer was deposited on the surface of the wafer and allowed to spread until it reached the edges. The chamber was then purged under low flow nitrogen to remove oxygen from the chamber without disturbing the exposed surface of PFPE. After which, the uncured mold was exposed to UV light ( $\lambda_{\text{max}} = 365 \text{ nm}$ ,  $P \geq 20 \text{ mW/cm}^2$ ) for an additional 3 minutes. Molds were gently peeled off the master then placed feature side up on a clean sheet of PET for ease of handling.

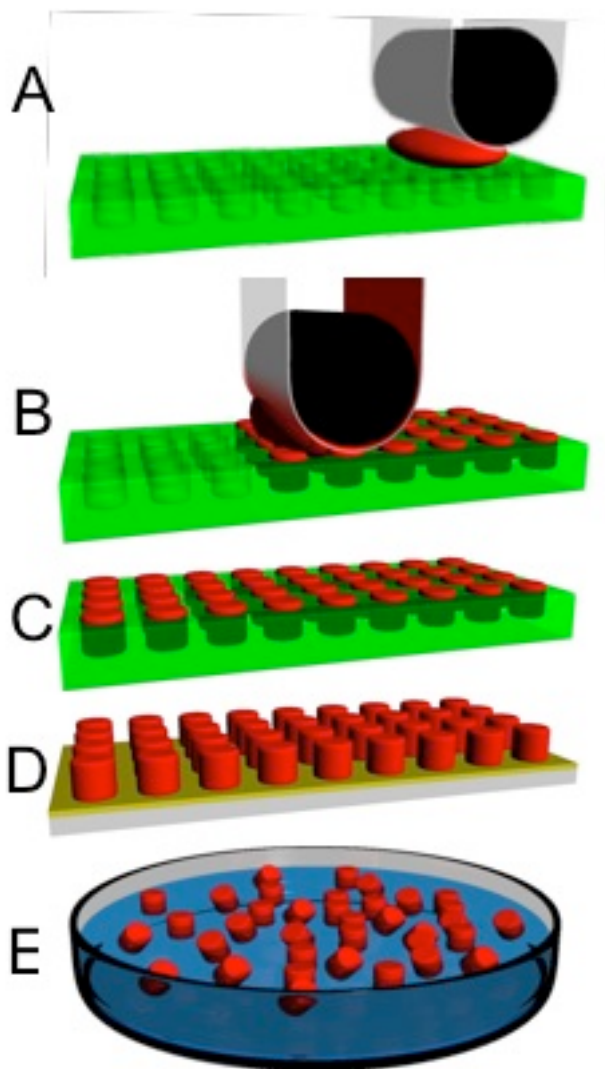
#### **3.1.2.4 Monomer Solution**

The first design parameter of the particles was to create a cross-linked architecture that was highly miscible with the other functional monomers and had minimal swelling in

aqueous environments. Trimethylolpropane ethoxylate triacrylate was ideal for this role because of the amphiphilic nature of the ethylene oxide repeat unit and its high functionality. Next, a small amount of fluorescent monomer, fluorescein o-acrylate, was incorporated into the hydrogel matrix to facilitate optical analysis. AEM was then added to the monomer mixture to impart amine functionality that will be used for particle functionalization in future projects. Finally, the DEAP photoinitiator was used because it was easy to handle (liquid at room temperature), highly miscible with the three monomers, and, in comparison to thermal initiators, facilitated rapid and convenient polymerization conditions that were compatible with the PRINT process. Monomer solution was prepared as follows: First, 20 mg fluorescein o-acrylate and 30 mg AEM were dissolved in 100  $\mu$ L DMSO. Next, 940 mg de-inhibited trimethylolpropane ethoxylate (14/3 EO/OH) triacrylate was added to the solution and mixed thoroughly by vortexing for 2-3 minutes until the solution was optically transparent. Finally, 10 mg DEAP was added and the solution was again vortexed until optically transparent.

### **3.1.2.5 Particle Fabrication**

A small aliquot (20-30  $\mu$ L) of the monomer solution was deposited on the surface of the PFPE mold where it met with the PET sheet. Using an in-house single-roll laminator, the monomer was evenly distributed over the surface of the mold. Excess monomer solution, visible as small beads on the PFPE surface, were wicked away using a clean sheet of PET on another heated (80 °C) laminator. The filled mold was then placed back in the UV-curing chamber where it was again purged for three minutes with dry nitrogen and subsequently exposed to UV-light for an additional 3 minutes under continued purge. See Figure 3.2 for a schematic representation of the PRINT process.



**Figure 3.2.** Schematic representation of the PRINT process. A) Empty mold (green), high surface energy polymer sheet (clear), roller (black); roller is brought into contact with the pre-particle solution and the mold; B) Roller evenly distributes pre-particle solution into cavities of mold. Excess pre-particle solution is wicked away by the high surface energy polymer sheet; C) Particles are cured in the mold; D) Particles are removed from the mold; E) Particles are collected in solution.

### 3.1.2.6 Particle Harvesting

The filled mold was hand laminated over small aliquot (100  $\mu$ L) of poly(cyanoacrylate) on a glass slide and allowed to set for 20-30 minutes. The mold was then peeled back from the glass slide leaving an array of particles firmly bound to slide by

the poly(cyanoacrylate). The particles were then rinsed with filtered acetone to remove them from the glass slides and collected in 50 mL falcon tubes for further purification.

#### **3.1.2.7 Particle Purification**

After harvesting, particles were purified to remove residual cyanoacrylate and other unwanted debris through a process of repeated rinsing with acetone. Initially, particles were pelleted out of solution by centrifugation (5 minutes, 137 G). The supernatant was then decanted and the particles were resuspended by vortexing gently for 1 minute. This process was repeated at least 5 times. Particles were then gravimetrically filtered to remove any debris. Finally a 100  $\mu$ L aliquot of the particle slurry in acetone was placed in a preweighed eppendorf tube and was dried *in vacuo* to determine the concentration of particles.

#### **3.1.2.8 Sample Preparation**

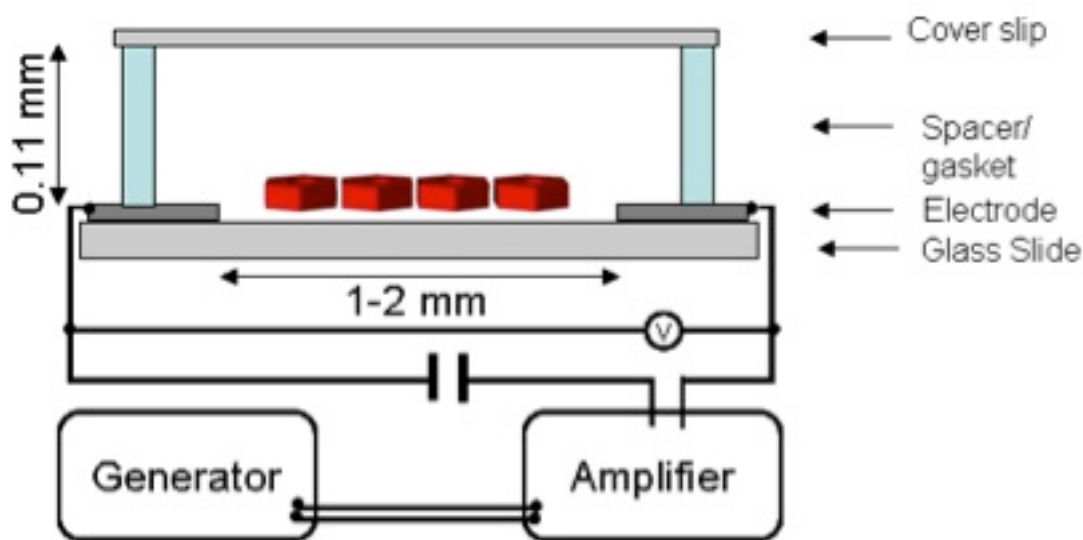
In order to avoid particle aggregation, particles were never completely dried. Instead, particle samples were prepared by combining 1.0% (w/v) aqueous CTAB solutions with particle/acetone slurries. The solutions were then placed under vacuum to remove the excess acetone. Final particle concentrations were as follows: hexnuts were 5 mg/mL, rods were 10 mg/mL, discs were 20 mg/mL, and the boomerangs were 10 mg/mL. For DEP experiments, aliquots of 11 mL were placed in the sample cell. Sample pH was between 5.5-6.5. No buffer was added.

### **3.1.3 Experimental Setup**

#### **3.1.3.1 Electrical Cell Setup**

The electrodes were fabricated following various procedures described elsewhere.<sup>36, 50, 51</sup> Briefly, glass slides fit with a 1-2 mm wide adhesive mask were coated with 70-90 nm Pd/Au allow using a sputter coater (Model 108 Auto Sputter Coater, Cressington Scientific

Instruments) to form two planar electrodes. An adhesive gasket was placed over the electrodes. A 10-11  $\mu\text{L}$  aliquot of colloidal particle solution was placed on the surface of the slide and was sealed in place using a cover slip (1.5 Gold Seal). The alternating electric field was produced by a wave function generator (Model 180 Function Generator, Wavetek) and then amplified (6824A DC Power Supply Amplifier, Hewlett Packard). Field intensities ranged from 10-50 V with square wave frequencies between 500-5000 Hz. Experiments were typically run at 40 – 50 V and 500 Hz (see Figure 3.3).



**Figure 3.3** Dielectrophoretic cell schematic. Particles, shown in red are placed in a cell with two electrodes. An alternating potential is applied across the cell creating a dipole moment in the particles that causes them to align.

### 3.1.3.2 Imaging

Individual particles were imaged using a Hitachi S-4700 scanning electron microscope. The samples were dried from acetone slurry at room temperature in air and then coated with Pd/Au (3-5 nm) in the sputter coater. Particle alignment, packing, and crystallization were observed using a Zeiss Axioskop 2 MAT incident light microscope fitted with an AxioCam MRm digital camera. Movies of particle alignment were captured using

Axiovision software. Movie frames were captured roughly every second for a minute (hexnuts, discs, and boomerangs) and five minutes (rods).

### 3.1.3.3 Turbidity Experiments

Particle samples (5-20 mg/mL) were prepared in 0.2, 1.0, and 5.0% (w/v) aqueous CTAB solution. A cuvette (100  $\mu$ L, QS), with a path length of 1 cm, containing the particle sample was then vortexed and placed in a plate reader (Spectra Max M5, Molecular Devices). A kinetic experiment was performed at  $\lambda = 490$  nm, reading absorbance every 30 s for 1 hour at 22  $^{\circ}$ C. All experiments were repeated three times to establish reproducibility. The turbidity,  $\tau$ , defined as the attenuation of the light beam by scattering when passing through a sample, was determined from equation 3.1 below, where  $I_o$  is the incident intensity of light,  $I_t$  the transmitted intensity, and  $l$  the optical path length.

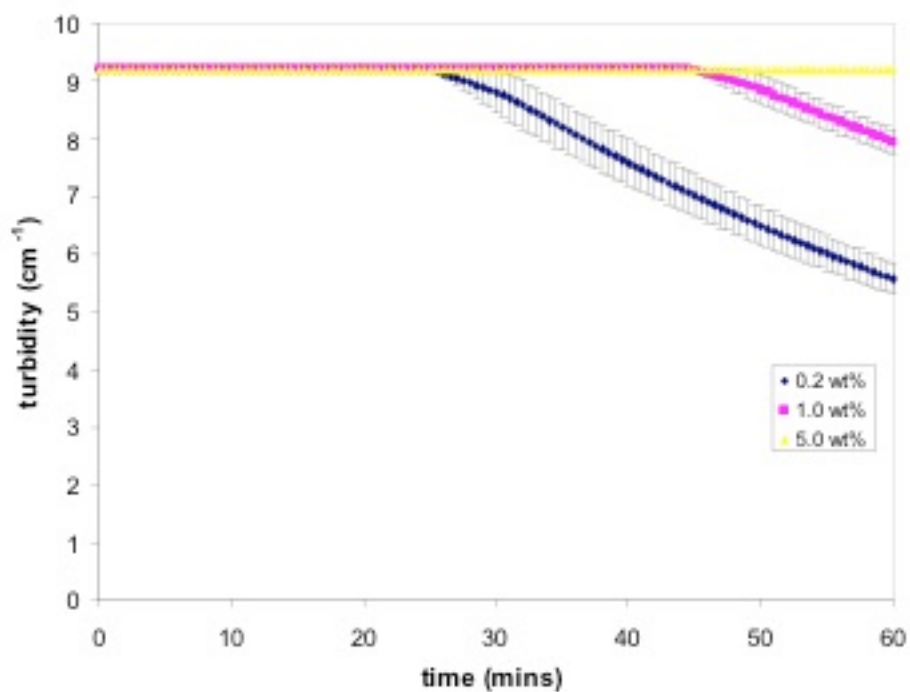
$$\tau = l^I \ln(I_o/I_t) \quad (\text{Eqn. 3.1})$$

### 3.1.4 Results and Discussion

#### 3.1.4.1 Particle Stability

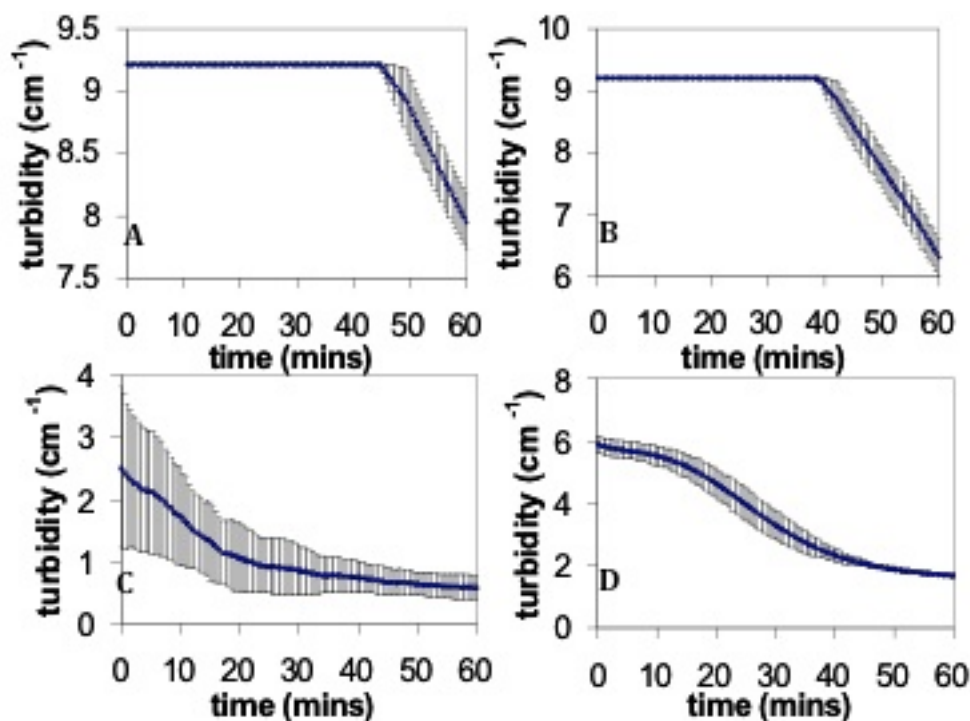
In colloidal systems, unless strategies are employed to stabilize the particles either electrostatically or sterically, there is a tendency for particles to aggregate due to attractive van der Waals forces. This was observed when the particles were suspended in water, as they aggregated rapidly in the absence of stabilizer. In order to hinder aggregation, increasing amounts of CTAB were added to the particle suspension. Generally, as CTAB concentration increased, particle stability increased (Figure 3.4). In this manner, it was possible to determine conditions for colloidal stability within the timeframe of the dielectrophoretic experiments. Turbidity experiments showed that 1.0% (w/v) CTAB was

adequate to slow particle aggregation and sedimentation of all the particle sizes studied sufficiently for our purposes (~5-10 minutes) (Figure 3.5).



**Figure 3.4** Turbidity measurements on 5 mg/mL hexnut suspensions at three CTAB concentrations: 0.2 wt%, 1.0 wt% and 5.0 wt%.





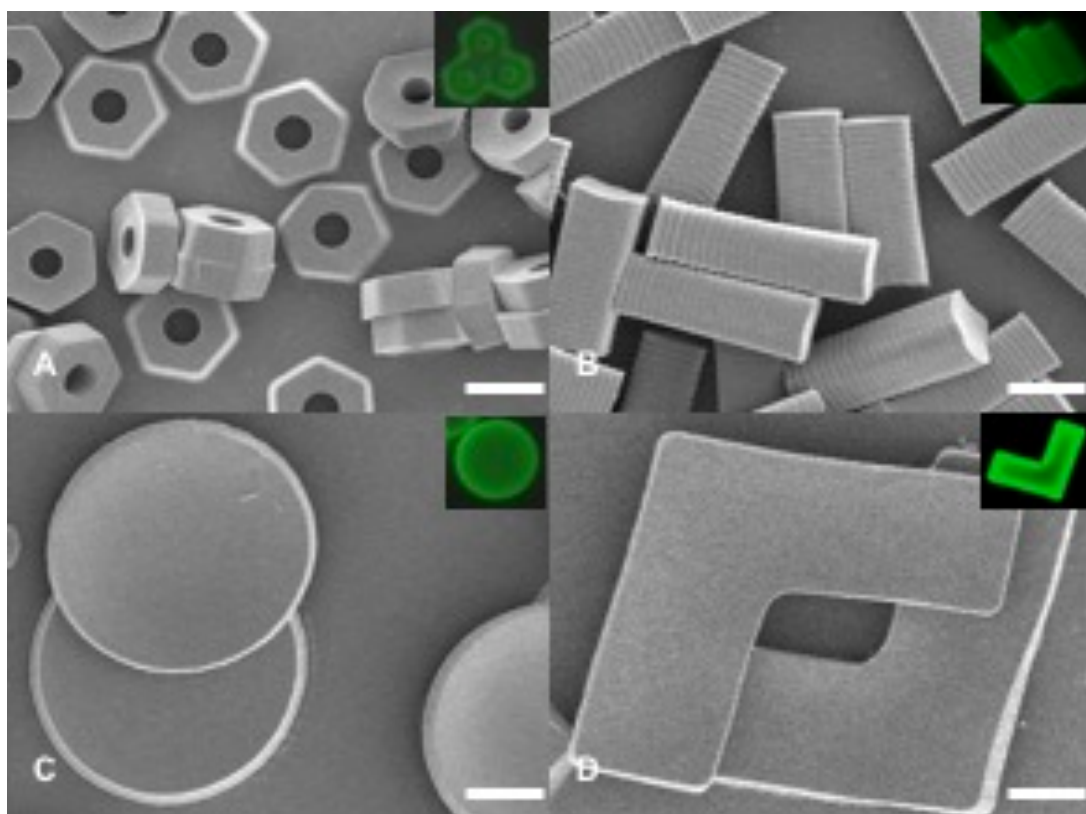
**Figure 3.5** Turbidity curves for aqueous particle suspensions containing 1.0 wt% CTAB where A) 5 mg/mL hexnut suspension, B) 10 mg/mL rod suspension, C) 20 mg/mL disc suspension, and D) 10 mg/mL boomerang suspension.

Observation by fluorescence microscopy revealed individually suspended particles, however, a small number of aggregates were observed in solution. These aggregates could be caused by depletion interactions. In these aggregates, the rods, hexnuts, and discs packed with their major axes parallel to one another. These aggregates typically settled out of solution much faster than individual particles. The trimethylolpropane ethoxylate triacrylate polymer used to synthesize the particles is denser than water with an estimated specific gravity of 1.2-1.3 at 25 °C, and, in general, the sedimentation rate for the particles depended on their size and shape: 40-50 minutes for the rods and hexnuts, 10-30 minutes for the boomerangs and discs. In addition, the limited mobility of the aggregates affected their response to the applied AC field; this was especially prevalent for the larger particles.

However, because the number of aggregates was small in comparison to the number of free particles we chose to focus on the free particles.


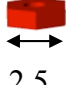
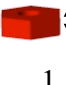



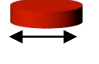



#### **3.1.4.2 Particle Fabrication Results**

The resulting PRINT particles were uniform in size and shape and were relatively stable in aqueous solution containing CTAB. The tops of the particles were flat while the bottoms of the particles were slightly concave due to a meniscus that was formed during the mold filling process. Scanning electron microscopy (SEM) images of the particles are shown in Figure 3.6 with corresponding optical fluorescence images. Particle sizes were calculated using PCI software with SEM images. The sizes obtained by SEM were slightly smaller ( $< 5\%$ ) than the sizes of the mold. This is a result of the cosolvent removal during the washing and drying process prior to imaging by SEM. Particle surface area and volume were calculated using these values (Table 3.1).



**Figure 3.6** Representative scanning electron micrograph and fluorescent images of A.)  $2.5 \times 1 \mu\text{m}$  hexnut particles with  $1 \mu\text{m}$  hole, B.)  $1.6 \times 1.6 \times 5 \mu\text{m}$  trapezoidal particles, C.)  $6.5 \times 0.8 \mu\text{m}$  disc-shaped particles, D.)  $9.6 \times 3.4 \times 1 \mu\text{m}$  boomerang-shaped particles with  $2 \mu\text{m}$  scale bar.

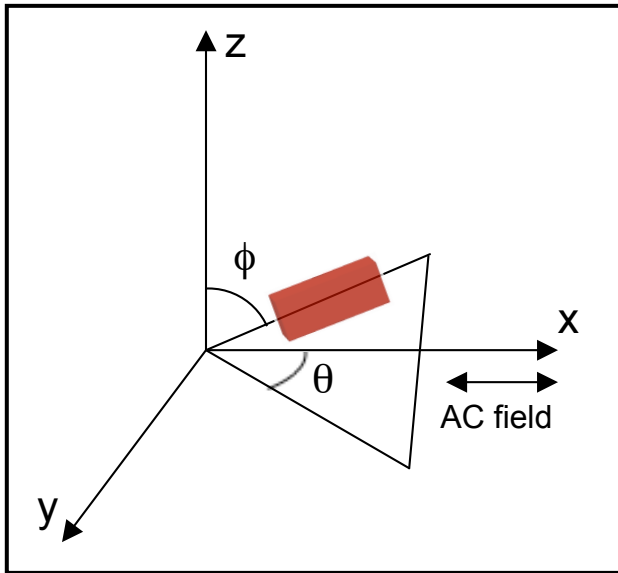
**Table 3.1** Particle dimensions and critical aggregation values.

Particle	Primary Axis ( $\mu\text{m}$ )	Secondary Axis ( $\mu\text{m}$ )	Tertiary Axis ( $\mu\text{m}$ )	Surface Area ( $\mu\text{m}^2$ )	Volume ( $\mu\text{m}^3$ )	SA:Vol	Aggregation Threshold (minutes)
Hexnut	 2.9	 2.5	 1	21	4.6	4.56	44.5
Rod	 5	 1.6	 1.6	37.1	12.8	2.89	39
Disc	 6.1	 1	-	82.7	26.5	3.12	-
Boomerang	 -	 1	-	146	53.7	2.71	9

### 3.1.4.3 Particle Alignment and Crystallization Experimental Results

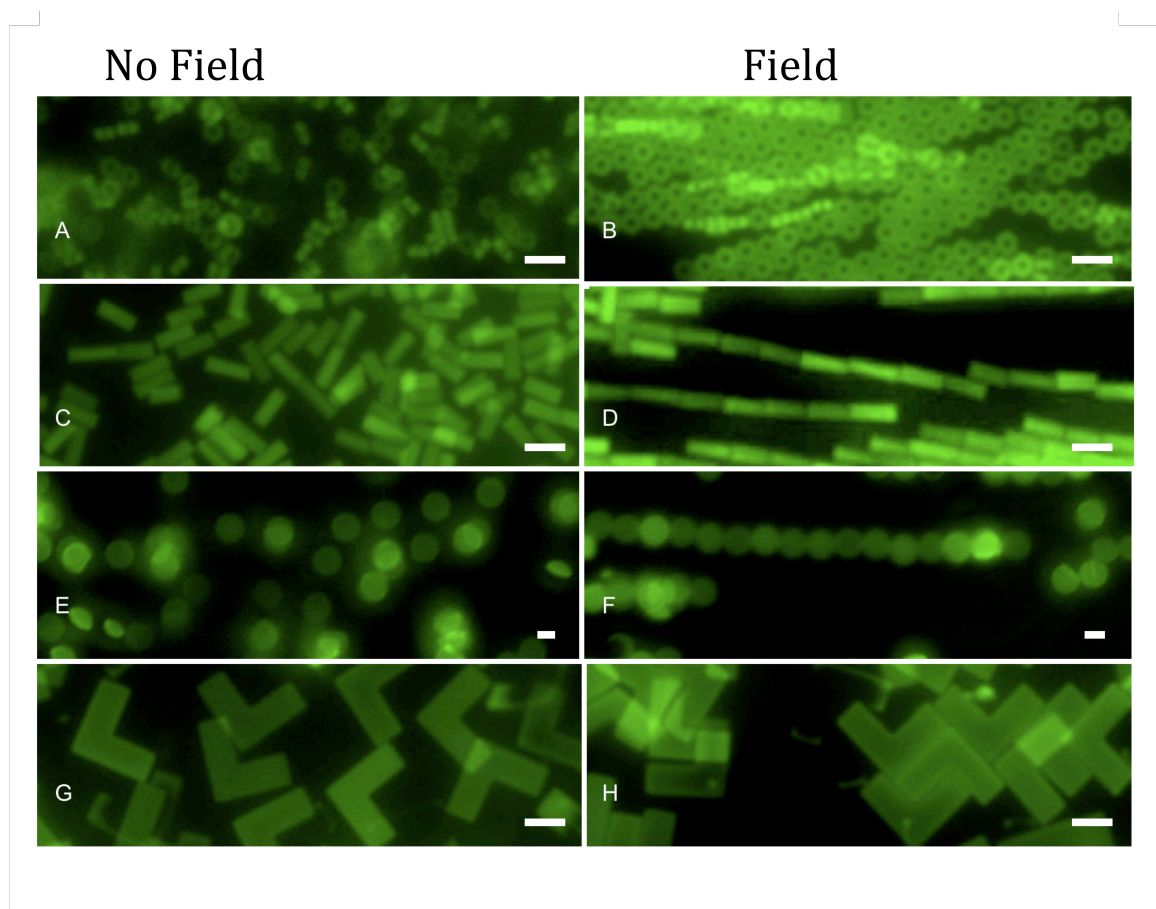
Dielectrophoretic alignment of particles in solution occurred when a nonuniform AC field was applied across two planar electrodes (Figure 3.3). As expected for positive dielectrophoresis, when the field is turned on, the particles become polarized and are directed towards the region with the highest field intensity – the glass region between the electrodes. During this step, particles experience a torque and are observed to reorient to a new stable position from their initial random orientation relative to the field. This electroorientation results in the alignment of particles with their longest axis parallel to the applied field ( $\theta = 0^\circ$ ), consistent with observations made by others.<sup>47, 48</sup> Additionally, in the majority of cases, the particles' second major axis (if there was one) was perpendicular to the normal of the plane of the electrode ( $\phi = 90^\circ$ ), or in other words, the particles laid flat on the surface of the glass electrode (Figure 3.7). Once the particles aligned with the field, they began to link

together forming chains. This phenomenon is thought to be due to the interactions between the dipoles induced in the particles.<sup>37</sup> Chains formed rapidly (10-20 seconds) and continued to grow as long as the field was left on. The speed of chaining appeared to be a function of the size of the particle with the smaller particles (hexnuts and rods) forming chains the fastest while the discs formed chains much slower and the boomerangs formed no discernable chains. Large chains of particles then moved slowly towards each other and formed large crystalline structures. If the AC field was removed after being applied for only a short period (10-20 seconds), particles returned to a random state. However, if the field was applied for a longer period of time, aggregation and sedimentation of the particles began to take place. This trapped some particles in permanent chains while bound to the surface of the glass cell. The alignment, chaining, and packing properties of each particle shape is described in greater detail below.



**Figure 3.7** Particle orientation in the electric field:  $\theta$  is the angle between the major axis of the particle and the AC field, and  $\phi$  is the angle between the major axis of the particle and the normal of the plane of the electrode.

Hexnut shaped particles, the smallest of the four particles shapes, aligned rapidly with the applied field. The principle axis of the hexnut particle was  $2.9\text{ }\mu\text{m}$  from point-to-point (Table 3.1). The particles initially formed chains in this fashion (Figure 3.8 A-B). It was interesting to observe that the majority of hexnut chaining took on a slightly different conformation with the flat edges of the particles touching one another rather than just the tips, thus the second axis of the hexnuts ( $2.5\text{ }\mu\text{m}$ ) was found to be aligned parallel to the applied field. This effect is most likely driven by the need to maximize surface interactions. That is, it is more energetically favorable for the chains to undergo a slight modification from the most dielectrophoretically stable conformation to one that is slightly less favorable because of the stability gained from the dramatic increase in surface interactions. Chains of hexnuts had two orientations. The primary orientation, shown in Figure 3.9 A, was with the particles parallel to the AC field ( $\theta = 0^\circ$  for secondary axis) and perpendicular to the normal of the electrode plane ( $\phi = 90^\circ$ ). The second, and less common orientation was with particle chains parallel to the AC field and parallel to the normal of the electrode ( $\phi = 0^\circ$ ). While this chain orientation was regularly observed, the chains typically collapsed back into the plane of the electrode. Over time, chains of hexnut particles moved towards each other and came into contact. This process eventually formed large crystals of particles in a hexagonal close-packed pattern.



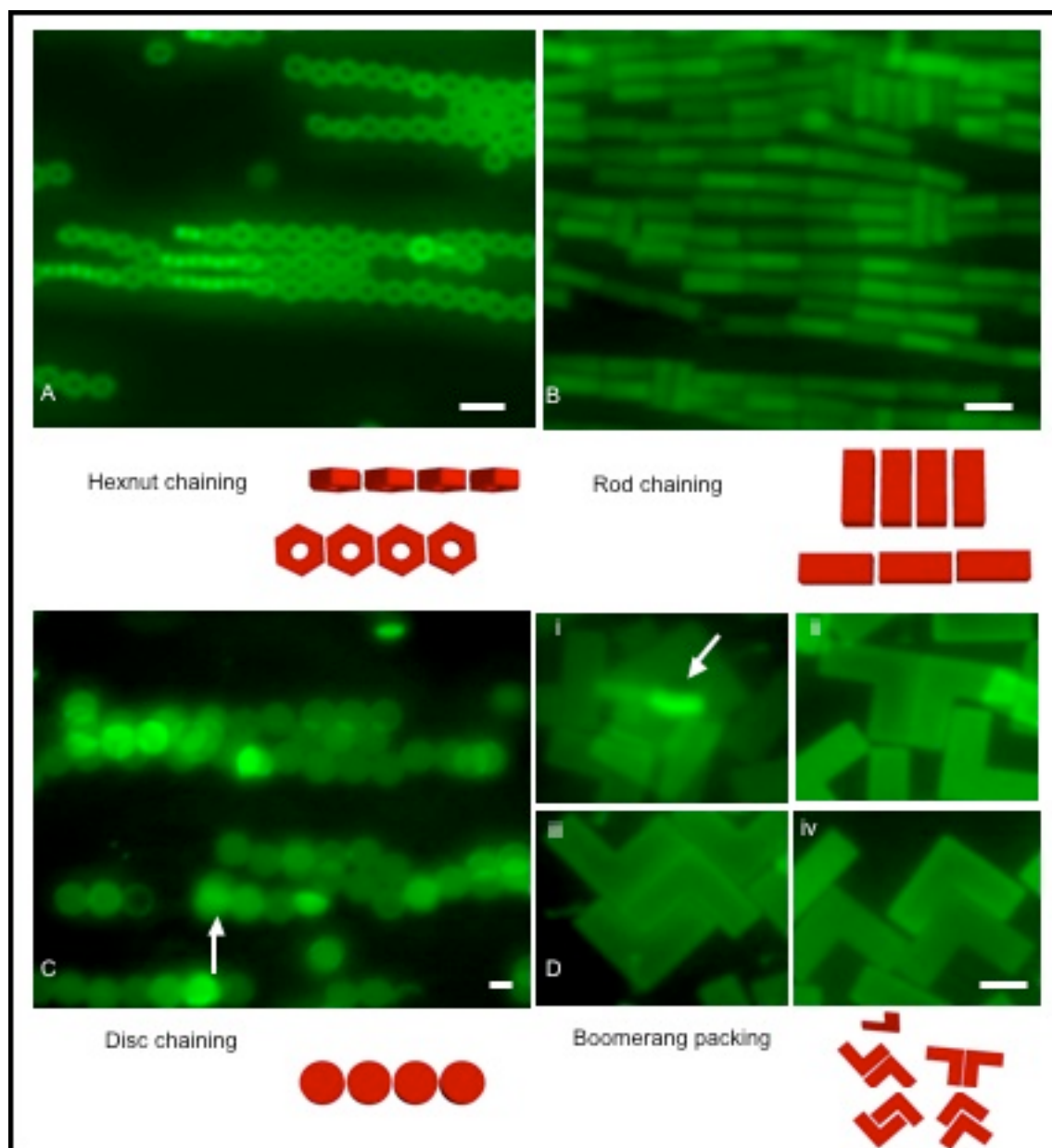
**Figure 3.8** Representative fluorescence images of randomly dispersed A, C, E, G, and electrically aligned B, D, F, H particles with a 5  $\mu\text{m}$  scale bar.

Rod shaped particles, like the hexnut particles, responded rapidly to the dielectrophoretic force and aligned with their primary axis parallel to the AC field (Table 3.1). As particles began to move through solution, some particles ( $9\% \pm 1\%$ ) were trapped perpendicular to the AC field ( $\theta = 90^\circ$ ,  $\phi = 90^\circ$ ). Very few particles were observed with the long axis parallel to the normal of the electrode plane. Long chains of the rods formed almost immediately parallel to the AC field (Figure 3.8 C-D). As with the hexnuts, the chains of rods came together to form crystals. Unlike the hexnuts, the rods formed a rectangular lattice (Figure 3.9 B). It is interesting to note that in the absence of any defects (perpendicular particles) individual particles within adjacent chains came into registry with

one another in a smectic-like manner. We believe this effect may be driven by the areas of high field intensity at the corners of the particles.

The disc shaped particles rapidly settled out of solution and sat with their face flat on the glass surface in the absence of an AC field. Once settled, the particles became difficult to move even at higher voltages. The circular nature of the disc shaped particles gives them only one major axis (Table 3.1). This is different from the particles mentioned above which both have at least two major axes that aligned with the applied field. Alignment of the disc shaped particles manifested itself with the particles laying flat on the surface of the glass ( $\theta = 0^\circ$ ,  $\phi = 90^\circ$ ). In comparison to the smaller particles the discs slowly (30-60 seconds) formed short chains (Figure 3.8 E-F). The chains had trouble moving and therefore crystallization was only observed a few times. The crystals that formed were hexagonal close-packed in nature (Figure 3.9 C).



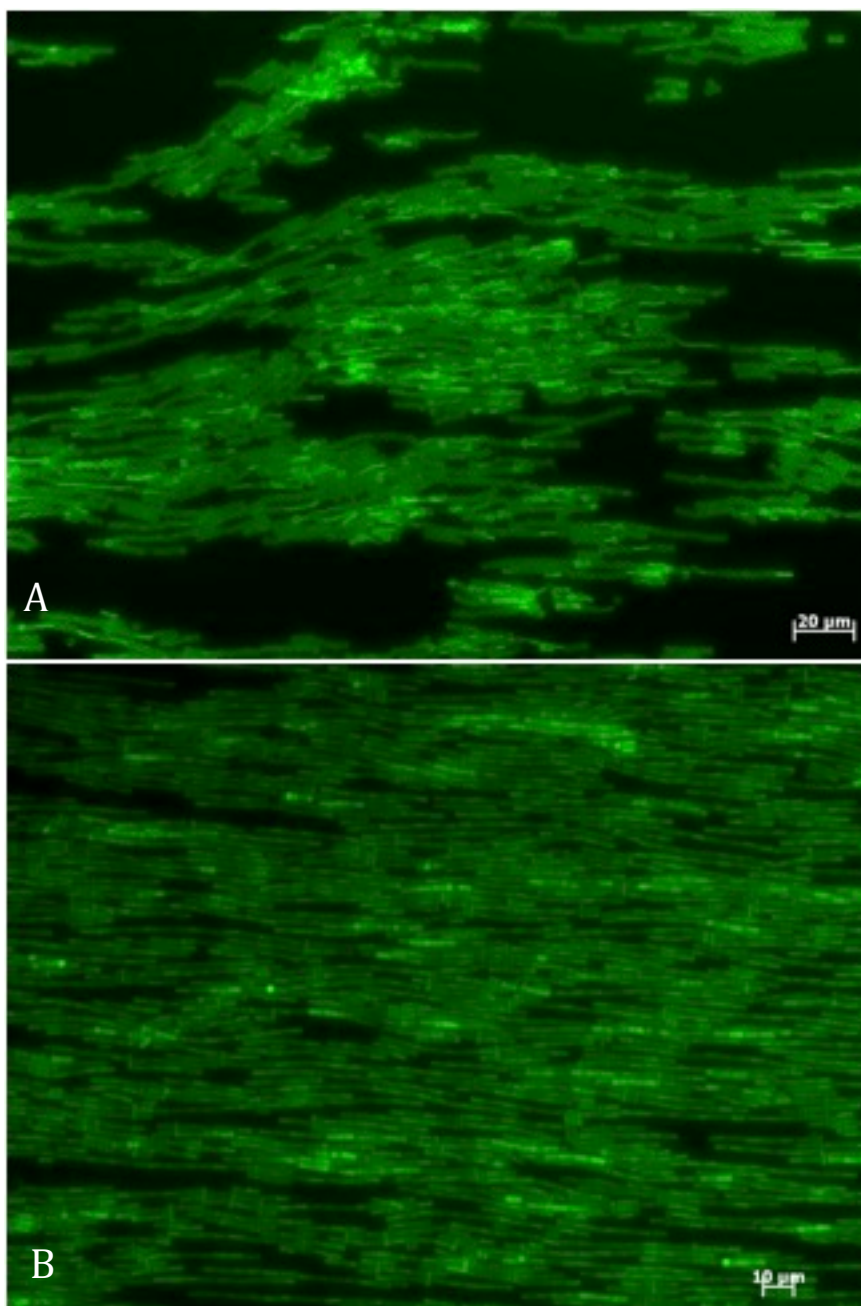


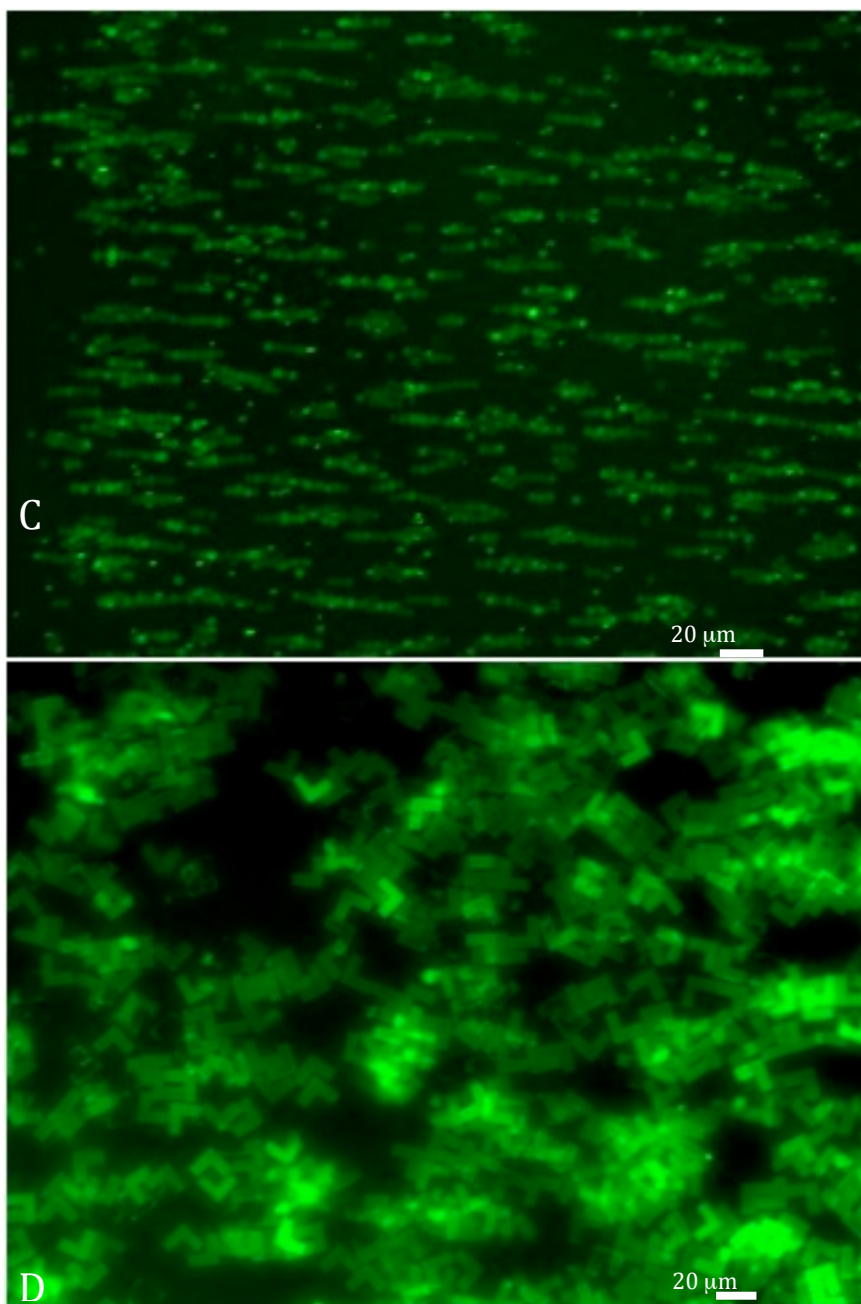
**Figure 3.9** Fluorescence images of aligned particles with applied AC electric field. 5 μm scale bar.

Boomerang shaped particles exhibited unique behavior in comparison to the other particle shapes. Similar to the other shapes, boomerangs typically laid flat in the plane of the electrode ( $\phi = 90^\circ$ ). But unlike the other shapes, the boomerangs had no preferential orientation with respect to  $\theta$ , which may be due to the symmetry in the particle shape (Table

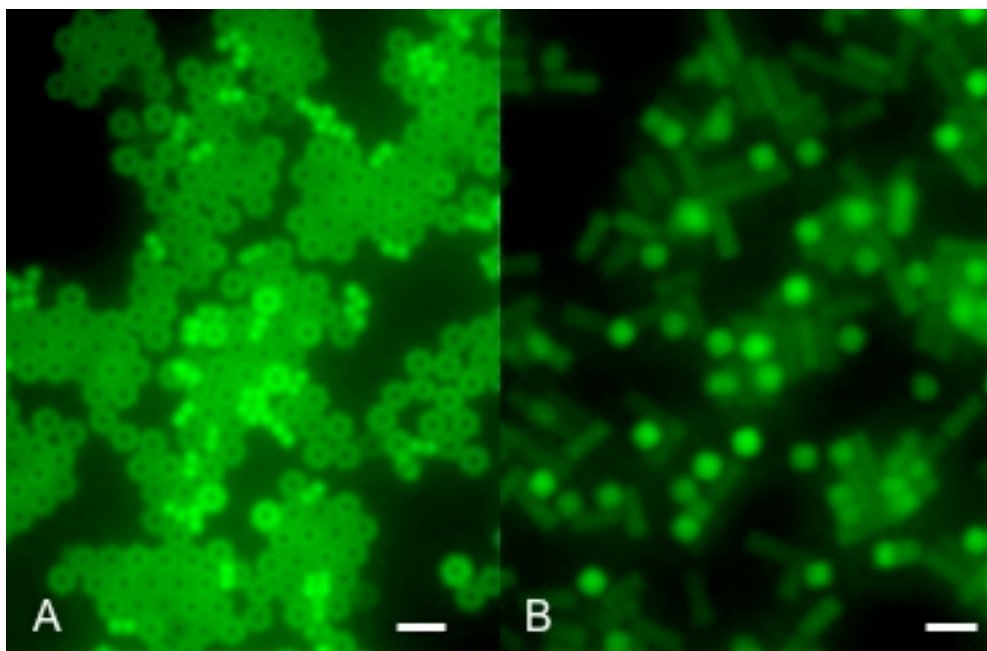
3.1). Interestingly, the few boomerangs that did stand straight up aligned with the applied AC field ( $\theta = 0^\circ$ ,  $\phi = 45^\circ$ ). These particles eventually tipped and fell back into the plane of the electrode ( $\phi = 90^\circ$ ). Although the boomerangs did not align in the presence of an applied AC field, they did adopt a number of interesting orientations in clusters (Figure 3.9 D i-iv). These clusters eventually grew large enough that some directionality was observed in which the clusters were aligned with the applied field. Rapid sedimentation coupled with the unique shape of the particles prevented large-scale crystallization.

While the studies have focused primarily on crystallization of particles between the electrodes (see Figure 3.10 A-D for low magnification images of particle alignment), crystallization on the electrodes was also observed. This type of crystallization was only observed for the hexnut shaped particles. These particles formed small hexagonal close-packed clusters that laid flat on the electrode surface. A large portion of the individual hexnut particles found on the electrode were oriented perpendicular to the surface of the electrode but had no significant preference for orientation otherwise. The rod and disc shaped particles did not form crystals but did orient themselves perpendicular to the plane of the electrode. Boomerang shaped particles did not exhibit any preferential alignment or crystallization on the electrode (Figure 3.11 A-B).





**Figure 3.10** Low magnification fluorescence images of particle alignment in nonuniform AC electric field for (A) hexnut, (B) rod, (C) disc, and (D) boomerang shaped particle suspensions.



**Figure 3.11** Fluorescence images of hexnut (A) and rod shaped (B) particles with applied AC electrical field on the electrode. 5  $\mu\text{m}$  scale bar.

#### 3.1.4.4 Dielectrophoresis Summary

The ability to design and fabricate new particle shapes with tailored chemistries expands the possibilities for observing and characterizing novel particle assemblies, and for the design and synthesis of advanced composite materials with interesting nanostructures. We have introduced new organic particle geometries to the study of colloidal assemblies, and have demonstrated that these new shapes can influence interesting packing and crystallization behavior. With the exception of the boomerang shaped particles, all particle shapes studied exhibited chaining behavior in the presence of the nonuniform AC electric field. Moreover, our results are consistent with others, as the anisotropic particles preferentially align with their longest axes parallel to the field. We observed different crystal structures when the chains assembled: hexagonal close packed for the hexnuts and discs, and rectangular for the rods. Interestingly, even though the boomerangs did not align in chains in the field, regions of unique packing were observed. Unfortunately, this particular series of

sizes and shapes did not enable us to make systematic quantitative comparisons between the various particle shapes with regard to their response times and relaxation times. These properties will be examined in the near future.

## **Section 3:**

### **Chapter 2:**

## **3.2 Fabrication and Magnetic Manipulation of Shape and Size Specific Magneto-Polymer Composite Particles**

### **3.2.1 Introduction and motivation for the Fabrication of Magneto-Polymer Composite Particles**

The relentless drive towards processes that can fabricate uniform, multifunctional colloidal particles has been strongly influenced by increasingly complex applications in both life and materials sciences. One approach to enhancing the properties of colloidal particles is through the use of nanocomposites, such as the incorporation of inorganic nanoparticles into a polymer colloidal particle. In this way, properties specific to the inorganic component are conferred to the composite particle thereby imparting desirable properties to the particle. Magnetic nanoparticles are one such filler particle of great interest, and they are integral to numerous biological and electronic processes. For example, magnetic particles have been used in different bioseparation techniques, for magnetically-induced hyperthermia of malignant tumors, as contrast enhancement agents for magnetic resonance imaging (MRI), and in tissue repair.<sup>52, 53</sup> Magnetic particles can also play a role in the delivery of biologics, especially drugs<sup>54-56</sup> and nucleic acids (magnetofection)<sup>57-59</sup>, as they can be manipulated via external fields to improve transport in biological systems. In the materials science field, the directed assembly or the self-assembly of magnetic particles has been found to be exceedingly useful in the fabrication of photonic crystals<sup>60-62</sup> and as nanowire contacts in electronic devices.<sup>63, 64</sup> They are also used as device components in microfluidics.<sup>65-67</sup>

Additionally, there has been growing interest in the use of magnetic particles in the fabrication of nanomotors and nanomachines.<sup>68-71</sup>

With the host of applications requiring tailored magnetic particles, and the even greater number of potential applications that have yet to be realized, synthetic processes that can generate particles with specific features that result in some set of desired functionality and properties are in demand. Magneto-polymer nanocomposite particles have been synthesized via various bottom-up methods, typically with spherical geometry. The composite particles can have a random internal structure, a core-shell structure,<sup>72</sup> an aligned chain structure<sup>61</sup>, or the composite particles can be Janus particles, with the magnetic nanoparticles concentrated on one side.<sup>73-76</sup> The alignment of the magnetic nanoparticles within the composite particle plays an important role in the overall magnetic properties, and thus the behavior of such particles in the presence of an external magnetic field. For example, Dyab *et al.*<sup>73</sup> showed that aligning and concentrating magnetite nanoparticles in their microparticles resulted in a change from superparamagnetic behavior of the nanoparticles to ferromagnetic behavior of the composite microparticles; furthermore, for janus microparticles, the colloidal materials, exhibited zigzag chaining in an external magnetic field. Shape control, beyond spheres, is very difficult with bottom-up approaches, and there are very few examples of uniform non-spherical composite particles synthesized via these routes.<sup>74, 77, 78</sup> One morphology of particular interest to the drug delivery community is the wormlike particle shape.<sup>77-79</sup> This structure is accessible via block copolymer micelle morphologies<sup>78</sup> and aggregation strategies,<sup>77</sup> though with these approaches there is a broad distribution in final composite particle size.



There are even fewer examples of magneto-polymer nanocomposite particles fabricated via top-down methods, and these have been mainly in microfluidic devices.<sup>28-31</sup> Two main advantages of top-down approaches are uniformity and shape control. It is possible to fabricate anisotropically-shaped nanocomposite particles in microfluidic devices, such as disks, plugs and torroids,<sup>80, 81</sup> in addition to spheres. The nanocomposite particles can have a uniform distribution of the magnetic nanoparticles. Hwang *et al.*<sup>80</sup> studied the effect of shape on the alignment of magneto-polymer composite particles with the magnetic nanoparticles uniformly distributed. They found that unlike the spheres, disks and plugs exhibited a directional preference to an external magnetic field arising from their shape asymmetry. Microfluidic devices can also be used to fabricate composite particles with anisotropically distributed magnetic nanoparticles.<sup>82</sup>

This chapter details the fabrication of well-defined, shape-specific magneto-polymer nanocomposite particles using the top-down imprint lithography approach, Particle Replication in Nonwetting Templates (PRINT<sup>®</sup>). The PRINT process has proved to be a versatile, scalable particle fabrication platform with exceptional tunability of particle characteristics – size, shape, modulus, composition, cargo, surface functionalization and chemical anisotropy.<sup>83</sup> This chapter builds upon early work<sup>84</sup> by incorporating superparamagnetic magnetite nanoparticles into PRINT polymer particles resulting in unique magneto-polymer composite particles in a range of shapes and sizes, from nanoworms to micron-sized boomerangs. One important feature of the fabrication process is the ability to manipulate the magnetic cargo within the particle matrix prior to its polymerization. In this way, the magnetite nanoparticle chains can be permanently aligned in different directions relative to the composite particle axis, which affects particle motion in response to external

magnetic fields. Additionally, it is demonstrated that the PRINT magneto-polymer particles can be engineered to be steerable micromotors, via the anisotropic surface functionalization of platinum. In the presence of the fuel, hydrogen peroxide ( $\text{H}_2\text{O}_2$ ), chemical locomotion is achieved<sup>85</sup> and the encapsulated magnetite then provides a means of remotely steering the motors, providing an attractive multifunctional approach to powering and controlling motion on the microscale.

### 3.2.2 Fabrication of Magnetic Hydrogel Composites with Random and Linear Magnetic Domains

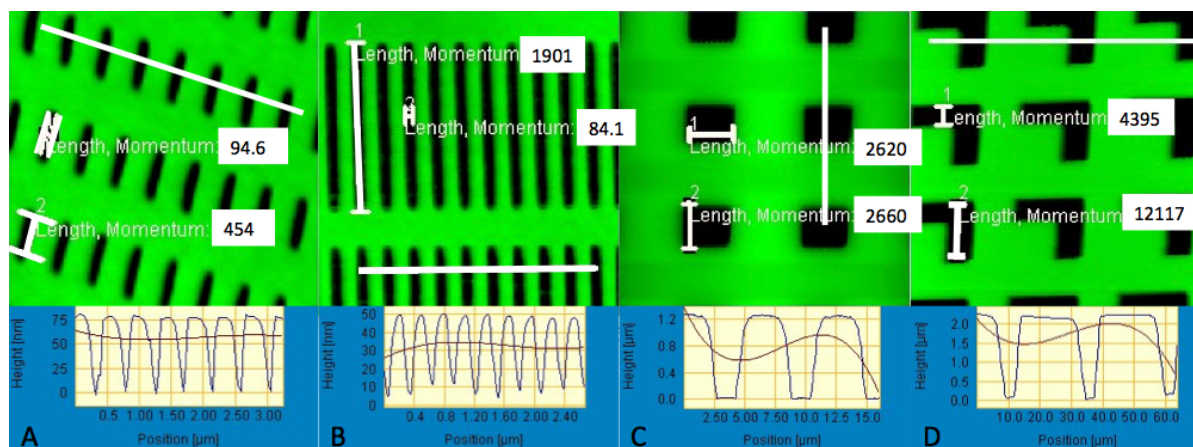
#### 3.2.2.1 General Particle Composition

As mentioned earlier, composite particles were fabricated with some minor modifications using the standard PRINT technique that has been described in great detail elsewhere.<sup>35-38</sup> Particles were primarily composed of PEG<sub>700</sub>diacrylate (Sigma). Amine functionality was imparted through the incorporation of N-aminopropyl methacrylamide (APMA, Polysciences, Inc.). A fluorescent tracer (fluorescein-o-acrylate, Sigma) was used to aid in microscopic characterization and particle tracking. Finally, a photoinitiator 1-hydroxycyclohexylphenyl ketone (HCPK, Sigma) was incorporated to facilitate radical polymerization of the pre-particle solution. Particle details including composition and template size are provided in Table 3.2 and Figure 3.12 respectively.

**Table 3.2** Particle composition, patterned PFPE mold, and thin film attributes.

Particle Composition	
Component	(Wt %)
PEG <sub>700</sub> diacrylate	78
APMA	10
Fe <sub>3</sub> O <sub>4</sub>	10

Fluorescein-o-acrylate	1
HCPK	1

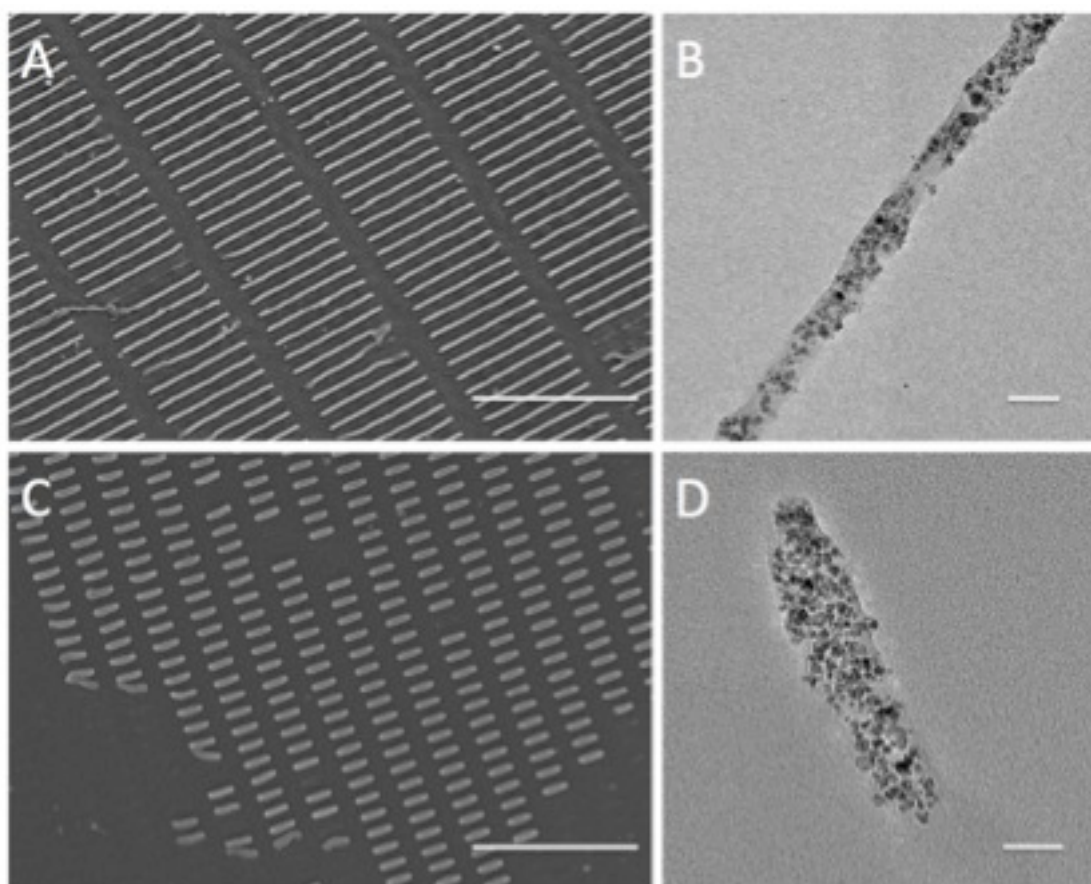


**Figure 3.12** Atomic force micrographs of rice (A), worm-like (B), block (C), and boomerang-shaped (D) particles bound to a sacrificial adhesive layer of poly(cyanoacrylate).

### 3.2.2.2 Nano-scale Particle Fabrication

For particles with a critical dimension measuring 80 nm (80 x 360 nm “rice” and 80 x 2000 nm “worms”), the monomer solution was diluted with dimethylformamide (DMF) after which an aliquot of dextran-stabilized iron oxide (~20 nm Fe<sub>3</sub>O<sub>4</sub>) nanocrystals (FluidMag DX, Chemicell GmbH) was added. The thin film (~2.5 μm) was cast over a sheet of poly(ethylene terephthalate) (PET) using a Mayer rod (2.5 μm feature size RD Specialties, Inc.). After a brief drying period (22 °C) to remove excess DMF, the thin film was laminated to, and immediately split from, a patterned perfluoropolyether (PFPE, Fluorocur<sup>®</sup>, Liquidia Technologies, Inc.) mold (Lot # MC1-0175-131), thus filling the cavities of the mold with a pre-particle suspension. Next, a second sheet of PET was laminated to the surface of the filled mold that was then placed in a UV curing chamber. After curing (~12 J/cm<sup>2</sup>, 365 nm), particles adhered to the PET sheet as it was split from the mold (see Figure 3.13 A and C).

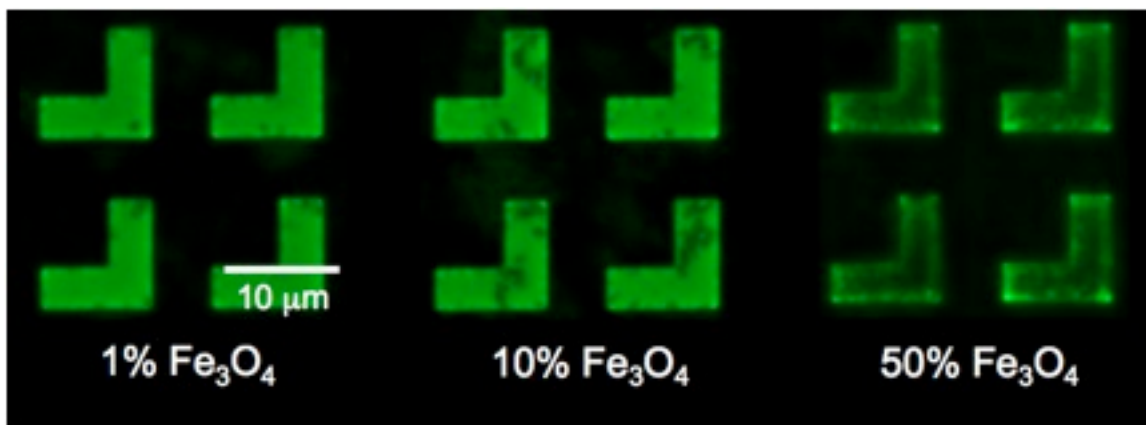
Particles were then removed from the PET by spreading 400  $\mu$ L of distilled water over the surface and gently agitating the particles with a rubber cell scraper. The particles were then rinsed with Milli-Q water to remove any sol fraction and non-magnetic debris using a magnetic column (MiniMacs, Miltenyi Biotec). TEM images of the worm-like and rice nanoparticles (Figure 3.13 B and D) show the successful loading of  $\text{Fe}_3\text{O}_4$ . In addition, there was a fairly uniform distribution of the  $\text{Fe}_3\text{O}_4$  nanoparticles within the polymer matrix. These particles represent the first published examples of shape and size specific magneto-polymer composite nanoparticles fabricated by a top-down method. Given the shape and size control, these composite nanoparticles are very promising candidates for different life science applications.



**Figure 3.13** SEM (A) and TEM (B) of 80 x 2000 nm “worm-like” particles and SEM (C) and TEM (D) of 80 x 360 nm “rice” particles show the nanoscale particles in an array on a PET harvesting layer and cast from solution onto a TEM grid. Scale bars are 3  $\mu\text{m}$  (A), 80 nm (B), 2  $\mu\text{m}$  (C), and 70 nm (D).

### 3.2.2.3 Micro-scale Particle Fabrication

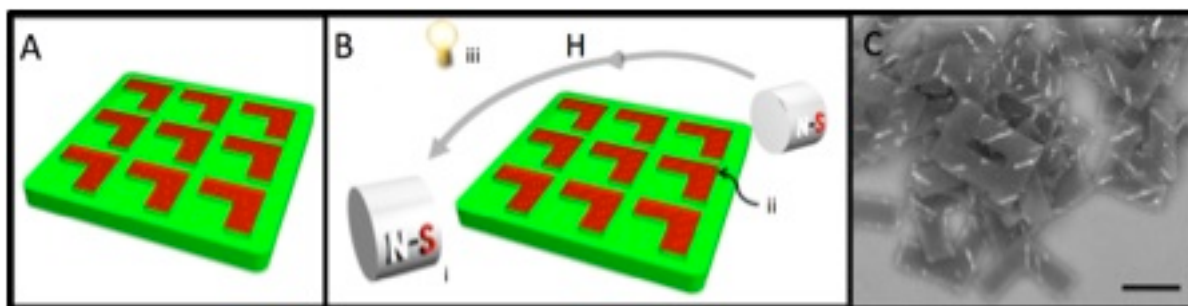
For the micron-sized particles, the  $\text{Fe}_3\text{O}_4$  nanoparticles used were uncoated 200 nm iron oxide (Polysciences, Inc.) instead of the 20 nm surface coated variety. The larger iron oxide particles were used both because they provided stronger magnetic characteristics and because the mold feature sizes were large enough to accommodate the increased iron oxide crystal size. The nanoparticles were stabilized in 1% pluronic solution prior to combining with the monomers. For all experiments, the composite particles were charged with 10 wt%  $\text{Fe}_3\text{O}_4$ , though it was possible with this process to vary the  $\text{Fe}_3\text{O}_4$  content up to 50 wt% (see Figure 3.14). The pre-particle suspension films were cast from a neat solution and fabricated using a similar technique described in previous work.<sup>86</sup> Rhombohedral (block-shaped) and boomerang-shaped particles were centrifuged and washed first with acetone 5 times to remove residual adhesive then transferred to Milli-Q water for improved stability and handling.



**Figure 3.14** Fluorescent micrograph of particles containing 1, 10, and 50 wt % magnetite particles. The composite particles are trapped in a patterned PFPE mold. Small clusters of

magnetite are visible in the 1 and 10 wt % particles as dark spots in the green fluorescent polymer background.

Overall composite particle shape has been shown to dictate the direction of the particle's magnetic moment.<sup>80</sup> Using the template-based PRINT method, the magnetic moment was dictated by the net magnetic moment of the magnetite clusters within the composite particle. Alignment of magnetic nanocrystals within the polymer-composite was possible due to the unique top-down approach to particle fabrication (See Figure 3.15). If alignment of the  $\text{Fe}_3\text{O}_4$  was desired, prior to curing, the filled PFPE mold was placed between two neodymium magnets (5,233 Gauss each) separated by one inch for at least 2 minutes. During this time, the  $\text{Fe}_3\text{O}_4$  nanocrystals formed linear aggregates parallel to the applied field. Directionality of the  $\text{Fe}_3\text{O}_4$  chains, with respect to the polymer composite particle, was controlled by changing the orientation of the mold in the magnetic field. As such, a wide variety of magnetic configurations were possible, thus demonstrating the fact that the orientation of the magnetic moment of the composite particles was independent of the overall particle shape. Next, the mold and magnets were placed in a UV curing chamber that was purged with nitrogen gas. The particles were then cured as described earlier.



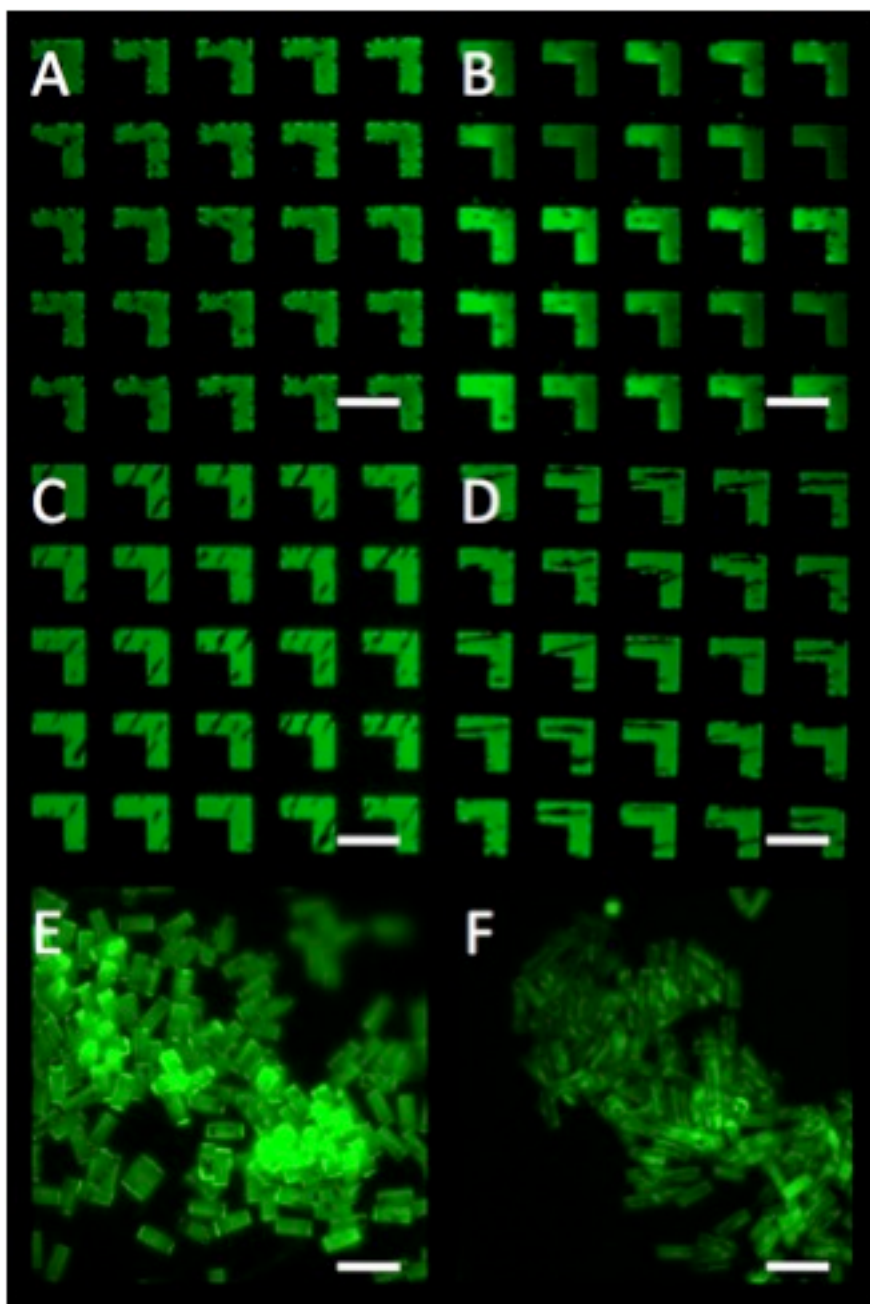
**Figure 3.15** A schematic representation of the PRINT process wherein the PFPE mold (shown in green) (A) and pre-particle solution (shown in red) containing randomly dispersed  $\text{Fe}_3\text{O}_4$  is placed in a magnetic field (B) created by two permanent magnets (i). Linear aggregates of  $\text{Fe}_3\text{O}_4$  (ii) are formed prior to photopolymerization (iii) of the composite

particle. After harvesting and purification linear aggregates of  $\text{Fe}_3\text{O}_4$  are clearly visible via the ESEM backscattered electron detector (C). Scale bar is 10  $\mu\text{m}$ .

#### **3.2.2.4 Directionality of Linear Chains of Magnetite**

Directionality of the linear  $\text{Fe}_3\text{O}_4$  aggregates, examined by fluorescence microscopy, is demonstrated in Figure 3.15. Boomerang particles were cured with the no applied field, a field normal to the plane of the particles, at  $45^\circ$  to both arms of, and parallel to one arm of the particle. Rhombohedral particles were cured with the field perpendicular to and parallel to the length of the particle. In Figure 3.14, the dark regions void of fluorescence within the green polymer matrix clearly indicate the presence of  $\text{Fe}_3\text{O}_4$  nanoparticles. It was found that when there was no applied magnetic field during curing, the composite particles were not homogeneous - the  $\text{Fe}_3\text{O}_4$  nanoparticles form small random aggregates within the particles (Figure 3.16 A). This may be because the nanoparticles were not well-stabilized in the monomer solution. The use of particles stabilized with a suitable organic coating would most likely improve the homogeneity of the composite particles. When the particles were cured in the presence of an applied field, linear aggregates of  $\text{Fe}_3\text{O}_4$  were trapped in specific directions within the micron-sized particles (Figure 3.16 B-F). Alignment of  $\text{Fe}_3\text{O}_4$  within the rice and worm-like particles was difficult to obtain because highly defined linear aggregates were typically larger than the features of the polymer composites themselves.





**Figure 3.16** Fluorescence microscopy images of 10  $\mu\text{m}$  boomerang-shaped particles trapped in the patterned PFPE mold with no linear  $\text{Fe}_3\text{O}_4$  aggregates (A), aggregates normal to the plane of the particle (B), aggregates parallel to the plane at a  $45^\circ$  angle to the arms of the boomerang (C), and aggregates parallel to one arm of the boomerang (D). Harvested block-shaped  $2 \times 2 \times 6 \mu\text{m}$  particles with linear aggregates perpendicular to the length of the particles (E) and parallel to the length of the particles (F). Scale bars are all 10  $\mu\text{m}$ .

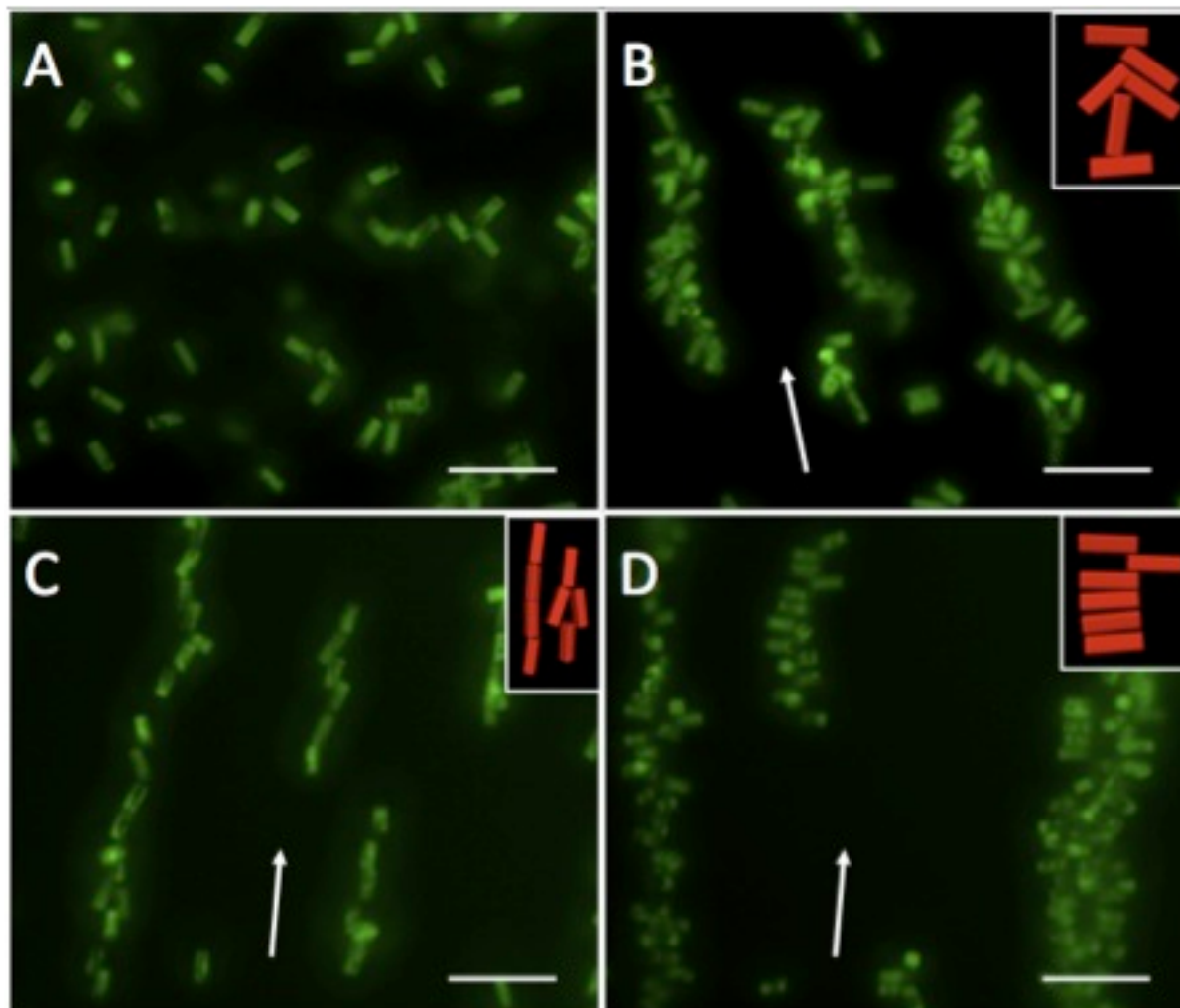
### 3.2.3 Magnetic Manipulation of Microscale Composite Particles



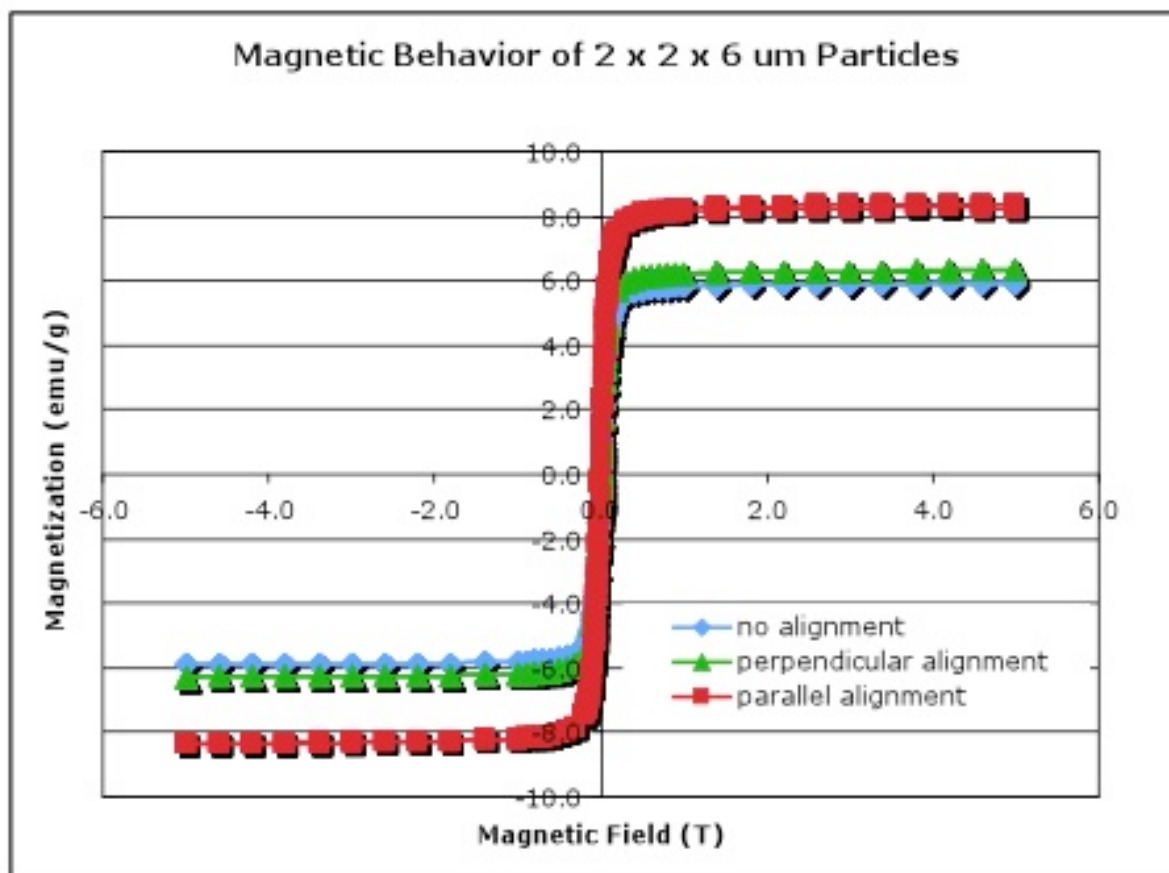
Rhombohedral and boomerang-shaped composite particles were then dispersed in water ( $\phi = 0.0001$ ). In the absence of a magnetic field, the composite particles had no preferred orientation. Once placed in a magnetic field between two identical similarly oriented permanent magnets, the composite particles aligned with the field according to the direction of their highest magnetic moment. Composite particles with linear  $\text{Fe}_3\text{O}_4$  aggregates all aligned with the field in one orientation and followed changes in the magnetic field as it was rotated around the microscope stage. Composite particles with randomly dispersed  $\text{Fe}_3\text{O}_4$  also changed orientation with the applied magnetic field but were not in registration with one another. Movies of boomerang-shaped particles show how the particles preferentially orient themselves with respect to their magnetic poles in a rotating magnetic field. Boomerang-shaped particles with linear  $\text{Fe}_3\text{O}_4$  aggregates parallel to the plane of the particle are shown to rotate while laying flat. By comparison, particles with linear  $\text{Fe}_3\text{O}_4$  aggregates normal to the plane of the particle stand up right while rotating with the external magnetic field.

Magnetic alignment of the composite particles was achieved at higher concentrations ( $\phi = 0.001 - 0.005$ ). As before, the composite particles aligned with their highest magnetic moment parallel to direction of the applied magnetic field. In this case however, the high concentration made it possible for chaining to occur. Based on the directionality of the linear  $\text{Fe}_3\text{O}_4$  aggregates, chaining of  $2 \times 2 \times 6 \mu\text{m}$  rhombohedral particles was observed in three distinct manifestations demonstrated in Figure 3.17. Samples with aggregates aligned with the long axis of the particle formed chains with all of the particles in line with the applied magnetic field. Samples with the linear  $\text{Fe}_3\text{O}_4$  aggregates aligned along the short axis of the particle formed chains of stacked composite particles. Finally, samples in which the

magnetite was not aligned showed chaining with no specific orientation of the composite particles. Once the field was removed, the chains of composite particles fell apart without the need for external agitation or de-Gaussing. SQUID (Superconducting Quantum Interference Device) magnetometry confirmed that particles were superparamagnetic in behavior (Figure 3.18).



**Figure 3.17** Fluorescence microscopy images of a dispersion of block-shaped  $2 \times 2 \times 6 \mu\text{m}$  composite particles in the absence of an applied magnetic field (A). Particles without linear aggregates (B) in an applied magnetic field formed disordered chains, while particles with linear aggregates parallel to (C) and perpendicular to (D) the length of the composite particle formed organized chains stacking head-to-tail and side-to-side respectively. Insets for B, C, and D are cartoons that reflect particle alignment representative of each of the three types of particle. Scale bars are all  $20 \mu\text{m}$ . Arrows indicate direction of applied magnetic field.



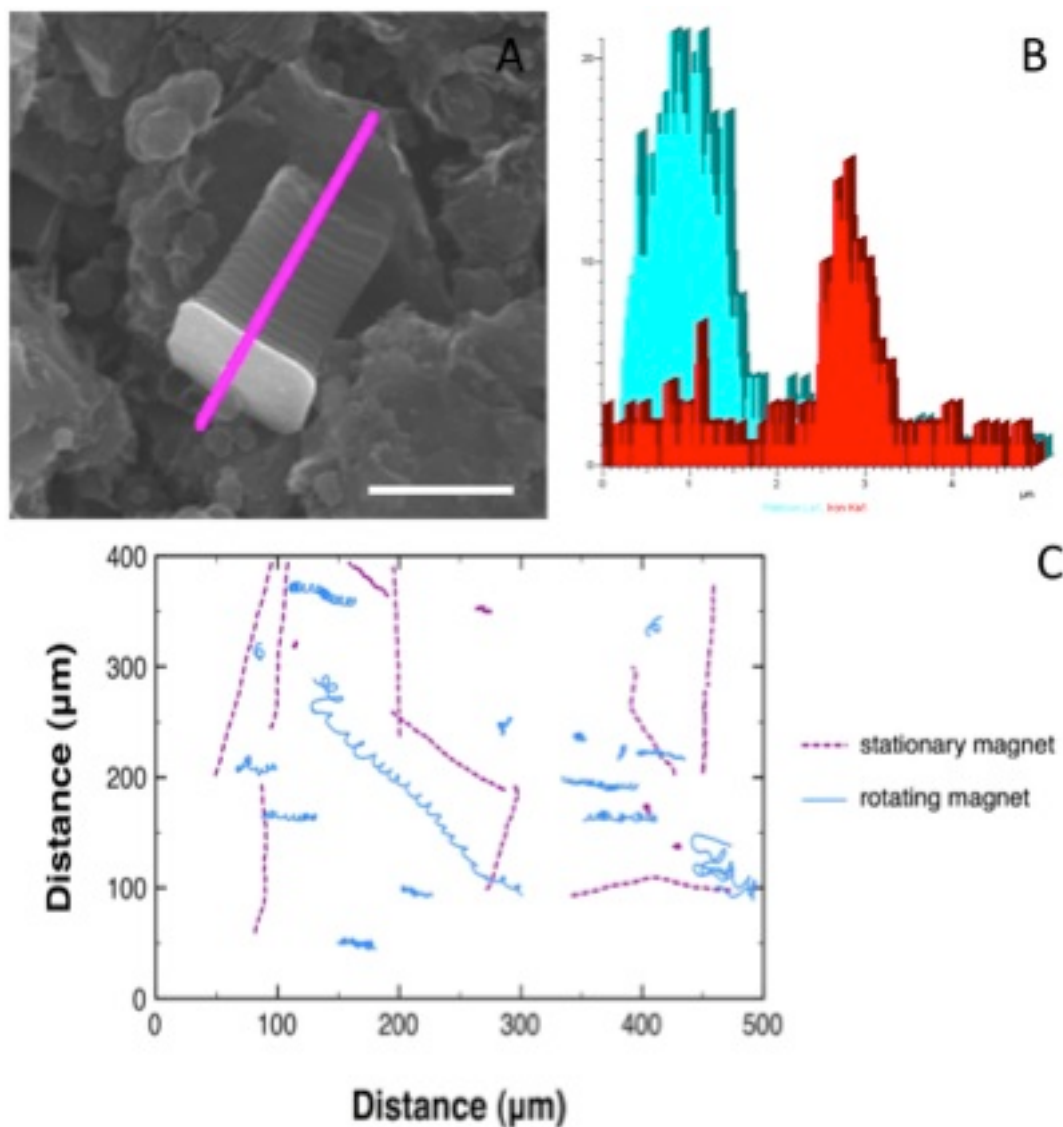
**Figure 3.18** Magnetization curves for  $2 \times 2 \times 6 \mu\text{m}^3$  rhombohedral particles with dispersed  $\text{Fe}_3\text{O}_4$  and linear aggregates of  $\text{Fe}_3\text{O}_4$  aligned perpendicular and parallel to the length of the particles. All magnetic orientations exhibit superparamagnetic behavior.

### 3.2.4 End-labeled Composite Particles and Their Use as Micromotors

#### 3.2.4.1 End-labeling Composite Particles

Using a series of rhombohedral PRINT particles with  $2 \times 2 \mu\text{m}^2$  square cross-sections, the potential for PRINT particles as engineered micromotors was explored. Three aspect ratios were used: 0.5, 2 and 3, and all of the particles contained 10 wt %  $\text{Fe}_3\text{O}_4$  aligned parallel to the height of the particles (perpendicular to the plane of the mold). Two strategies were employed to regiospecifically functionalize the particles: chemical grafting and metal deposition.<sup>87</sup> After photocuring the particles, but while still in the mold, a reactive dye,

Dylight 549-NHS (Fisher Scientific), was grafted onto the exposed face of the particles using the reactive amine groups in the particle matrix. Three nanometers of titanium (Ti) followed by 20 nm platinum (Pt) were evaporated onto the full mold of particles. The particles were then harvested from the mold using poly(cyanoacrylate). Following this, the particles were washed multiple times in acetone and collected in distilled water. It was also possible to put the dye and the metal on opposite faces of the particles. To do so, the particles were poly(cyanoacrylate)-harvested after reacting the dye to the exposed face of the particles, then the Ti and Pt were evaporated on the particles in the harvested array, where the opposite side of the particles were exposed. The particles were then washed and collected as described above. Both approaches were equally effective at anisotropically surface functionalizing the particles. Figure 3.19 demonstrates the successful end-functionalization of a  $2 \times 2 \times 4 \mu\text{m}^3$  particle. The Energy Dispersive Spectroscopy (EDS) elemental line scan in Figure 3.19 clearly indicates the relative locations of the platinum and iron present in the particle.

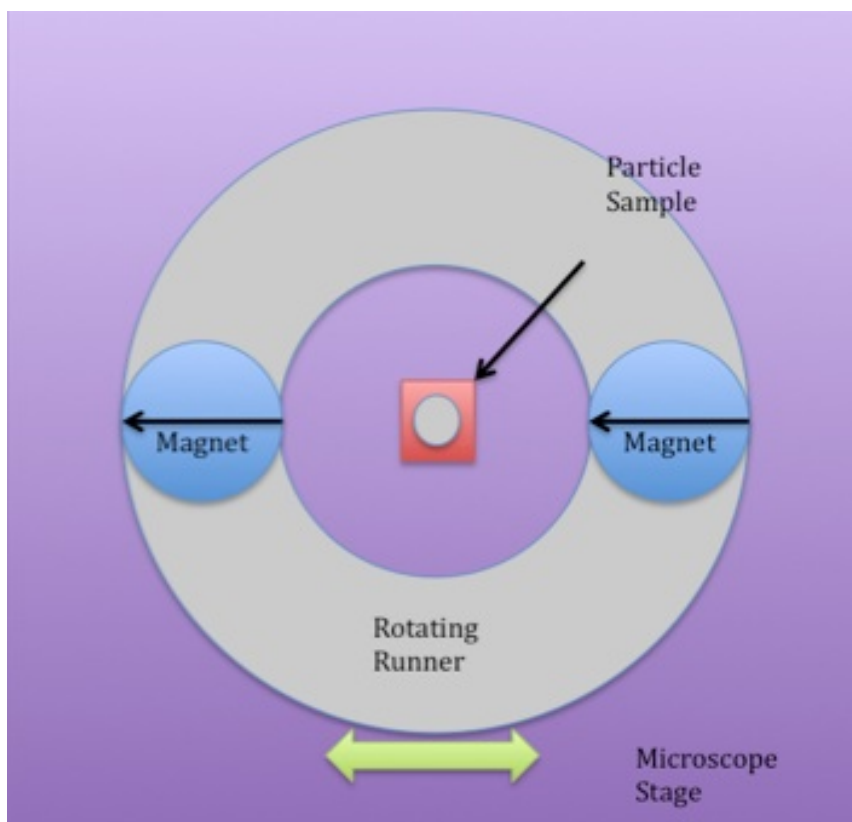


**Figure 3.19** SEM image (A) of a Pt-capped  $2 \times 2 \times 4 \mu\text{m}^3$  PRINT particle containing linear aggregates of  $\text{Fe}_3\text{O}_4$  with elemental line scan (magenta) indicating the location of the iron (red) and platinum (teal) in the particle. Scale bar is  $2 \mu\text{m}$ . Traces of  $2 \times 2 \times 4 \mu\text{m}^3$  particles (C) in 10% in a stationary (dotted) and rotating (solid) magnetic field  $\text{H}_2\text{O}_2$ .

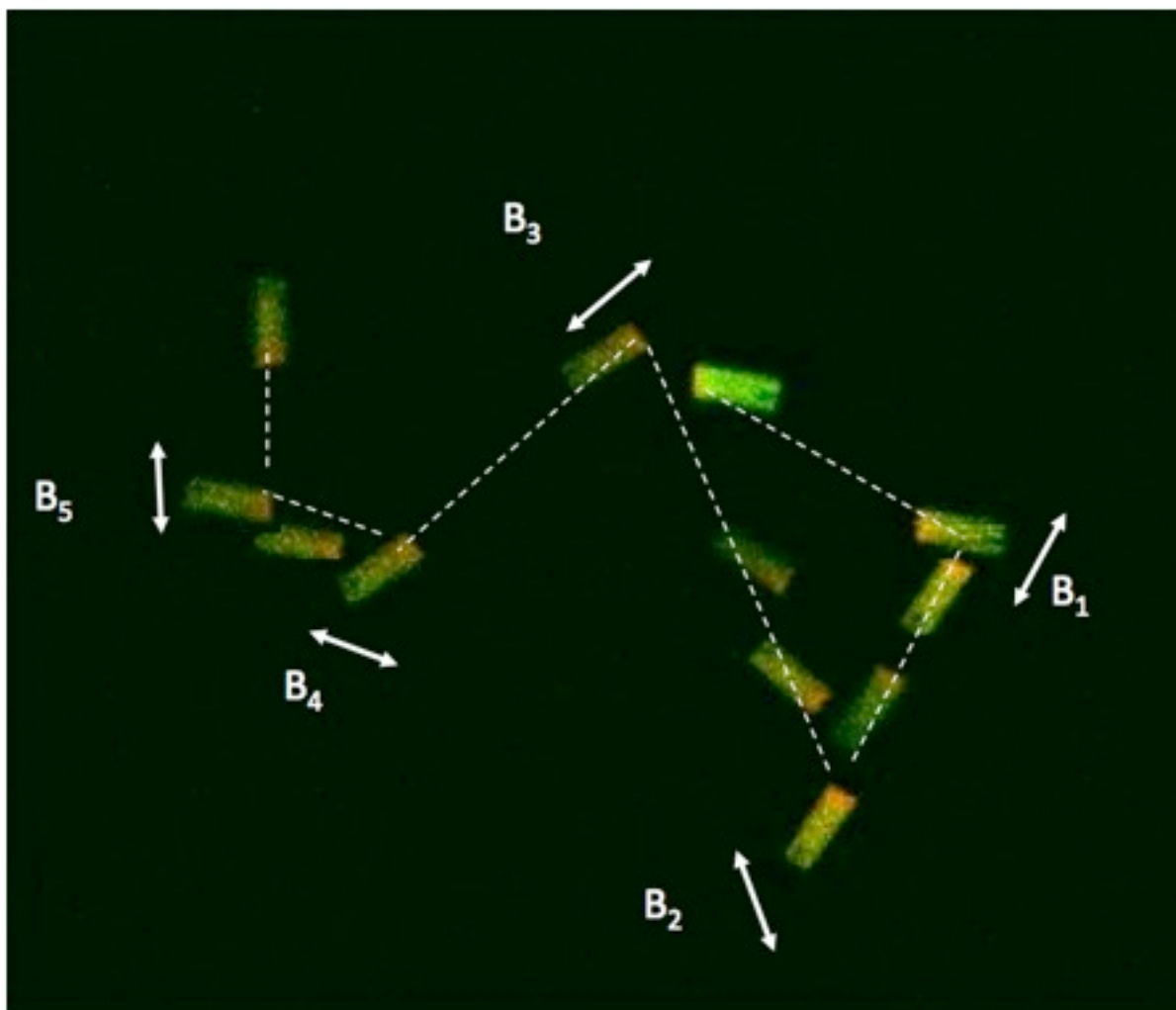
#### 3.2.4.1 Background of Micromotor Particles in $\text{H}_2\text{O}_2$

The Pt-capped, magneto-polymer PRINT particles were studied in the presence of hydrogen peroxide ( $\text{H}_2\text{O}_2$ ). It is well known that Pt catalyzes the decomposition of  $\text{H}_2\text{O}_2$  to water and oxygen. This reaction has been exploited to power the motion of nano- and

microobjects in solution, though there is some dispute as to the mechanism of motion, whether due to bubble formation<sup>88</sup> or self-diffusiophoresis<sup>89</sup>. Despite this ambiguity, it was observed that the Pt-capped, magneto-polymer PRINT particles were definitely motile in H<sub>2</sub>O<sub>2</sub> solution. Moreover, it was found that the motion was linear and directed away from the Pt end of the particle. Similar to the boomerang-shaped particles described above, Fe<sub>3</sub>O<sub>4</sub> present in the Pt-endcapped particles provided a mechanism for changing the direction of particles in solution. The direction of a  $2 \times 2 \times 6 \mu\text{m}^3$  particle, containing magnetite chained along the long axis of the rod, was changed by moving a strong permanent magnet around the microscope stage (see Figure 3.20). The particle responded immediately to the change in position of the magnet, and thus was able to be steered accurately. A movie of the steered motion of a  $2 \times 2 \times 6 \mu\text{m}^3$  rod was converted to a schematic (see Figure 3.21). The dye was placed on the same end of the particle as the Pt to clearly illustrate that the motion is directed away from the Pt end.



**Figure 3.20** Schematic of an in-house magnetic stage for particle rotation and alignment experiments in water. The runner (gray) rotates in a circular fashion (green double-sided arrow) around the magnetic particle sample (red and gray) in the center of the microscope stage (purple). Magnets at opposite ends of the runner (blue) with similarly facing magnetic fields (black arrows) create a magnetic field across the particle sample that rotates with the runner.



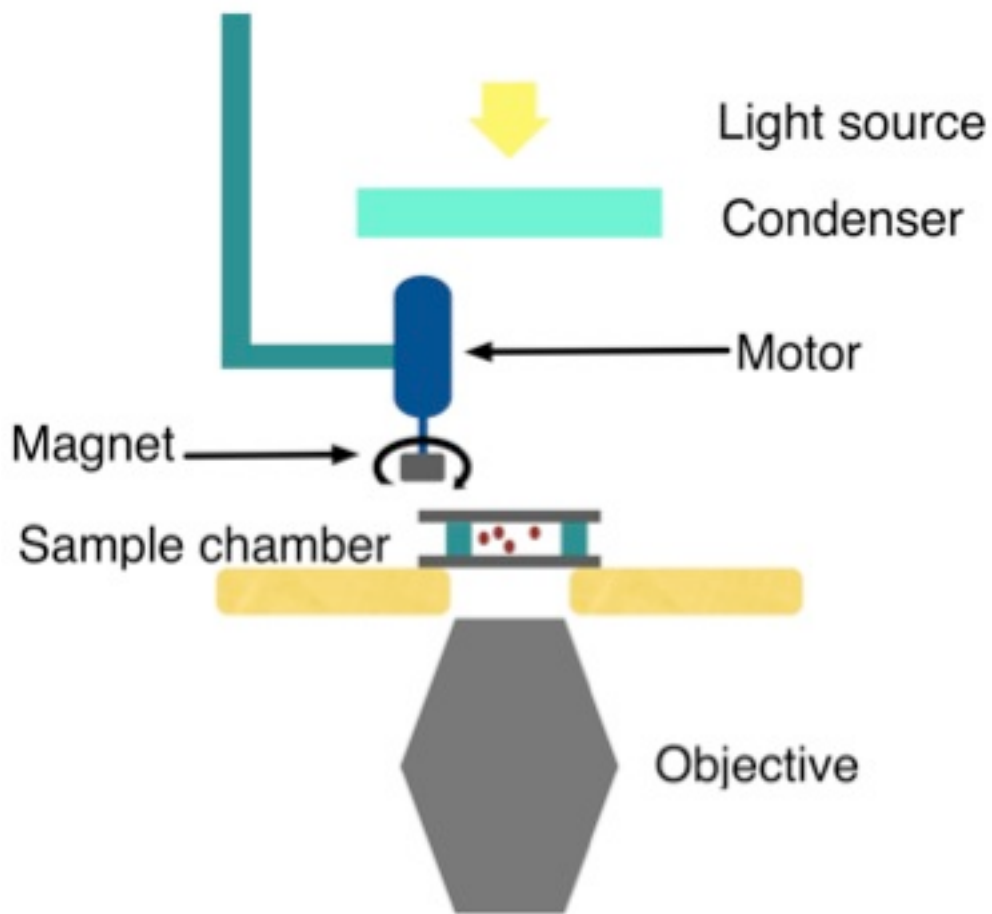
**Figure 3.21** Schematic representation of a movie of one microscale rocket particle in 10 %  $\text{H}_2\text{O}_2$ . The particle moves through space in a linear fashion parallel to the direction of the applied magnetic field ( $B$ ). Once the direction of  $B$  is changed the particle changes direction.

#### 3.2.4.2 Micromotor Particles in $\text{H}_2\text{O}_2$ in a Stationary Magnetic Field

Particle motion was observed as a function of particle aspect ratio (0.5, 2, 3) and  $\text{H}_2\text{O}_2$  concentration (0%, 10%, 20%, 30%). The particles were tracked in the presence of a stationary or rotating magnet; due to the microscope configuration, the magnet was located off-center above the solution. Figure 3.22 offers a schematic description of microscope and magnetic setup for these experiments. For the stationary magnet experiments, at 0%  $\text{H}_2\text{O}_2$ , all of the particles exhibited small random movements due to Brownian motion. With



increasing  $\text{H}_2\text{O}_2$  concentration, the particles were propelled linearly through solution, and for each particle aspect ratio, the particle velocities were the same (within error, Table 3.2) with increasing  $\text{H}_2\text{O}_2$  concentrations. The highest particle velocities were observed with the  $2 \times 2 \times 4 \mu\text{m}^3$ , at speeds as high as  $6 \mu\text{m/s}$ . It was expected that the smallest particle, the  $2 \times 2 \times 1 \mu\text{m}^3$  square discs, would be the fastest, however, they appeared to move slower than the  $2 \times 2 \times 4 \mu\text{m}^3$  rods. This may be because the motion of the disks was somewhat irregular, and they tended to change direction fairly readily, unlike the more elongated particles. The  $2 \times 2 \times 6 \mu\text{m}^3$  rods were the slowest, which was expected because they were the largest in the particle series.



**Figure 3.22** The above figure is a schematic of the microscope-sample-rotating magnet setup. The magnet is mounted on a motor and is suspended above the sample, slightly off-center from the path of the transmitted light.

**Table 3.3** Particle translational velocities for all particle sizes under a stationary magnetic field (no field) with varying solutions of  $\text{H}_2\text{O}_2$ .

Particle Size ( $\mu\text{m}^3$ )	% $\text{H}_2\text{O}_2$	Average Translational Velocity ( $\mu\text{m/s}$ )	Standard error
2x2x1	0	0.25	0.07
2x2x1	10	28.49	10.76
2x2x1	20	22.14	7.83
2x2x1	30	27.29	12.21
2x2x4	0	0.21	0.06
2x2x4	10	54.88	12.94
2x2x4	20	47.30	21.15
2x2x4	30	56.97	28.49
2x2x6	0	0.93	0.19
2x2x6	10	22.62	5.84
2x2x6	20	16.33	8.17
2x2x6	30	22.96	13.25

#### 3.2.4.2 Micromotor Particles in $\text{H}_2\text{O}_2$ in a Rotating Magnetic Field

For the rotating magnet experiments, at 0 %  $\text{H}_2\text{O}_2$  the particles rotated at the same speed as the magnet about their axes with no lateral motion. In the presence of  $\text{H}_2\text{O}_2$ , a very unusual type of particle motion was observed. All of the particles tended to travel a prolate cycloid path. The particle tracks for both the stationary and rotating magnet experiments are presented in Figure 3.18 C. This unique motion occurred because the particles were experiencing both a linear force due to  $\text{H}_2\text{O}_2$  decomposition as well as the torque from the rotating magnet located off to one side of the solution. In addition, the particle velocities were found to be significantly slower than in the presence of the stationary magnet.

#### 3.2.5 Magneto-Polymer Composites Summary

The development of magneto-polymer composite nanoscale and microscale particles has potential for a number of new biomedical and materials-based applications. Using the PRINT technique, we have shown fabrication of such particles with highly tailored form

factors ranging in size from 50 nm to 10  $\mu\text{m}$ . The microscale composite particles were fabricated with a variety of different magnetic conformations with respect to the overall particle dimensions. We have shown the manipulation of these particles in solution using applied magnetic fields. We also demonstrated regiospecific functionalization of these particles with amine reactive organic dyes and deposited platinum for use as self-propelled micromotors in  $\text{H}_2\text{O}_2$ . These experiments clearly demonstrate our ability to manipulate the motion of catalytically-driven magneto-polymer PRINT particles. Smaller and more highly magnetic nanocomposites are currently being examined. We hope that this work will open the door to new, exciting applications in magnetic colloids and micro- and nanomotors and machines.

## References

1. Glotzer, S. C.; Solomon, M. J., *Nature Mater.* 2007, 6, 557-562.
2. Velev, O. D., *Science* 2006, 312, 376-377.
3. Velev, O. D., *Science* 2006, 312 (5772), 376-7.
4. Bae, Y.; Kim, N. H.; Kim, M.; Lee, K. Y.; Han, S. W., *J. Am. Chem. Soc.* 2008, 130, 5432-5433.
5. Cozzoli, P. D.; Pellegrino, T.; Manna, L., *Chem. Soc. Rev.* 2006, 35, 1195-1208.
6. Talapin, D. V.; Nelson, J. H.; Shevchenko, E. V.; Aloni, S.; Sadtler, B.; Alivisatos, A. P., *Nano Lett.* 2007, 7, 2951-2959.
7. Badaire, S.; Cottin-Bizonne, C.; Woody, J. W.; Yang, A.; Stroock, A. D., *J. Am. Chem. Soc.* 2007, 129, 40-41.
8. Moon, S. I.; McCarthy, T. J., *Macromol.* 2003, 36, 4253-4255.
9. Park, S.; Lim, J.-H.; Chung, S.-W.; Mirkin, C. A., *Science* 2004, 303, 348-351.
10. Zhao, K.; Mason, T. G., *Phys. Rev. Lett.* 2007, 99, 268301.
11. Hernandez, C. J.; Mason, T. G., *J. Phys. Chem. C* 2007, 111, 4477-4480.
12. Dendukuri, D.; Hatton, T. A.; Doyle, P. S., *Langmuir* 2007, 23, 4669-4674.
13. Fujibayashi, T.; Okubo, M., *Langmuir* 2007, 23, 7958-7962.
14. Kim, J.-W.; Larsen, R. J.; Weitz, D. A., *J. Am. Chem. Soc.* 2006, 128, 14374-14377.
15. Champion, J. A.; Katare, Y. K.; Mitragotri, S., *Proc. Natl. Acad. Sci. U.S.A.* 2007, 104, 11901-11904.
16. Kim, S.-H.; Yi, K. H.; Yang, S.-M., *Langmuir* 2008, 24, 2365-2371.
17. Xu, S.; Nie, Z.; Seo, M.; Lewis, P.; Kumacheva, E.; Stone, H. A.; Garstecki, P.; Weibel, D. B.; Gitlin, I.; Whitesides, G. M., *Angew. Chem., Int. Ed.* 2005, 44, 724-728.
18. Chung, S. E.; Park, W.; Park, H.; Yu, K.; Park, N.; Kwon, S., *Appl. Phys. Lett.* 2007, 91, 041106.

19. Dendukuri, D.; Pregibon, D. C.; Collins, J.; Hatton, T. A.; Doyle, P. S., *Nature Mater.* 2006, 5, 365-369.
20. Dendukuri, D.; Tsoi, K.; Hatton, T. A.; Doyle, P. S., *Langmuir* 2005, 21, 2113-2116.
21. Nie, Z.; Xu, S.; Seo, M.; Lewis, P. C.; Kumacheva, E., *J. Am. Chem. Soc.* 2005, 127, 8058-8063.
22. Sung, K. E.; Vanapalli, S. A.; Mukhija, D.; McKay, H. A.; Millunchick, J. M.; Burns, M. A.; Solomon, M. J., *J. Am. Chem. Soc.* 2008, 130, 1335-1340.
23. Moon, J. H.; Kim, A. J.; Crocker, J. C.; Yang, S., *Adv. Mater.* 2007, 19, 2508-2512.
24. Glangchai, L. C.; Caldorera-Moore, M.; Shi, L.; Roy, K., *J. Controll. Rel.* 2008, 125, 263-272.
25. Guan, J.; Chakrapani, A.; Hansford, D. J., *Chem. Mater.* 2005, 17, 6227-6229.
26. Gratton, S. E. A.; Pohlhaus, P. D.; Lee, J.; Guo, J.; Cho, M. J.; DeSimone, J. M., *J. Controlled Release* 2007, 121, 10-18.
27. Hampton, M. J.; Williams, S. S.; Zhou, Z.; Nunes, J.; Ko, D. H.; Templeton, J. L.; Samulski, E. T.; DeSimone, J. M., *Adv. Mater.* 2008, DOI: 10.1002/adma.200702495.
28. Kelly, J.; DeSimone, J. M., *J. Am. Chem. Soc.* 2008, 130, 5438-5439.
29. Maynor, B. W.; LaRue, I.; Hu, Z.; Rolland, J. P.; Pandya, A.; Fu, Q.; Liu, J.; Spontak, R. J.; Sheiko, S. S.; Samulski, R. J.; Samulski, E. T.; DeSimone, J. M., *Small* 2007, 3, 845-849.
30. Petros, R. A.; Ropp, P. A.; DeSimone, J. M., *J. Am. Chem. Soc.* 2008, 130, 5008-5009.
31. Rolland, J. P.; Maynor, B. W.; Euliss, L. E.; Exner, A. E.; Denison, G. M.; DeSimone, J. M., *J. Am. Chem. Soc.* 2005, 127, 10096-10100.
32. Jones, T. B., *Electromechanics of Particles*. Cambridge University Press: New York, 1995; p 265.
33. Park, C.; Robertson, R. E., *Mater. Sci. Eng. A* 1998, 257, 295-311.
34. Dassanayake, U.; Fraden, S.; van Blaaderen, A., *J. Chem. Phys.* 2000, 112, 3851-3858.

35. Dong, L.; Huang, J. P.; Yu, K. W., *J. Appl. Phys.* 2004, **95**, 8321-8326.
36. Lumsdon, S. O.; Kaler, E. W.; Velev, O. D., *Langmuir* 2004, **20**, 2108-2116.
37. Velev, O. D.; Bhatt, K. H., *Soft Matter* 2006, **2**, 738-750.
38. Fan, C. Z.; Huang, J. P.; Yu, K. W., *J. Phys. Chem. B* 2006, **110**, 25665-25670.
39. Radu, M.; Ionescu, M.; Irimescu, N.; Iliescu, K.; Pologea-Moraru, R.; Kovacs, E., *Biophys. J.* 2005, **89**, 3548-3554.
40. Park, C.; Robertson, R. E., *J. Mater. Sci.* 1998, **33**, 3541-3553.
41. Park, C.; Wilkinson, J.; Banda, S.; Ounaies, Z.; Wise, K.; Sauti, G.; Lillehei, P. T.; Harrison, J., *J. Polym. Sci.: B: Polym. Phys.* 2006, **44**, 1751-1762.
42. Tomer, V.; Randall, C. A.; Polizos, G.; Kostelnick, J.; Manias, E., *J. Appl. Phys.* 2008, **103**, 034115.
43. Wilson, S. A.; Maistros, G. M.; Whatmore, R. W., *J. Phys. D: Appl. Phys.* 2005, **38**, 175-182.
44. Asencor, F. J.; Santamaria, C.; Iglesias, F. J.; Dominguez, A., *Biophys. J.* 1993, **64**, 1626-1631.
45. Morgan, H.; Green, N. G., *J. Electrostat.* 1997, **42**, 279-293.
46. Poortinga, A. T.; Bos, R.; Busscher, H. J., *Biotechnol. Bioeng.* 2000, **67**, 117-120.
47. Yang, M.; Chew Lim, C.; Liao, R.; Zhang, X., *J. Microelectromech. Sys.* 2006, **15**, 1483-1491.
48. Yang, C. Y.; Lei, U., *J. Appl. Phys.* 2007, **102**, 094702.
49. Saito, M.; Schwan, H. P.; Schwarz, G., *Biophys. J.* 1966, **6**, 313-327.
50. Bhatt, K. H.; Velev, O. D., *Langmuir* 2004, **20**, 467-476.
51. Lumsdon, S. O.; Kaler, E. W.; Williams, J. P.; Velev, O. D., *Appl. Phys. Lett.* 2003, **82**, 949-951.
52. Gupta, A. K.; Gupta, M., *Biomaterials* 2005, **26** (18), 3995-4021.
53. Pankhurst, Q. A.; Connolly, J.; Jones, S. K.; Dobson, J., *Journal of Physics D: Applied Physics* 2003, **36**, R167-R181.

54. Rusetski, A. N.; Ruuge, E. K., *Journal of Magnetism and Magnetic Materials* 1990, 85 (1-3), 299-302.
55. Ruuge, E. K.; Rusetski, A. N., *Journal of Magnetism and Magnetic Materials* 1993, 122 (1-3), 335-339.
56. Voltairas, P. A.; Fotiadis, D. I.; Michalis, L. K., *Journal of Biomechanics* 2002, 35 (6), 813-821.
57. Mair, L.; Ford, K.; Alam, M.; Kole, R.; Fisher, M.; Superfine, R., *Journal of Biomedical Nanotechnology* 2009, 5, 182-191.
58. Mair, L.; Ford, K.; Alam, M. R.; Kole, R.; Fisher, M.; Superfine, R., *Journal of Biomedical Nanotechnology* 2009, 5, 182-191.
59. Buerli, T.; Pellegrino, C.; Baer, K.; Lardi-Studler, B.; Chudotvorova, I.; Fritschy, J.-M.; Medina, I.; Fuhrer, C., *Nat. Protocols* 2007, 2 (12), 3090-3101.
60. Ding, T.; Song, K.; Clays, K.; Tung, C.-H., *Advanced Materials* 2009, 21 (19), 1936-1940.
61. Ge, J.; Lee, H.; He, L.; Kim, J.; Lu, Z.; Kim, H.; Goebel, J.; Kwon, S.; Yin, Y., *Journal of the American Chemical Society* 2009.
62. Lu, Y.; Yin, Y.; Xia, Y., *Advanced Materials* 2001, 13 (6), 415-420.
63. Bangar, M. A.; Hangarter, C. M.; Yoo, B.; Rheem, Y.; Chen, W.; Mulchandani, A.; Myung, N. V., *Electroanalysis* 2009, 21 (1), 61-67.
64. Hangarter, C. M.; Myung, N. V., *Chemistry of Materials* 2005, 17 (6), 1320-1324.
65. Biswal, S. L.; Gast, A. P., *Analytical Chemistry* 2004, 76 (21), 6448-6455.
66. Kavcic, B.; Babic, D.; Osterman, N.; Podobnik, B.; Poberaj, I., *Applied Physics Letters* 2009, 95 (2), 023504-3.
67. Ng, J. M. K.; Gitlin, I.; Stroock, A., D.; Whitesides, G., M., *Electrophoresis* 2002, 23 (20), 3461-3473.
68. Burdick, J.; Laocharoensuk, R.; Wheat, P. M.; Posner, J. D.; Wang, J., *Journal of the American Chemical Society* 2008, 130 (26), 8164-8165.
69. Dreyfus, R.; Baudry, J.; Roper, M. L.; Fermigier, M.; Stone, H. A.; Bibette, J., *Nature* 2005, 437 (7060), 862-865.

70. Ghosh, A.; Fischer, P., *Nano Letters* 2009, 9 (6), 2243-2245.
71. Tierno, P.; Golestanian, R.; Pagonabarraga, I.; Sagues, F., *Physical Review Letters* 2008, 101 (21), 218304.
72. Caruso, F.; Susha, A., S.; Giersig, M.; Möhwald, H., *Advanced Materials* 1999, 11 (11), 950-953.
73. Dyab, A. K. F.; Ozmen, M.; Ersoz, M.; Paunov, V. N., *Journal of Materials Chemistry* 2009, 19, 3475-3481.
74. Ge, J.; Hu, Y.; Zhang, T.; Yin, Y., *Journal of the American Chemical Society* 2007, 129 (29), 8974-8975.
75. Isojima, T.; Suh, S. K.; Vander Sande, J. B.; Hatton, T. A., *Langmuir* 2009, 25 (14), 8292-8298.
76. Zhao, N.; Gao, M., *Advanced Materials* 2009, 21 (2), 184-187.
77. Park, J.-H.; von Maltzahn, G.; Zhang, L.; Schwartz, M. P.; Ruoslahti, E.; Bhatia, S. N.; Sailor, M. J., *Advanced Materials* 2008, 20 (9), 1630-1635.
78. Zhu, J.; Hayward, R. C., *Journal of the American Chemical Society* 2008, 130 (23), 7496-7502.
79. Geng, Y.; Dalhaimer, P.; Cai, S.; Tsai, R.; Tewari, M.; Minko, T.; Discher, D. E., Shape effects of filaments versus spherical particles in flow and drug delivery. 2007.
80. Hwang, D. K.; Dendukuri, D.; Doyle, P. S., *Lab on a Chip* 2008, 8, 1640-1647.
81. Wang, B.; Shum, H. C.; Weitz, D. A., *ChemPhysChem* 2009, 10 (4), 641-645.
82. Chen, C.-H.; Abate, A. R.; Lee, D.; Terentjev, E. M.; Weitz, D. A., *Advanced Materials* 2009, 21 (31), 3201-3204.
83. Gratton, S. E. A.; Williams, S. S.; Napier, M. E.; Pohlhaus, P. D.; Zhou, Z.; Wiles, K. B.; Maynor, B. W.; Shen, C.; Olafsen, T.; Samulski, E. T.; DeSimone, J. M., *Accounts of Chemical Research* 2008, 41 (12), 1685-1695.
84. Herlihy, K. P. D., Joseph M., *Proceedings of SPIE* 2007, 6517 (2), 651737.1-651737.8.
85. Paxton, W. F.; Sundararajan, S.; Mallouk, T. E.; Sen, A., *Angewandte Chemie International Edition* 2006, 45 (33), 5420-5429.



86. Herlihy, K. P.; Nunes, J.; Desimone, J. M., Electrically driven alignment and crystallization of unique anisotropic polymer particles. In *Langmuir : the ACS journal of surfaces and colloids*, 2008; Vol. 24, pp 8421-6.
87. Zhang, H.; Nunes, J. K.; Gratton, S. E. A.; Herlihy, K. P.; Pohlhaus, P. D.; Desimone, J. M., Fabrication of multiphasic and regio-specifically functionalized PRINT ®particles of controlled size and shape. In *New J. Phys.*, 2009; Vol. 11, p 075018.
88. Gibbs, J.; Zhao, Y., Autonomously motile catalytic nanomotors by bubble propulsion. In *Appl. Phys. Lett.*, 2009; Vol. 94, p 163104.
89. Howse, J.; Jones, R.; Ryan, A.; Gough, T.; Vafabakhsh, R.; Golestanian, R., Self-motile colloidal particles: from directed propulsion to random walk. In *Physical Review Letters*, 2007; Vol. 99, p 48102.